The University of Southern Mississippi
The Aquila Digital Community

Dissertations

Spring 5-1-2018

Polymer Nanocomposites Containing High Aspect Ratio Particulates: Innovation in Co-Extruded Multilayer Barrier Films

Kevin Meyers
University of Southern Mississippi

Follow this and additional works at: https://aquila.usm.edu/dissertations

 Part of the Materials Chemistry Commons, Polymer and Organic Materials Commons, Polymer Chemistry Commons, Polymer Science Commons, and the Transport Phenomena Commons

Recommended Citation

Meyers, Kevin, "Polymer Nanocomposites Containing High Aspect Ratio Particulates: Innovation in Co-Extruded Multilayer Barrier Films" (2018). *Dissertations*. 1494.
https://aquila.usm.edu/dissertations/1494

This Dissertation is brought to you for free and open access by The Aquila Digital Community. It has been accepted for inclusion in Dissertations by an authorized administrator of The Aquila Digital Community. For more information, please contact Joshua.Cromwell@usm.edu.

POLYMER NANOCOMPOSITES CONTAINING HIGH ASPECT RATIO PARTICULATES: INNOVATION IN CO-EXTRUDED MULTILAYER BARRIER FILMS

by

Kevin Patrick Meyers

A Dissertation
Submitted to the Graduate School,
the College of Science and Technology
and the School of Polymers and High Performance Materials
at The University of Southern Mississippi
in Partial Fulfillment of the Requirements
for the Degree of Doctor of Philosophy

Approved by:

Dr. Sergei Nazarenko, Committee Chair
Dr. Jeffrey Wiggins
Dr. James Rawlins
Dr. Sarah Morgan
Dr. Robert Lochhead

Dr. Sergei Nazarenko Committee Chair	Dr. Jeffrey Wiggins Department Chair	Dr. Karen S. Coats Dean of the Graduate School

May 2018

COPYRIGHT BY

Kevin Patrick Meyers

2018

Published by the Graduate School

ABSTRACT

POLYMER NANOCOMPOSITES CONTAINING HIGH ASPECT RATIO PARTICULATES: INNOVATION IN CO-EXTRUDED MULTILAYER BARRIER FILMS

by Kevin Patrick Meyers

May 2018

Delaminated montmorillonite (MMT) clay/ maleic anhydride grafted LLDPE nanocomposite multilayer films with alternating layers of LDPE were produced through multilayer co-extrusion. The MMT concentration within the nanocomposite layers was increased through annealing the films in the melt due to a mismatch in interdiffusion rates of the polymer layers. Analysis of the nanocomposite layers upon annealing revealed that the platelets impinged upon one another resulting in significant improvement in oxygen barrier in the multilayer system, exceeding the results of bulk nanocomposites.

Model analysis demonstrated that increasing the nanoplatelet aspect ratio or initial concentration in the filled layers would lead to even higher barrier. This lead to an investigation into high aspect ratio graphene nanoplatelete composites. Gas and fire barrier, mechanical, and thermal property enhancement of polyethylene/ short stack graphene nanoplatelet (xGnP) composite systems were thoroughly analyzed in bulk composites and multilayers. Through incorporation of a small amount of xGnP in LLDPE, a substantial increase in barrier and mechanical strength was observed, even without polymer/platelet modification. Composite layer shrinkage from controlled interdiffusion in the melt was confirmed and resulted in a decrease in permeability for the

coextruded films that reflected barrier properties of composite multilayers with initially more GnPs.

Finally, to better understand clay-polymer interactions, amorphous hyperbranched polyester (HBP)/MMT nanocomposites were studied. With increasing clay content, the composites' glass transition (T_g) and heat capacity (ΔC_p) at T_g showed behavior indicative of the suppression of the HBP's segmental mobility. This behavior correlated to changes in intercalation interlayer spacing. The fraction of the mobile amorphous fraction (MAF), which contributed to the change in heat capacity at T_g, and corresponding rigid amorphous fraction (RAF) were calculated based on the corresponding ΔC_p. Calculation of interlayer spacings from the ΔC_p data were in agreement with those determined by x-ray diffraction. The results demonstrated that changes in the RAF and MAF content depend on both the clay volume fraction and the clay morphology. Furthermore, a novel approach to estimate MAF and RAF via positron annihilation lifetime spectroscopy (PALS) from the thermal expansivities of free volume hole sizes in the liquid and glassy states was proposed.

ACKNOWLEDGMENTS

I am sincerely grateful to my advisor, Dr. Sergei Nazarenko, for his guidance, patience, and perseverance throughout my research career at the University of Southern Mississippi. I thank him for giving me the opportunity to work on a variety of interesting projects, both industrial and academic, that gave me a broad foundation of polymer related research and analytic skills and allowed me to share my research at national conferences around the country. His expertise in polymer physics and structure-property relationships is unique and he was always available to give insight and tutelage. I want to thank Dr. Nazarenko for pushing me to apply for the National Science Foundation's (NSF) Graduate STEM Fellows in K-12 Education (*GK-12 Fellowship)* and for Dr. Morgan and Kim Wingo for taking me into the program and helping me expand out of my comfort zone and improve on my scientific communication skills. I would also like to thank Shalawn Clark who was so kind and helpful while I visited her high school chemistry classroom as part of the GK-12 program. I want to thank Dr. Eric Baer for heading the NSF's Science and Technology Center for Layered Polymeric Systems (CLiPS) that provided both insight and opportunities for research involving layered polymer structures. I would like to thank the graduate students at Case Western Reserve University who worked with me to facilitate my CLiPS research. Primarily I would like to thank Matthew Herbert and Dr. David Schiraldi whose research group we collaborated with on the phosphate glass work. I would like to thank the REU students that helped me with my research during their summer, Emily Fullwood, Vander Breland and Michael Otto, and my Polymer Envoy high school students. I would like to thank the Robert M. Hearin Foundation and the Bryce Corporation for their financial contributions to continue

my research. I would very much like to thank all of the graduate students in the Polymer Science program at USM, especially the members of the Nazarenko group for their friendship and research help. I'd like to thank Justin Brandt for guiding me when I initial joined the group, Jeremy Decker for his collaboration, and all the other members of the Nazarenko group including Brian, Luke, Mukul, Yingji, Jim, Maliha, Ramesh, Vivek, and Beibei for all their help. I'd also like to thank our lab manager Jody Wiggins who made my life so much easier with all her hard work with things I know I took for granted. Finally, I'd like to thank the faculty at USM for teaching me, from scratch, the many fundamentals of polymer science.

Primary financial support of this research was from the Center for Layered Polymeric Systems Center (CLiPS), DMR 0423914, the National Science Foundation's (NSF) Graduate STEM Fellows in K-12 Education (*GK-12 Fellowship),* the Robert M. Hearin Foundation and the Bryce Corporation.

TABLE OF CONTENTS

LIST OF TABLES

LIST OF ILLUSTRATIONS

LIST OF SCHEMES

CHAPTER I – A BRIEF OVERVIEW

Nature provides us with countless examples of the potential of using layered structures to enhance the properties of a material when compared to its individual components. The possibilities seem endless in the study of these layered structures and how they could be realized to meet a plethora of applications from readily available materials. The goal of this dissertation is to show and understand how through use of layered nanoplatelets in a multilayered film one can create polymeric films that exhibit properties that, like nature, outperform their constituent materials. Also we will show how the layered morphology of intercalated nanoplatelets has a unique and profound effect on the thermal and physical properties of a polymer matrix.

To create new and exciting materials with enhanced properties, particles with one or more dimensions in the nanometer range are commonly added to a bulk polymer phase. The inclusion of these nanoparticles can dramatically enhance many material properties such as aesthetic, mechanical, thermal, optical, electrical, and gas barrier properties. Even a small addition of nanoparticulates can impart surprisingly large changes in the macroproperties of the nanocomposite material. Of particular interest in this dissertation is the use of high aspect ratio platelets to impart gas barrier properties. However, our methodology could also be utilized to produce other smart materials including highly conducting, drug delivery, or bioactive films. Inexpensive high gas barrier films, for instance, are highly desirable in the food packaging industry to limit oxygen diffusion that promotes food decomposition and in the electronics industry to prevent oxygen and water vapor contamination that is detrimental to many sensitive electronic devices.

As mentioned, one of the primary focuses of this dissertation is in increasing the gas barrier properties of highly commercialized polymeric films through the addition of high aspect ratio nanoplatelets (i.e, montmorillonite and graphene). Particulate filled polymer systems are commonly used in the reduction of a polymer's permeability/enhancement of barrier properties. Platelets, flakes, tubes, and fiber composites have all been implemented to increase the barrier properties of a polymer matrix and many models have been derived to describe how the dispersal of nanosized fillers affects the gas transport properties of a polymer film.

The permeability (P) of a material is dependent on the solubility (S) of gas molecules into the material and the diffusivity (D) of the gas molecules through it ($P=D\cdot S$). The theoretical models center on the idea that the diffusivity of a penetrant is affected by the tortuous diffusion pathway or multiple reflections between the virtually impermeable filler. The gas molecules must diffuse around the impermeable particles instead of taking a direct route from surface to surface. As the permeability is a product of both the solubility and diffusivity of a system, one mechanism of reducing the permeability of a system is to lessen the diffusivity.

The models that predict gas diffusion through polymer composites containing disc-shaped fillers suggest that the characteristic distance between the particles controls the barrier properties. Nanocomposites are thought to exhibit very different diffusion behaviors depending on the concentration and spacing of the particles. For instance, when the disks are spaced at distances much exceeding the disks' radii (dilute regime), diffusion is described by a formula devised by Nielsen [1]. When the particles are more concentrated, where the disks are spaced at distances comparable or smaller than their

radii (semi-dilute regime), diffusion can be more accurately described by a separate model devised by Cussler [2]. This transition can be ascribed to the increased significance of the scattering of the penetrants between close pairs of disks in this more concentrated regime. These scatterings add considerably to the decrease of overall diffusivity and subsequently permeability of the composite.

Thus, it can be advantageous for barrier enhancement, while keeping the mineral content the same, to disperse particulates unevenly in a layered structure where polymer layers containing the particulates in the semi-dilute regime are alternated with unfilled layers of polymer. Our research group has shown that multilayer co-extrusion processing can be successfully utilized in creating such layered structures. Additionally, the stringent melt flow conditions associated with the multilayer extrusion typically leads to orientation of the particulates perpendicular to the film surface. Particulate alignment can also have a drastic impact on the gas barrier properties of nanocomposites.

Attaining this semi-dilute regime can be problematic with some nanoplatelet materials. For instance, clay platelets (i.e. montmorillonite) impart significant melt viscosity increases upon being added to a polymer resin. This viscosity increase can be beneficial in some applications; for instance, the use of clay platelets as paint viscosifiers or flow modifiers. However, high viscosities are typically problematic in melt processing, the most commercially relevant process of making polymeric films, requiring high energy consumption and specialty equipment.

To overcome these limitations, we demonstrated that the controlled interdiffusion of a polymer pair in microlayers can be employed to increase the concentration of inorganic particles included in one of the component layers. Thus, the need for initially

highly concentrated composites would be eliminated in favor of careful polymer selection in the microlayers. Kramer first demonstrated this phenomenon, resembling the Kirkendall effect in metals, through his work with polystyrene bilayer polymer pairs of different molecular weights [3-4]. He showed that the polymer layer interface moved toward the polymer with the lower molecular weight upon interdiffusion in the melt. It was concluded that the boundary movement was a result of an unequal flux of polymers across the interface balanced by a net flux of vacancies. As interdiffusion in the melt is a relatively slow phenomenon, the use of a multilayer system proved highly beneficial due to the ability to create films with large numbers of interfaces and thin layers. This allowed the interdiffusion to reach equilibrium in a reasonable experimental timescale.

Multilayer films are co-extruded in a system that typically consist of multiple single screw extruders with melt pumps, a co-extrusion block, a series of layer multiplier elements, and a film die. The melt streams are combined in the feedblock as parallel layers. From the feedblock the layers flow through a series of layer multiplying elements, with each multiplier element doubling the number of layers by first slicing the layers vertically, then spreading them horizontally, and finally recombining. Extruded films can vary from 1-2 mm thick tape to as thin as 25 μm with layer thickness down to less than 100 nm.

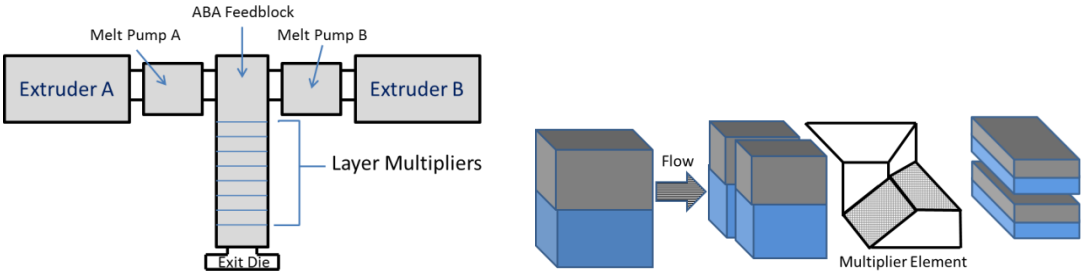

Scheme 1.1 Schematic of multilayer coextrusion process

Control of the melt viscosity and melt viscosity ratio of the multilayered polymers is crucial in the production of quality uniform layers. Polymer melt flow is laminar and flows in discrete layers. The laminar flow keeps the different polymer layers from mixing. If the polymers in the different layers have similar viscosities, the layer structure should uniformly exit the dye. A mismatch in viscosity will lead to interfacial instability and encapsulation of the higher viscosity material by the lower viscosity material. Therefore, considerable effort was taken to match viscosities as close as possible

Our groups' previous research demonstrated that the before mentioned interdiffusion phenomenon could be observed in various other polymeric systems where the molecular mobility of the diffusing polymer chains could be affected by many factors including molecular weight and structural differences (i.e. branching structure). For instance, when microlayers of linear low density polyethylene (LLDPE) and low density polyethylene (LDPE) were taken into the melt, the greater mobility of the more linear LLDPE chains compared to the longer branched LDPE chains caused the layer boundary to move in the direction of the more slowly diffusing chains. This resulted in substantial shrinkage of the LLDPE layers. If particles were dispersed in the LLDPE phase, the resultant shrinkage dramatically increased the particle concentration [5].

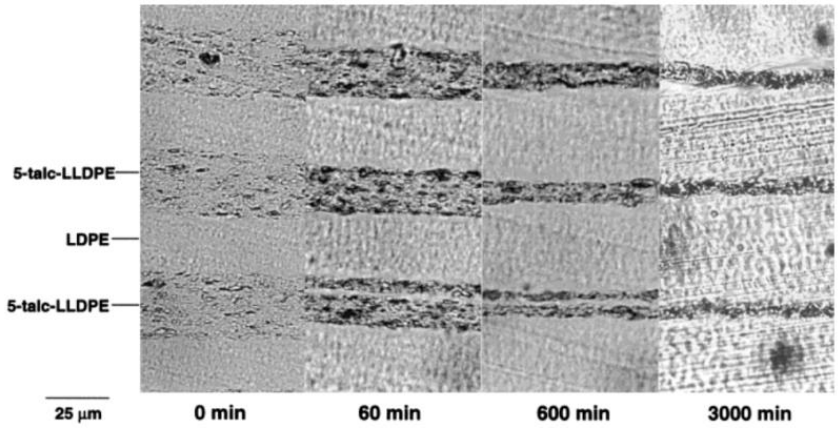

Figure 1.1 Optical micographs of 5 vol% talc + LLDPE/ LDPE multilayer system annealed at 200°C for indicated time [5].

As mentioned, the primary focus of this dissertation is an extensive analysis of layered high aspect ratio nanocomposite materials. The research in this document spans from a study of co-extruded multilayered nanocomposites for barrier applications to a thermal and free volume analysis of nanocomposites comprised of layered clay platelets intercalated with amorphous hyperbranched polymer. Knowledge gained from this research could have immediate applicability in barrier film applications including food, beverage, and electronic packaging along with niche smart materials in the fields of drug delivery and diagnostics, for example. Further, pertinent background information relatable to this dissertation can be found in Chapter II.

This research is divided into five primary objectives. The objectives focus on expansion/ fundamental understanding of the interdiffusion and moving boundary process in multilayered LDPE/ LLDPE systems with a particular emphasis on creating high barrier polymer films through implementation of LLDPE composites. The objectives also detail a goal of analyzing how clay platelet/ polymer interactions affect

the physical properties of a model intercalated nanocomposite system. The objectives are detailed as follows:

1) To develop a fundamental understanding of factors that control the extent of interdiffusion and moving boundary effect in olefin based LLDPE/LDPE multilayers (i.e., composition, morphology, polymer/ nanoparticle structure).

2) To conduct a processing optimization study which would allow nanoplatelets, including montmorillonite and graphene sheets, as well as low-T_g phosphate glass beads to be dispersed in a LLDPE matrix.

3) To fabricate LDPE/LLDPE multilayer composites containing inorganic particulates and to study interdiffusion, moving boundary and particle concentration effects in these systems.

4) To investigate the physical properties of particulate filled composites and multilayers; i.e. gas transport, mechanical, and fire retardancy. To relate the studied physical properties to the layer structure and particulate morphology.

5) To investigate the thermal and physical property changes in an intercalated nanoplatelet/ model amorphous hyperbranched polymer composite. To relate these property changes to the morphology of the intercalated nanoplatelets.

Chapters III, IV, and Appendix I all focus on co-extruded multilayer nanocomposite films for increased barrier properties. Through a considerate selection of the polymers utilized in multilayer films of alternating pure polymer (LDPE) and polymer nanocomposite layers (LLDPE), melt induced asymmetric interdiffusion was

harnessed to increase the particulate concentration in the nanocomposite layers. This resulted in enhanced gas barrier properties in these films that are typically only observed in highly difficult to process composites of much higher loadings.

Chapter III is a continuation of our group's research focused on montmorillonite (MMT) clay platelet nanocomposites in multilayered films. An in-depth nanocomposite and multilayer morphological study was combined with gas transport analysis to monitor the interdiffusion driven shrinkage of the nanocomposite layers with annealing time. This compaction of the nanocomposite layers and the resulting morphology of the concentrated clay platelets resulted in improvement of gas barrier properties over materials with much higher clay loadings [6].

Along with the success of the work in Chapter III, there were some areas of improvement and questions left unanswered for further studies. For instance, extra steps were needed to modify the montmorillonite and LLDPE polymer in the nanocomposites to achieve full exfoliation of the platelets. It was of interest to determine if these small amounts of modifiers affected the interdiffusion kinetics of the polymers. Also, addition of montmorillonite to the polymer matrix resulted in large viscosity increases in the composite. This limited the amount of initial clay added to the system and made processing pure polymer multilayer controls not possible. Viscosity matches of the resins used in the multilayer coextrusion must closely match to achieve distinct uniform layers. In our system, the polymer in the nanocomposite layers had to be of much lower viscosity than the polymer in the unfilled layers to compensate for the viscosity increase brought on by the addition of the clay particles. Finally, the initial small aspect ratios of the clay

particles hindered us from reaching the regime of drastic, multiple orders of magnitude, improvement that is predicted in our modeling for high aspect ratio platelets.

We attempted to address these issues in the research of Chapter IV, where high aspect ratio graphene nanoplatelets were utilized in a similar multilayer system. However, no modification of the graphene or the polymers was implemented. The graphene utilized had a much larger aspect ratio than the before studied MMT particles, up to 25 μm in length as compared to ~100 nm for the MMT platelets. Also, the graphene proved to impart much smaller increases in viscosity to the polymer resins enabling larger initial concentrations of particulates to be co-extruded into multilayer films. Pure polymer multilayers could also be processed for this system as the drastic viscosity differences in polymers was not necessary. Barrier property improvement, including fire barrier properties, were analyzed for the composites and multilayered systems in a similar manner to Chapter III.

The multilayered graphene composite systems showed layer movement/ shrinkage of the nanocomposite layers upon annealing similar to the work in Chapter III. However, achieving the initial exfoliated dispersion state proved problematic. This lead to aggregation of graphene particles upon melt mixing with LLDPE and thus limited gas barrier enhancement. The graphene nanoplatelet composites and annealed multilayered composites did achieve barrier property enhancement that outperformed similar graphene-polyolefin systems found in the literature.

The work in Appendix I utilized the same particle concentration method employed in Chapters III and IV but with low T_g phosphate glass as the filler. The phosphate glass, with a T_g below that of the melt processing temperature, could be added

to the LLDPE up to very high concentrations as the glass was fluidic at the melt mixing temperature. The goal of the work was to promote glass coalescence into high aspect ratio impermeable sheets upon melt induced particle concentration. In reality, we were never able to overcome the thin polymer layers in between the glass droplets and thus ended up with layers of highly aligned glass spheres post interdiffusion.

Finally, the last chapter of this dissertation, Chapter V, focuses upon the thermal and free volume properties of a layered clay nanocomposite system intercalated with amorphous hyperbranched polyester (HBP). Changes in the composites' glass transition (T_g) and the heat capacity (ΔC_p) at T_g with clay concentration were correlated with clay platelet morphological observations including the clay's intercalation interlayer spacing. From the ΔC_p thermal analysis, weight fractions of the amorphous phases of the polymer, i.e., a mobile amorphous fraction (MAF) and a corresponding mobility suppressed rigid amorphous fraction (RAF) could be calculated. Results demonstrated that changes in the RAF and MAF content depend not only on the clay volume fraction but also on clay morphology. Lastly, in this chapter, a novel approach to estimate MAF and RAF concentrations via positron annihilation spectroscopy (PALS) from the thermal expansivities of free volume hole sizes in the liquid and glassy states was demonstrated and proved consistent with values calculated from the thermal analysis [7].

References

1] Nielsen, L. E., J. Macromol. Sci. (Chem) 1967, A1 (5), 929.

2] Cussler, E. L.; Hughes, S. E.; III, W. J. W.; Aris, R., Barrier Membranes. Journal of Membrane Science 1988, 38, 161-174.

3] Green, P. F.; Palmstrom, C. J.; Mayer, J. W.; Kramer, E. J., Marker Displacement Measurements of Polymer-Polymer Interdiffusion. Macromolecules 1985, 18, 501-507.

4] Kramer, E. J.; Green, P.; Palmstrom, C. J., Interdiffusion and marker movements in concentrated polymer-polymer diffusion couples. Polymer 1984, 25, 473-480.

5] Nazarenko, S.; Dennison, M.; Schuman, T.; Stepanov, E. V.; Hiltner, A.; Baer, E., Creating Layers of Concentrated Inorganic Particles by Interdiffusion of Polyethylenes in Microlayers. Journal of Applied Polymer Science 1999, 73, 2877-2885.

6] Decker, J. J.; Meyers, K.P.; Paul, D.R.; Schiraldi, D.A., Hiltner, A.;Nazarenko, S., Polyethylene-based nanocomposites containing organoclay: A new approach to enhance gas barrier via multilayer coextrusion and interdiffusion: Polymer 2015, 61, 42-54.

7] Meyers, K.P.; Decker, J.J.; Olson, B.G.; Lin, J.; Jamieson, A.M.; Nazarenko, S., Probing the confining effect of clay particles on an amorphous intercalated dendritic polyester: Polymer 2017, 112, 76-86.

CHAPTER II - RESEARCH BACKGROUND

Project Rationale

Packaging materials have historically been comprised of metal, paper, and glass, but are increasingly being replaced by light weight, low cost, easily processed polymeric materials. Unfortunately, many mass produced inexpensive polymers are less effective than desired in regards to gas barrier properties, especially polyolefins which exhibit relatively poor oxygen barrier. The deficiency of these pure polymers, in regards to gas barrier and other desired mechanical properties, drove this research of polymer nanocomposites in an effort to improve on the properties of polymers that are already commercially utilized.

High gas barrier films are crucial in the food packaging industry to protect and preserve food that will not be consumed immediately after production. These films need to be able to protect the contents from permeants that range from large dirt and dust particles to small gas molecules that expedite decomposition. Along with the barrier properties, the films need to be durable and able to withstand the conditions associated with filling and storing the containers. Therefore, traditional food packaging polyolefins were analyzed to increase their gas barrier properties, while keeping their light weight, ease of processing, and mechanical properties that are beneficial in the packaging industry.

In this project we continue an investigation of the utilization of co-extruded multilayer films with layers of particulate filled nanocomposites to increase a polymer film's barrier properties without the negative drawbacks typical of high loading nanocomposites including lack of polymer toughness and processing difficulties.

Multilayer coextrusion is a cost effective processing technique that can be used to combine the physical properties of multiple polymers. This is crucial as polymeric systems may need to meet multiple requirements for transparency, contact with food, package sealing, and/or gas barrier. Polymer strength, flexibility, gas barrier properties, and FDA approval are thus of vital importance [1].

Through multilayering alternating layers of different polymeric materials in layer sizes from micrometers to nanometers, one is able to achieve a synergistic combination of material properties. In this study, two inexpensive, easily processable, readily available resins, LLDPE and LDPE, which differ only in their branching structure, were utilized as base resins in the microlayer films.

If a system of alternating layers of polymers with highly different molecular mobilities (i.e. LLDPE and LDPE) is taken into the melt, convective flow (a moving boundary phenomenon) of the more slowly diffusing material can be observed opposite to the faster diffusing molecules in order to relax the sudden increase in density from the diffusion of the more mobile molecules into the sluggish polymer phase [2]. If the more mobile polymer phase is loaded with high aspect ratio platelets, gas barrier improvement can be observed with the depletion of those polymer layers and thus concentration of the platelets, creating a highly torturous pathway for diffusing gas molecules. This effect has previously been demonstrated in LLDPE/ LDPE multilayer systems as LLDPE, with its numerous short branches, has been shown to be more mobile than the long branched LDPE polymer [3].

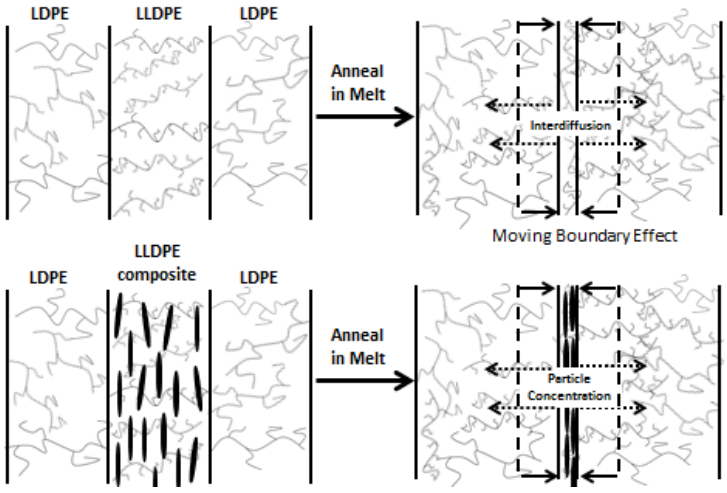

Scheme 2.1 The moving boundary effect/ particle concentration that takes place as the LLDPE diffuses faster into the LDPE when heated into the melt.

Prior research on monitoring the interdiffusion progression of these two polymers is limited to tracking the convergence of the polymer melting peaks through thermal analysis [3]. However, various experimental techniques have been used to measure mutual diffusion coefficients in other systems including fluorescence nonradiative energy transfer [4], positron annihilation lifetime spectroscopy (PALS) [5], ellipsometry [6], pulsed field gradient-nuclear magnetic resonance (PFG-NMR) spectroscopy[7], energy-filtering transmission electron microscopy (EFTEM)[8], asymmetric double beam cantilever test (ADBC) [8], X-ray microanalysis in scanning electron microscopy [9], small-angle neutron scattering [10], dynamic secondary ion mass spectroscopy (DSIMS) [11], neutron reflection [11], neutron spin echo [12], nuclear reaction analysis (NRA) [13-14], forward recoil spectrometry [15], Rutherford backscattering spectrometry [16-17], Fourier transform infrared spectroscopy (FTIR) [18-19], rheometry [20-21], and transmission electron microscopy (TEM) [22]. The analytical tools being implemented in this research to track interdiffusion and determine the properties affecting the rate and completion of interdiffusion include layer thickness analysis through optical and

transmission electron microscopy. These techniques do not require chemical labeling, making them a better representation of the actual polymeric diffusion process.

The particle concentration brought on through imbedding particulates in the more mobile polymer phase (LLDPE) allow for nanocomposite concentrations in the shrunken LLDPE layers that would not be possible to reach from any other common melt processing technique. Nanocomposites increase in viscosity with filler concentration, thus high content composites which are beneficial for gas barrier improvements are typically very difficult to process.

Multilayered Materials in Nature

Multilayered materials with increased mechanical and barrier properties are prevalent in biological structures and have been utilized by mankind for thousands of years. Laminated steels date back to the first millennium B.C. in the forging of Japanese swords which were strong in compression while remaining very tough [23]. In nature many organisms developed multilayered structures over hundreds of millions of years to exhibit exceptional structural properties despite primarily consisting of quite brittle materials. These structures are typically composites of organic (proteins/ polysaccharides) and inorganic (minerals) components but have properties that drastically outperform their relatively weak constituents.

A few biological examples with these multilayered structures include the abalone nacre, crab exoskeletons, chiton radular teeth, squid beaks and arapaima scales [24]. For instance, the nacre (mother-of-pearl) shell consists of 95% aragonite (a mineral form of $CaCO_3$); however, through use of a multilayered structure and a few percent biological

macromolecules it has a work of fracture 3 orders of magnitude higher than monolithic ceramics [25]. Another example, the scales of the arapaima, one of the largest freshwater fish on earth, exhibit an advanced multilayer structure with enhanced mechanical properties capable of withstanding a bite from its ecosystem cohabitant, the piranha. The scales consist of a highly mineralized external layer and an internal layer, both consisting of collagen fibers. The cross-lamellar arrangement of mineralized fibers on the external layer provides the hardness and wear resistance requisite for the armor protection. The internal layers provide the flexibility and toughness [24,26].

Layered Polymeric Systems

Coextruded multilayer polymer films and composites have been used for many years to try to replicate the enhanced mechanical and structural properties of the before mentioned biological structures. The carefully controlled flow conditions that are required for microlayer coextrusion attempt to achieve this through the combination of different polymers with very little to no mixing [27]. Two or more polymers can be combined as tens, hundreds, or even thousands of alternating layers with layer thickness ranging from microns to tens of nanometers [28].

Layered polymeric systems are important in achieving films that exhibit a desired mix of end-use characteristics. Polymers with widely dissimilar properties can be combined into multilayered structures that exhibit a synergistic combination of properties, when the layers are thin enough, that would be unavailable in a single material. Mechanical, optical, gas barrier, electronic and aesthetic properties can all be improved through multilayering. Multilayer films also provide a unique research tool for studying phenomenon including interdiffusion, crystallization, and adhesion due to their

large interface to volume ratio. Originally, commercially available multilayer films were produced from single layer films that were stacked together through several lamination processes. This method is impractical and expensive; therefore, the most rapid and industrially relevant process for producing these multilayer films is from the co-extrusion of two or more polymers in a multilayer co-extrusion process.

Multilayer films are co-extruded in a system that consists of two single screw extruders with melt pumps, a coextrusion block, a series of layer multiplier elements, and a film die as seen in Scheme 1.1. The metering pumps control the two melt streams which are combined in the feedblock as two parallel layers. From the feedblock the layers flow through a series of layer multiplying elements, with each multiplier element doubling the number of layers by first slicing the layers vertically, then spreading them horizontally, and finally recombining. An assembly of *n* multiplier elements produces a film with $2^{(n+1)}$ layers. Extruded films can vary from 1-2 mm thick tape to as thin as 25 μm with layer thickness down to less than 100 nm.

Control of the melt viscosity and melt viscosity ratio of the multilayered polymers is crucial in the production of quality uniform layers. Polymer melt flow is laminar and flows in discrete layers. The laminar flow keeps the different polymer layers from mixing. If the polymers in the different layers have similar viscosities, the layer structure should uniformly exit the dye. A mismatch in viscosity will lead to interfacial instability and encapsulation of the higher viscosity material by the lower viscosity material. Therefore, considerable effort must be taken to match viscosities as close as possible through material selection and temperature control of extruders and melt pumps [1].

There are numerous examples of achieving significant physical properties improvement in multilayer films, without sacrificing other important properties, as compared to traditional processing techniques. Co-extruded layered films have been produced having heat sealable polyethylene skin layers and a saran core layer for gas barrier [29]. Multilayering polycarbonate (PC) and the brittle styrene-acrylonitrile copolymer (SAN) resulted in a ten-fold enhancement in toughness and impact strength when the layer size was reduced to several microns [30]. Enhanced mechanical properties, including increases in modulus and elongation at fracture, were observed in talc-filled polypropylene alternated with layers of unfilled polypropylene. Conductive nickel flake-filled polypropylene films alternated with insulating polypropylene demonstrated anisotropy in resistivity improvements of ten orders of magnitude when microlayered [31].

Coextrusion multilayered films are currently being researched to produce a variety of low-cost, easily fabricated, and commercially viable materials. Gradient refractive lens (GRIN) material made out of multilayered polymethylmethacrylate (PMMA) and poly(styrene-co-acrylonitrile) (SAN17), with a reduced weight and volume as compared to typical inorganic lenses, possess enhanced focusing power and superior aberration correction when compared to traditional monolithic lenses with a single refractive index [32]. Multilayered coextruded films are also being implemented for optically-pumped all-polymer distributed feedback (DFB) surface-emitting lasers through uses of hundreds of alternating layers of transparent polymers SAN25, with a laser dye, and a fluoroelastomer terpolymer of vinylidene fluoride, hexafluoropropylene, and tetrafluoroethylene (THV) [33].

Addition of another co-extrusion system that adds a thin layer of a third polymer between the layers of polymer A and polymer B can also be utilized to achieve acceptable interlayer adhesion. The addition of a compatibilizer as this tie layer at the interface of two dissimilar polymer allows for better layer adhesion in the multilayering of two immiscible and incompatible polymers. For example, this technique was implemented to combine the ductility of polypropylene with the high yield strength of polyamide through the addition of a maleated polypropylene tie layer [28].

Interdiffusion/ Moving Boundary Effect in Bilayers and Multilayers

As mentioned, multilayer films provide a unique platform to study phenomenon including polymer interdiffusion. Polymeric interdiffusion is the diffusion among distinguishable molecules and is typically very slow, 10^{-16} to 10^{-10} m^2/s. Interdiffusion is vital in the understanding of the rate of composition inhomogeneity disappearance and how it depends on molecular structures. Interdiffusion is influenced by thermodynamic and frictional factors including molecular weight, molecular weight distribution, composition, temperature, chain orientation and the molecular structure of the polymer. These factors have a profound effect on the shape of the concentration profile across the interface as interdiffusion proceeds. Polymer pairs with dissimilar properties can show an asymmetric concentration profile about the interface as one polymer diffuses more quickly into the other polymer. Multiple review articles are available that detail interdiffusion at polymer/polymer interfaces [2, 34-35].

The rate of disappearance of the gradient in inhomogeneous systems moving toward homogeneity is defined by the mutual diffusion coefficient, D_m, and is explained by Fick's law of diffusion ($-J_i = D_m \Delta c_i$). Fick's law relates the flux, J_i, to the concentration

gradient, Δc_i, in moles of molecules per unit volume. An experimental route for the determination of the mutual diffusion coefficient is to map out the concentration profiles from interdiffusion of two species and extract D_m from the diffusion equation obtained from inserting Fick's law into a species mass balance as shown in Equation 2.1

$$\partial c/\partial t = \partial/\partial x(D_M(c)\,\partial c/\partial x) \tag{2.1}$$

Early studies of the diffusion of macromolecules across polymeric interfaces consisted primarily of analysis of bilayers of thin films. Bilayer films were formed from stacking polymer components and then annealed for analysis of interdiffusion kinetics of polymers across the interface. Bilayer systems left much to be desired in regards to contact area and the number of interfaces between the materials.

The modeling of the interdiffusion process of polymers across an interface has been of critical interest for many years. Brochard-Wyart et al. derived the slow-mode theory to describe interdiffusion at polymer interfaces, assuming the fluxes of the two components were equal but opposite. This theory predicts that interdiffusion is dominated by the slower-diffusing polymer and that the interface should remain symmetric as interdiffusion proceeds for symmetric boundary conditions. The slow-mode theory is described in Equation 2.2, where D is the interdiffusion coefficient, Λ_A and Λ_B are the mobilities of polymers A and B, N_A and N_B are the number of repeat units of each polymer, ϕ_A and ϕ_B are the molar fraction of each polymer, and χ is the Flory-Huggins interaction parameter.

$$D = \left(\frac{\Lambda_A \Lambda_B}{\Lambda_A + \Lambda_B}\right)\left(\frac{1}{\phi_A N_A} + \frac{1}{\phi_B N_B} + 2\chi\right) \tag{2.2}$$

Kramer demonstrated in his work on PS/d-PS that for polymer pairs with different molecular weights, the interface could move toward the polymer with the lower molecular weight during interdiffusion in the melt. Kramer [36] and Sillescu [37] concluded that the moving boundary was caused by an unequal flux of polymers across the interface that was balanced by a net flux of vacancies. Assuming the vacancies' chemical potential was zero in the melt state but the flux of the vacancies was finite, they derived the "fast-mode" theory (Equation 2.3) that indicates the interdiffusion coefficient is dominated by the faster-moving component [16].

$$D = \phi_A \phi_B \left(\frac{\phi_B}{\phi_A} \Lambda_A + \frac{\phi_A}{\phi_B} \Lambda_B \right) \left(\frac{1}{\phi_A N_A} + \frac{1}{\phi_B N_B} + 2\chi \right) \qquad (2.3)$$

It was suggested, and experimental data from the literature mostly agrees, that the fast-mode theory describes interdiffusion above the T_g while the independently derived slow mode-theory describes interdiffusion below the T_g [34]. Kramer first observed this moving boundary phenomenon through the use of Rutherford backscattering to follow the movement of gold markers situated at the interface of PS and d-PS of different molecular weights. They observed that the gold markers moved toward the faster diffusing component (lower molecular weight polymer) [16, 36].

Jabbari and Peppas also observed this moving boundary phenomenon for chemically dissimilar polystyrene and poly(vinyl methyl ether) bilayers with interdiffusion through FTIR spectroscopy with an ATR accessory. The concentration profiles at 125°C for the PS/PVME pair were asymmetric with substantial swelling of the slower-diffusing component by the faster-diffusing component [34].

Multilayer coextrusion has also been implemented for interdiffusion studies and has several advantages over the bilayer system analysis. Larger contact area and greater number of interfaces between materials can amplify the effect of interdiffusion where more common characterization techniques can be implemented and complete layer diffusion can be concluded in reasonable experimental time scales.

Prior interdiffusion studies of polymeric multilayers include miscible PC and PET [38], molecularly similar HDPE and LLDPE [27, 39], and PMMA and SAN17 [32]. The PC/PET multilayered system comprised of hundreds to thousands of layers was analyzed through a convergence of the glass transition temperature when annealed into the melt. A model based on Fick's law of diffusion was used to describe the mutual diffusion at the layer interface and provide a reasonable prediction of experimental results [38]. DSC melting peak convergence analysis of HDPE/ LLDPE multilayer systems required a modification of the previously derived model to take into account the effect of molecular weight distribution, especially the high molecular weight tail [27, 39]. Work by Dr. Baer's Research Group studied the use of interdiffusion of two materials to fabricate polymeric gradient refractive index (GRIN) lenses by varying contact time during multilayer coextrusion of poly(methylmethacrylate) (PMMA) and poly(styrene-coacrylonitrile) (SAN17). Their model successfully described the interdiffusion with various contact times for the determination of the mutual diffusion coefficient. This knowledge would allow for GRIN lenses fabrication optimization or to be utilized in novel designs of gradient refractive index optics [32].

This research project focuses on the utilization of alternating layers of different polymers (LLDPE and LDPE) with mismatched diffusion coefficients. By taking this

system into the melt, one is able to observe the phenomenon described by Kramer, a movement of interfacial boundaries in the direction of the faster diffusion component. As the more mobile chains diffuse into the regions of less mobility, osmotic pressure drives the bulk flow which results in a movement of the polymer boundary layers similar to the Kirkendall effect in metals [27]. The polymer interdiffusion, activated by heating the system into the melt state, gradually creates a gradient blend of compositions with maxima and minima concentrations located at the initial centers of the layers [27].

The moving boundary phenomenon observed through interdiffusion of alternating LLDPE/LDPE films can be exploited to fabricate high gas barrier films containing layers of highly concentrated particles if high aspect ratio particulates are dispersed in the LLDPE phase. It has been demonstrated that for alternating multilayers of LLDPE filled with inorganic platelets and LDPE, when taken into the melt, the greater mobility of short branched LLDPE chains relative to long branched LDPE chains causes a mismatch in diffusion coefficients between the polymer layers. This results in shrinkage of the LLDPE layers and the particle concentration phenomenon [3]. Multilayer co-extrusion processing has been successfully applied for creating these particulate filled layered structures. This behavior has been demonstrated with nickel platelets [3], TiO_2 particles [3], talc platelets [3], organically modified montmorillonite, synthetic mica, graphene and through preliminary studies utilizing low T_g phosphate glass.

Gas Permeability

The permeability of a polymeric material is dependent on the solubility of gas molecules into the matrix and the diffusivity of the gas molecules through the matrix ($P=D\cdot S$). Particulate filled polymer systems are commonly used in the reduction of a

polymer's permeability/ enhancement of barrier properties. Extensive research has been conducted on the effect of particulates dispersed in a polymer matrix on the system's permeability. Neilsen [40], Cussler [41], Fredrickson [42], and Gusev [43] have all derived equations to model how the dispersal of nanosized fillers affects the barrier properties in a polymer film. The models center on the idea that diffusivity of a penetrant is affected by the tortuous diffusion pathway or multiple reflections between the virtually impermeable filler. The gas molecules must diffuse around the impermeable particles instead of taking a straight path from surface to surface. Permeability is a product of the solubility and diffusivity of a system and therefore as the diffusivity is decreased, the permeability also decreases.

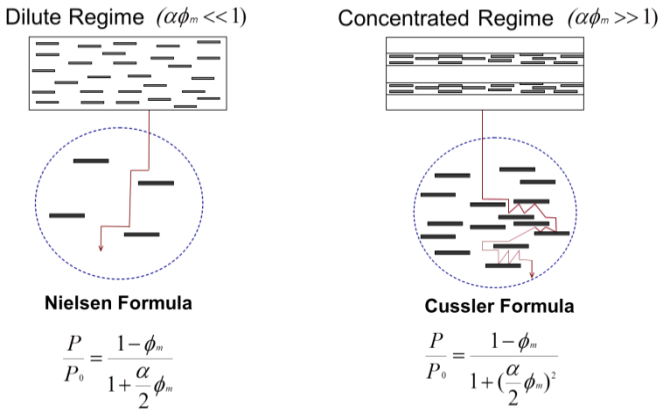

Scheme 2.2 Theoretical predictions of the relative permeability (P/P_0) of platelet filled nanocomposites as a function of platelet aspect ratio (α=L/h) and volume fraction (ϕ_m). (Neilsen is simplest model but only useful for ϕ_m<10%)

Platelets, flakes, tubes, and fiber composites have all been utilized to increase the barrier properties of a polymer matrix. The geometric constraints imposed by the multilayering process generally orient the particles parallel in the plane of the layers [3]. Multilayered polymer films with alternating layers of the particulate filled more mobile polymer layer and the unfilled less mobile layer can be utilized to create layered

structures with highly concentrated layers of inorganic particles [3]. The moving boundary effect takes place as the more mobile polymer diffuses into the less mobile phase, leaving behind the filler. This concentrated filler layer imparts substantial increases in the polymer film's barrier properties as the penetrants pathway becomes significantly more tortuous.

Theoretical predictions of gas diffusion through polymer composites containing evenly spaced disc-shaped fillers suggest that the characteristic distance between the particles and the particles' aspect ratio will control barrier properties [42, 44]. Therefore, through a transition from dilute particle conditions, where the disks are spaced at a distance much exceeding the disk radius *R* (Nielsen [40]) to semi-dilute conditions, where the disks are spaced at distances comparable or smaller than *R* (Cussler [41]), the diffusivity can be greatly reduced. The increased role of repeated multiple scattering of penetrants between close pairs of disks in the semi-dilute regime can lead to a further decrease in overall diffusivity and subsequent permeability of a composite. Hence, it can be advantageous for barrier enhancement to disperse particulates unevenly by creating a layered structure where polymer layers contain high aspect ratio particulates in the concentrated regime, alternated with unfilled layers of polymer.

Nanocomposite Morphology

Layered nanoplatelets (i.e. montmorillonite, synthetic mica, and graphene) typically fall into three levels concerning their dispersion in polymeric media. The first level is the phase-separated state where polymer chains cannot penetrate between individual layer sheets. The composite is thus only considered a microcomposite and the increased properties associated with nanocomposites are not achieved. As demonstrated in the

Neilsen and Cussler models, agglomeration of nanoparticulates into microcomposites with reduced aspect ratios will greatly reduce the barrier efficiencies of the nanocomposites. The next level is the intercalated morphology where polymer chains are able to interpenetrate the nanoparticulate layers. Finally the last (and typically most desired) level of dispersion is a fully exfoliated composite. In this nanocomposite system, property enhancement is maximized [45].

Exfoliated and highly dispersed nanocomposites are extremely difficult to prepare in a nonpolar polyolefin matrix. Van der Waals forces and surface energy differences can cause the nanoparticles to have a stronger affinity toward each other than the polymer matrix they are dispersed in. This self-affinity leads to problems associated with agglomeration and thus loss of nanocomposite barrier properties. Various processing and modification techniques can be used to alleviate this problem.

The protocols in which the nanocomposites are fabricated play a crucial role in how the nanoparticulates are distributed in the polymer matrix, and thus the barrier properties. Typical nanocomposite compounding techniques include *in situ* polymerization, solvent processing, and melt processing. With *in situ* polymerization's high energy consumption and solvent processing's unfavorable environmental impact, melt processing typically proves to be the most direct, environmentally friendly, and cost effective method of creating polymer nanocomposites, but not necessarily the most effective in creating high nanoparticulate dispersions.

Polymer modification (i.e., maleic anhydride grafted polyethylenes) and nanoparticulate surface modification (i.e., functionalization of polar nanoclays with

organic ammonium ions bearing long aliphatic chains) have been investigated for optimization of filler dispersion in the LLDPE matrix.

Rigid Amorphous Fraction

As mentioned, polymer clay nanocomposites often exhibit chemical and physical properties that are superior to those of conventional composite materials [46-48]. While a completely exfoliated nanocomposite system is typically desirable, intercalated nanocomposite systems can prove quite interesting and impart some property enhancement as well. Therefore, we studied the incorporation of model amorphous dendritic hyperbranched polyester polyols (HBP) into clay galleries and probed the resulting polymer-substrate interactions by bulk techniques.

The confinement of collapsed HBP between multiple clay layers results in a sizable amount of immobilized polymer. The nature of this immobilized polymer is viewed as analogous to the concept of a rigid amorphous fraction (RAF) in semi-crystalline polymers, introduced to explain an observed discrepancy between the degree of crystallinity and the change in heat capacity, ΔC_p, at the glass transition, T_g [49]. The RAF represents the fraction of the amorphous phase that does not contribute to the change in ΔC_p at either the T_g or T_m (melting). It is well-established [49-61] that the RAF is due to an immobilization of the disordered polymer chains that connect the crystalline lamellae. These chains are unable to undergo long range translational motions when crystalline constraints are imposed during crystallization of the polymer melt, implying that the RAF vitrifies in the vicinity of the crystallization temperature, T_c. In contrast, the un-constrained amorphous chains, the mobile amorphous fraction (MAF), remain in the

molten state at T_c and vitrify upon cooling at the regular T_g. Complete devitrification of RAF occurs at T_m.

It is also established that the immobilized amorphous phase in nanocomposites exhibits some of the characteristics of a RAF, such as the suppression of the glass transition [62-65]. Unlike crystalline phases, however, inorganic clay does not melt within the thermal stability range of the polymers. This means that, if the interactions between polymer and inorganic substrate are maintained at elevated temperatures, devitrification of the immobilized chains does not occur [62]. Since MMT exhibits no thermal transitions within the investigated temperature ranges, it is ideally suited to investigate polymer immobilization solely at the clay interfaces. Heat capacity measurements were used to quantify the amount of RAF as described by Wunderlich et al. for semicrystalline polymers [49]. To probe the structure of the RAF, free volume measurements using positron annihilation life-time spectroscopy (PALS) were employed.

Positron Annihilation Life-time Spectroscopy (PALS)

PALS is a well-established, quantitative probe for free volume in polymeric materials [66-67]. In a PALS experiment, high energy positrons are injected from a radiation source into a polymer sample. The positrons thermalize via collisions with atoms and either annihilate or form a hydrogen-like pair with a secondary electron created via collision-induced ionization. In polymers, the more stable pair system, called an ortho-positronium (o-Ps), tends to localize in regions of low density, i.e. holes. Annihilation of such localized o-Ps occurs via a pickoff mechanism in which the o-Ps positron annihilates with an electron of the medium with an opposite spin. Quantitative comparisons have been established between the characteristic parameters, obtained via

PALS, viz. the intensity, I_3, and lifetime, τ_3, of the o-Ps annihilation component, and the fractional free volume, f_v, of amorphous polymers, as computed by statistical mechanical theory [68-69]. The o-Ps intensity, I_3, is typically regarded as a measure of the number density of the free volume holes. The o-Ps lifetime, τ_3, can be related to a spherical hole radius, R, via the Tao-Eldrup equation, which is based on quantum mechanical and empirical arguments [70-71] as follows:

$$\tau_3 = 0.5\ (ns)\left[1 - \frac{R}{R_0} + \frac{1}{2\pi} sin\left(\frac{2\pi R}{R_0}\right)\right]^{-1} \quad (2.4)$$

where R is the hole radius in Å. R_0 equals $R + \Delta R$ where ΔR is a fitted empirical electron layer thickness of 1.66 Å. From R, the average hole free volume $v_h = (4\pi/3)R^3$ may be calculated. It follows that f_v is proportional to the product $I_3 v_h$.

As mineral silicate layers are too dense for o-Ps species to form, PALS is only sensitive to the HBP content of the HBP/clay nanocomposites. PALS experiments were used to assess, as a function of clay content, the average free volume hole size below and above the glass transition of the nanocomposites.

References

1] Jr., H. F. G.; Jr., J. R. W.; III, E. M. M. Extrusion-The Definitive Processing Guide and Handbook. 2005; William Andrew Inc.

2] Kausch HH, Tirrell M. Polymer Interdiffusion. Annu Rev Mater Sci 1989; 19: 341-377.

3] Nazarenko S, Dennison M, Schuman T, Stepanov EV, Hiltner A, Baer E. Creating Layers of Concentrated Inorganic Particles by Interdiffusion of Polyethylenes in Microlayers. J Appl Polym Sci 1999; 73: 2877-2885.

4] Dhinojwala A, Torkelson JM. A Reconsideration of the Measurement of Polymer Interdiffusion by Fluorescence Nonradiative Energy Transfer. Macromolecules 1994; 27: 4817-4824.

5] Dlubek, G, Bondarenko V, Pionteck J, Kilburn D, Pompe G, Taesler C, Redmann F, Petters K, Krause-Rehberg R, Alam MA. Studies of interdiffusion in polymer blends by PALS. Radiat Phys Chem 2003; 68: 369-373.

6] Yukioka S, Nagato K, Inoue. Ellipsometric studies on mutual diffusion and adhesion development at polymer-polymer interfaces. Polymer 1992; 33 (6): 1171-1176.

7] Fleischer G, Straube E. Pulsed field gradient NMR measurements and theoretical interpretation of the self-diffusion of polystyrene in solution. Polymer 1985; 26: 241-246.

8] Liao Y, Nakagawa A, Horiuchi S, Ougizawa T. Interdiffusion at Homopolymer/ Random Copolymer Interfaces Investigated by Energy-Filtering Transmission Electron Microscopy. Macromolecules 2007; 40: 7966-7972.

9] Jones R, Klein J, Donald A. Mutual diffusion in a miscible polymer blend. Nature 1986; 321: 161-162.

10] Kim SD, Klein A, Sperling LH. Review of Polystyrene Diffusion Studies in Latex Particles by Small-angle Neutron Scattering. Polym Adv Technol 2002; 13: 403-412.

11] Welp KA, Wool RP, Satija SK, Pispas S, Mays J. Dynamics of Polymer Interdiffusion: The Ripple Experiment. Macromolecules 1998; 31: 4915-4925.

12] Ewen B, Richter D, Farago B, Fetters L, Huang J, Maschke U. Neutron spin echo studies on segmental diffusion in polymer melts. Polym Mater Sci Eng 1992; 67: 211-212.

13] Shearmur TE, Clough AS, Drew DW, Grinten MGDv.d., Jones RAL. Interdiffusion of deuterated and protonated poly(methyl methacrylate). Polymer 1998; 39 (11): 2155-2159.

14] Russ T, Brenn R, Abel F, Boue F, Geoghegan M. Reptation and interdiffusion in polystyrene networks. Euro Phys J E 2001; 4: 419-433.

15] Calcagno L, Foti G. Interdiffusion in polystyrene crosslinked by keV ion irradiation. J Appl Phys 1991; 71 (7): 3216-3219.

16] Green PF, Palmstrom CJ, Mayer JW, Kramer EJ. Marker Displacement Measurements of Polymer-Polymer Interdiffusion. Macromolecules 1985; 18: 501-507.

17] Jablonski EL, Gorga RE, Narasimhan B. Interdiffusion and phase behavior at homopolymer/random copolymer interfaces. Polymer 2003; 44: 729-741.

18] Elklind H, Hjertberg T, Determination of Interdiffusion in Thin Polymer Films Using FTIR Reflection Absorption Spectroscopy. Macromolecules 1993; 26: 5844-5851.

19] Neuber R, Schneider HA, Concentration-way profiles and interdiffusion coefficients of contacting compatible polymers by scanning FT-IR microscopy. Polymer 2001; 42: 8085-8091.

20] Qiu H, Bousmina M. New technique allowing the quantification of diffusion at polymer/polymer interfaces using rheological analysis: Theoratical and experimental results. J Rheol 1999; 43 (3): 551-568.

21] Zhao R, Macosko CW. Polymer-Polymer Mutual Diffusion via Rheology of Coextruded Multilayers. AIChE J 2007; 53 (4): 978-985.

22] Koizumi S, Hasegawa H, Hashimoto T. Mutual diffusion of block polymer and homopolymer. Visualization using microdomain as a probe. Macromolecules 1990; 23: 2955-2962.

23] Mueller C, Kerns J, Ebeling T, Nazarenko S, Hiltner A, Baer E. Microlayer Coextrusion: Processing and Applications. Polymer Process Engineering 1997.

24] Chen P-Y, Lin Y-S, Yang W, Lopez MI, Li J, Olevsky EA, Meyers MA. Predation versus protection: Fish teeth and scales evaluated by nanoindentation. J Mater Res 2012; 27 (1): 100-112.

25] Wang RZ, Suo Z, Evans AG, Yao N, Aksay IA. Deformation mechanism in nacre. J Mater Res 2001; 16 (9): 2485-2493.

26] Kakisawa H, Sumitomo T. The toughening mechanism of nacre and structural materials inspired by nacre. Sci Technol Adv Mater 2011; 12: 64710.

27] Schuman T, Nazarenko S, Stepanov EV, Magonov SN, Hiltner A, Baer E. Solid state structure and melting behavior of interdiffused polyethylenes in microlayers. Polymer 1999; 40: 7373-7385.

28] Jarus D, Hiltner A, Baer E. Barrier properties of polypropylene/polyamide blends produced by microlayer coextrusion. Polymer 2002; 43: 2401-2408.

29] Eichhorn J. Proc. 28th Annual National Packaging Forum 1966; 4: 242.

30] Im J, Hiltner A, Baer E. Microlayer Composites. High Performance Polymers 1991: 175-198.

31] Nazarenko S, Hiltner A, Baer E. Polymer microlayer structures with anisotropic conductivity. J Mater Sci 1999; 34: 1461-1470.

32] Lai C-Y, Ponting MT, Baer E. Influence of interdiffusion on multilayered gradient refractive index (GRIN) lens materials. Polymer 2012; 53: 1393-1403.

33] Song H, Singer K, Lott J, Wu Y, Zhou J, Andrews J, Baer E, Hiltner A, Weder C. Continuous melt processing of all-polymer distributed feedback lasers. J Mater Chem 2009; 19: 7520-7524.

34] Jabbari E, Peppas NA. A model for interdiffusion at interfaces of polymers with dissimilar physical properties. Polymer 1995; 36 (3): 575-586.

35] Klein J. The Interdiffusion of Polymers. Science 1990; 250 (4981): 640-646.

36] Kramer EJ, Green P, Palmstrom CJ. Interdiffusion and marker movements in concentrated polymer-polymer diffusion couples. Polymer 1984; 25: 473-480.

37] Sillescu H. Relation of interdiffusion and tracer diffusion in polymer blends. Makromol Chem Rapid Commun 1987; 8: 393.

38] Pollock G, Nazarenko S, Hiltner A, Baer E. Interdiffusion in Microlayered Polymer Composites of Polycarbonate and a Copolyester. J Appl Polym Sci 1994; 52: 163-176.

39] Schuman T, Stepanov EV, Nazarenko S, Capaccio G, Hiltner A, Baer E. Interdiffusion of Linear and Branched Polyethylene in Microlayers Studied via Melting Behavior. Macromolecules 1998; 31: 4551-4561.

40] Nielsen LE. J Macromol Sci (Chem) 1967; A1 (5): 929.

41] Cussler EL, Hughes SE, III WJW, Aris R. Barrier Membranes. Journal of Membrane Sci 1988; 38: 161-174.

42] Fredrickson GH, Bicerano JJ. J Chem Phys 1999; 110 (4): 2181-2188.

43] Gusev AA, Lusti HR, Rational Design of Nanocomposites for Barrier Applications. Adv Mater 2001; 13 (21): 1641-1643.

44] Zheng BX, Song Y, Shangguan Y. Polymer 2006: 47.

45] Potts JR, Dreyer DR, Bielawski CW, Ruoff RS. Graphene-based polymer nanocomposites. Polymer 2011: 5-25.

46] Alexandre M, Dubois P. Polymer-layered silicate nanocomposites: preparation, properties, and uses of a new class of materials. Mater Sci Eng 2000; 28: 1.

47] Ray SS, Okamoto M. Polymer/layered silicate nanocomposites: a review from preparation to processing. Prog Polym Sci 2003; 28: 1539.

48] Tjong SC. Structural and mechanical properties of polymer nanocomposites. Mater Sci Eng 2006; 53: 73.

49] Wunderlich B. Reversible crystallization and the rigid–amorphous phase in semicrystalline macromolecules. Prog Polym Sci 2003; 28: 383.

50] Wunderlich B. Calorimetry of Nanophases of Macromolecules. Int J Thermophys 2007; 28: 958.

51] Lin J, Shenogin S, Nazarenko S. Oxygen Solubility and Specific Volume of Rigid Amorphous Fraction in Semicrystalline Poly(ethylene terephthalate). Polymer 2002; 43: 4733.

52] Olson BG, Lin J, Nazarenko S, Jamieson AM. Positron Annihilation Lifetime Spectroscopy of Poly(ethylene terephthalate): Contributions from Rigid and Mobile Amorphous Fractions. Macromolecules 2003; 36: 7618.

53] Righetti MC, Tombari E, Di Lorenzo ML. The Role of the Crystallization Temperature on the Nanophase Structure Evolution of Poly[(R)-3-hydroxybutyrate]. J Phys Chem B 2013; 117: 12303.

54] Di Lorenzo ML, Androsch R, and Stolte I. Tailoring the rigid amorphous fraction of isotactic polybutene-1 by ethylene chain defects. Polymer 2014; 55: 6132.

55] Hamonic F, Miri V, Saiter A, and Dargent E. Rigid amorphous fraction versus oriented amorphous fraction in uniaxially drawn polyesters. Eur Polym J 2014; 58: 233.

56] Beckingham BS, Ho V, and Segalman RA. Formation of a Rigid Amorphous Fraction in Poly(3-(2'-ethyl) hexylthiophene). ACS Macro Lett 2014; 3: 684.

57] Righetti MC, Laus M, and Di Lorenzo ML. Temperature dependence of the rigid amorphous fraction in poly(ethylene terephthalate). Eur Polym J 2014; 58: 60.

58] Righetti MC, Laus M, Di Lorenzo ML. Rigid amorphous fraction and melting behavior of poly(ethylene terephthalate). Colloid Polym Sci 2014; 292: 1365.

59] Tognana S and Salgueiro W. Influence of the rigid amorphous fraction and segregation during crystallization in PHB/DGEBA blends. Polym J 2015: 1.

60] Massa CA, Pizzanelli S, Bercu V, Pardi L, and Leporini D. Constrained and Heterogeneous Dynamics in the Mobile and the Rigid Ammorphous Fractions of Poly(dimethylsiloxane): A Multifrequency High-Field Electron Paramagnetic Resonance Study. Macromolecules 2014; 47, 6748.

61] Remy R, Wei S, Campos LM, and Mackay ME. Three-Phase Morphology of Semicrystalline Polymer Semiconductors: A Quantitative Analysis. ACS Macro Lett 2015; 4: 1051.

62] Sargsyan A, Tonoyan A, Davtyan S, Schick C. The amount of immobilized polymer in PMMA SiO2 nanocomposites determined from calorimetric data. Eur Polym J 2007; 43: 3113.

63] Corcione EC, Maffezzoli A. Glass transition in thermosetting clay-nanocomposite polyurethanes. Thermochim Acta 2009; 485: 43.

64] Wurm A, Ismail M, Kretzschmar B, Pospiech D, Schick C. Retarded Crystallization in Polyamide/Layered Silicates Nanocomposites Caused by an Immobilized Interphase. Macromolecules 2010; 43: 1480.

65] Fotiadou S, Chrissopoulou K, Frick B, Anastasiadis SH. Structure and Dynamics of Polymer Chains in Hydrophilic Nanocomposites. J Polym Sci, Part B: Polym Phys 2010; 48: 1658.

66] Pethrick RA. Positron annihilation—A probe for nanoscale voids and free volume? Prog Polym Sci 1997; 22: 1.

67] Jean YC, Mallon PE, Schrader DM (Eds). Principles and Applications of Positron and Positronium Chemistry. River Edge, NJ: World Scientific; 2003.

68] Higuchi H, Yu Z, Jamieson AM, Simha R, McGervey JD. Thermal history and temperature dependence of viscoelastic properties of polymer glasses: relation to free volume quantities. J Polym Sci Polym Phys 1995; 33(17): 2295.

69] Simha R, Somcynsky T. On the Statistical Thermodynamics of Spherical and Chain Molecule Fluids. Macromolecules 1969; 2: 342.

70] Eldrup M, Lightbody D, Sherwood NJ. The temperature dependence of positron lifetimes in solid pivalic acid. Chem Phys 1981; 63: 51.

71] Tao SJ. Positronium annihilation in molecular substances. J Chem Phys 1972; 56: 5499.

CHAPTER III - POLYETHYLENE-BASED NANOCOMPOSITES CONTAINING ORGANOCLAY: A NEW APPROACH TO ENHANCE GAS BARRIER VIA MULTILAYER COEXTRUSION AND INTERDIFFUSION

This chapter was co-authored with Jeremy J Decker, Donald R Paul, David A Schiraldi, Anne Hiltner, and Sergei Nazarenko

Abstract

Layer multiplying coextrusion was employed to produce films consisting of alternating layers of unfilled and particulate filled polymers, i.e., low density polyethylene (LDPE) and maleic anhydride grafted linear low density polyethylene (LLDPE-g-MA)/organoclay nanocomposites. Layer multilplying coextrusion was employed to produce gas barrier films consisting of alternating layers of unfilled and particulate filled polymers, i.e., low density polyethylene (LDPE) and maleic anhydride grafted linear low density polyethylene (LLDPE-g-MA)/organoclay nanocomposite. To further enhance gas barrier performance, the clay concentration within the nanocomposite layers was increased several fold through annealing of the multilayer film in the melt state. Residing in the melt state activated the interdiffusion between the polymers and due to a significant difference in the molecular mobility between the LDPE and LLDPE-g-MA chains led to a moving boundary effect which contracted the (LLDPE-g-MA)-rich nanocomposite layers and expanded the LDPE-rich layers. Analysis of the clay morphology within the nanocomposite layers demonstrated an increase in the clay particle lengths and aspect ratios, which was attributed to the growth of "skewed" aggregates during layer contraction and particle concentration. The melt induced clay concentration and increased clay particle dimensions caused a significant decrease in

oxygen permeability of the nanocomposite layers and reduced the overall permeability of the multilayered films. Morphology and transport behavior of the multilayered films were compared to a series of LLDPE-g-MA/clay bulk nanocomposites with varying clay content prepared by melt compounding in a twin screw extruder. Nielsen and Cussler models were used to describe the gas barrier data of the nanocomposite films. Although both models can be fit well to the experimental data, the Cussler model showed a better agreement with the morphological observations.

Introduction

Polyethylene (PE) is one of the least expensive plastics produced in high volume and is used in a variety of applications, in particular packaging films [1]. While high gas barrier is often an essential attribute of a packaging film, all kinds of polyethylenes unfortunately exhibit rather low gas barriers. There is therefore a need to modify PE in order to enhance the gas barrier. Incorporation of inorganic platelet shaped fillers to polymers has been extensively employed as a versatile approach to improve gas barrier. Well dispersed high aspect ratio platelet particles, especially when they are aligned in the direction parallel to the film surface, can result in a significant decrease of the gas permeability [2].

The use of high aspect ratio layered silicates as fillers in polymers has attracted considerable interest due to the ability to achieve exceptional property enhancements at low loading levels, in particular enhancements in gas barrier [3, 4, 5, 6, 7]. Sodium montmorillonite (Na-MMT) clay has in particular been widely used for blending with polymers as it is the most abundant naturally occurring nanoclay. The structure of Na-

MMT consists of stacks of crystalline mineral sheets (nanoplatelets) that are 1 nm thick and about 50-150 nm long. If these high aspect ratio nanoplatelets are highly delaminated and uniformly dispersed in the polymer matrix, even at low concentrations, a considerable reduction of the gas permeability is expected. Single clay layers, however, exhibit a tendency to aggregate and this process may strongly affect the gas barrier outcome as compared to the one anticipated when the clay is dispersed to the level of single nanoplatelets [8]. Thus, to relate the nanocomposite gas barrier to the clay morphology one needs to conduct a very thorough analysis of the clay aggregates.

Polyethylene is a nonpolar polymer and thus lacks favorable interactions with the polar surface of the silicate layers even when the clay surfaces are organically modified. The most commonly used method to overcome this hurdle is based on chemical modification of the PE structure by grafting with polar maleic anhydride (MA) moieties to make the hydrophobic polymer more compatible with the clay surfaces. Adding a small amount of MA-grafted PE as a compatibilizer upon melt compounding of unmodified polyolefin with clay typically results in nanocomposites with an intercalated morphology. Direct melt compounding of organoclay with MA-grafted PE can, however, produce nanocomposites with a highly delaminated morphology [9].

Theoretical predictions of gas diffusion in the composite media containing platelet fillers suggest that the characteristic distance between the particles will control barrier properties [10]. Two possible filler concentration regimes are characterized by very different diffusion behavior. Under dilute particle conditions, the disks are spaced at a distance much exceeding the disk radius *R* and their volume fraction is much less than one. Here the contributions of the disks to the effective diffusivity of the permeants are

nearly independent and are best described by a tortuosity model derived by Nielsen [11]. At semidilute concentrations, the volume fraction of the disks is still much less than one but they are spaced at distances comparable to or smaller than *R*. In this semidilute regime the physics of diffusion is dominated by the significant contribution of repeated multiple scatterings of penetrant molecules between the close pairs of disks, adding considerably to the decrease in the overall diffusivity of the composite [10]. These changes in diffusivity in the semidilute diffusion regime are best described by the models derived by Cussler [12, 13]. Therefore, it can be advantageous for barrier enhancement, while maintaining the same overall mineral content and even reducing it, to disperse particulates unevenly, for instance, by fabricating a layered structure where polymer layers containing particulates in concentrated regimes are alternated with unfilled layers of the same polymer. Previously we showed that multilayer coextrusion processing can be successfully employed to fabricate films with alternating layers of filled and unfilled polymers [14, 15, 16].

The basic multilayer coextrusion system consists of two single screw extruders equipped with melt pumps, a coextrusion feed block, a series of layer multiplier elements, and a film die (film spreader). Metering pumps control the polymer melt streams which are combined in the feedblock as two parallel layers. From the feedblock the layers flow through a series of layer multiplying elements, with each multiplier element doubling the number of layers by first slicing the layers vertically, then spreading them horizontally, and finally recombining. The multilayer coextrusion process used in this study enables the fabrication of layered polymer films with tens, hundreds, and even thousands of alternating layers with individual layer thicknesses that can vary from hundreds of

microns to tens of nanometers [17-19]. Due to the stringent flow conditions, multilayering generally promotes particle orientation but highly concentrated regimes are difficult to achieve as they result in a considerable elevation in viscosity making the composite melts impossible to coextrude. It has been previously demonstrated that interdiffusion of a polymer pair in a multilayer can be employed to increase the concentration of inorganic particles in one of the component layers [20]. The physics of this phenomenon is described below.

Polymer-polymer interdiffusion or polymer-polymer mutual diffusion describes the process of polymer chain transport, usually in both directions, across an interface that is driven by a compositional gradient [21-22]. Early studies on interdiffusion analyzed polymer couples (bilayers) with only one interface. Kramer and Green et al. were the first to demonstrate that interdiffusion between two polymers, i.e., polystyrenes exhibiting very different molecular weights, can lead to a moving boundary (interface) phenomenon similar to that known in metallurgy as the Kirkendall effect [23]. This effect can be observed when the individual diffusion coefficients in the interdiffusing couple are very different. The polymer-polymer interface moves toward the polymer exhibiting a lower molecular weight (faster diffusing component). This movement has been attributed to the conservation of melt density. To conserve density, the voids created due to an imbalance in mass transport across the interface have to collapse causing the boundary to move [24-25].

More recently, multilayers have been employed for interdiffusion studies [26-29]. They display two major advantages. A larger contact area and a greater number of interfaces can amplify the effect so that more common characterization techniques can be

used to monitor the progression of interdiffusion. Also, because individual multilayer layers can be made relatively thin, the entire process of interdiffusion from start until finish (complete compositional homogenization) can be observed within a reasonable experimental time scale. A study conducted by our group in the past has demonstrated a very strong moving boundary effect in HDPE/LLDPE polyethylene multilayers. Upon annealing in the melt state, the layers containing faster interdiffusing chains (LLDPE) contracted and the layers containing slower interdiffusing chains (HDPE) subsequently expanded [30-31]. In the study conducted later on LDPE/LLDPE multilayers, micro particulates such as talc and nickel were added to the LLDPE polymer - faster interdiffusing component. The LLDPE layers contracted by more than fourfold resulting in a more than a fourfold increase in particulate concentration [20]. In this study that follows, organically modified Na-MMT nanoclay has been incorporated in the LLDPE-g-MA layers of a LLDPE-g-MA/LDPE multilayer. Interdiffusion and particle concentration upon annealing of this multilayer are studied with a particular emphasis on morphological and gas barrier changes.

Experimental

Materials

The organoclay, Cloisite®20A, dimethyl-bis(hydrogenate-tallow) ammonium montmorillonite, was purchased from Southern Clay Products. It is prepared by a cation exchange reaction between sodium montmorillonite (Na-MMT) and a two-tailed quaternary ammonium surfactant, i.e., dimethyl-bis(hydrogenated-tallow) ammonium chloride. According to the company specifications, the organic content of this clay is

38% (wt/wt) with a WAXS d-spacing of 25.1 Å. This organoclay was selected based upon previous studies showing excellent dispersion of Cloisite®20A with maleated polyethylene and because its two alkyl tail surfactant exhibits equitable thermal stability at 200°C [9, 32].

Much of the discussion will focus upon the inorganic portion of the organoclay, which will be designated as MMT, and any references to the MMT fraction in a polymer must be understood to only apply to the inorganic portion. The mineral weight fraction, w_m, was calculated as follows, $w_m = \gamma \cdot m_{oc}/m_{com}$, where m_{oc} is the weight of organoclay in the composite, m_{com} is the weight of the composite (organoclay + polymer), and γ is the mineral weight fraction within the organoclay itself (0.62 in this case). The volume fraction, ϕ_m, was calculated from the corresponding weight fraction as follows, $\phi_m = w_m (\rho_{com}/\rho_m)$, where ρ_{com} is the composite density and ρ_m is the mineral clay layer density, 2.86 g/cm^3. The composite density, ρ_{com}, was calculated from the corresponding weight fraction and the densities of the polymer and mineral layers assuming the two phase scheme. The organic matrix density was assumed to be equal to the original polymer density.

The maleic anhydride grafted linear low density polyethylene (LLDPE-g-MA), Fusabond® E MX110D, subsequently designated as PEMA110, was donated by DuPont. It was chosen in this study for its high melt flow index (MFI), 16.8 g/10min at 200°C and 2.16 kg. The PEMA110 was used to prepare polymer/clay nanocomposites for multilayering. After dispersing 5% (wt/wt) of nanoclay in PEMA110, the MFI was reduced to be very suitable for the multilayer coextrusion, 4.9 g/10min. The second LLDPE-g-MA system, Fusabond® E MB528D, also donated by DuPont and designated

here as PEMA528, was employed in this study as a model for comparative study. It has a much smaller MFI, 4.2 g/10 min, and a higher capacity to disperse larger loadings of the nanoclay. Based on our ^{1}H NMR analysis, the MA graft levels of PEMA 110 and PEMA 528 were 1.3 wt% and 1.0 wt% respectively. These levels of MA grafting are comparable with that reported elsewhere for a similar resin [9].

The low density polyethylene, Huntsman PE2030, designated here as LDPE, was purchased from PolyOne. This polymer was used to prepare a multilayer film. The MFI for this LDPE, 5.2 g/10min, matches well with the MFI for the PEMA110 nanocomposite containing 5% (wt/wt) of nanoclay. Note, matching the melt viscosities for the polymers comprising the alternating layers is critical for successful coextrusion of multilayers.

Melt processing

The nanoclay and the LLDPE-g-MA polymers were dried for a minimum of 24 hours in a vacuum oven at 80°C and then cooled to room temperature under vacuum prior to melt processing. Nanocomposites were melt compounded in a Prism TSE 16TC twin screw extruder using a barrel temperature of 200°C, a screw speed of 70 rpm, and maximal feed rate to generate kilogram quantities of pellets. For all nanocomposites generated, the LLDPE-g-MA and the nanoclay were hand mixed and introduced into the extruder by a single hopper which was blanketed in nitrogen gas to prevent water uptake. The extrudate was cooled in an ice water bath, pelletized, and dried at 80°C under vacuum for 2 hours. The dried pellets were reintroduced into the hopper and extruded again under the same conditions. This process was carried out four times for each nanocomposite generated, as it was found to optimize clay dispersion. After final drying,

the nanocomposite pellets were stored over desiccant. Film specimens were generated by compression molding at 200°C and 3000 psi on a non-stick surface in a 1 mm thick mold for oxygen transport, WAXS, and TEM analysis. MMT content of the samples was confirmed by placing pre-dried nanocomposite films or pellets in a furnace at 900°C for one hour and weighing the remaining MMT ash, correcting for the loss of structural water [33].

Multilayer films composed of 65 alternating layers of LDPE and PEMA110 nanocomposite with 5% wt/wt (1.0% vol/vol) of MMT were coextruded at a feed ratio 1:1 using the multilayer coextrusion system described previously [14, 34]. A sacrificial polystyrene layer was extruded on the outer surfaces of the multilayered films to prevent deformation of the external polyethylene layers from internal stresses during cooling, and was thereafter removed. After removal of both sacrificial layers, the final multilayer films possessed an average thickness of about 340 microns. The films were stored over desiccant. Layer volume composition was confirmed by measuring MMT ash and via direct observation of the layers by OM and TEM.

The multilayer films composed of LDPE and PEMA110/Cloisite®20A nanocomposite were annealed at 200°C under nitrogen atmosphere in a melt press for various times. Film specimens were annealed on non-stick surfaces and confined in a mold specifically fabricated to match the film thickness. Films were carefully cut to fit these molds, in order to prevent distortion of the film dimensions during annealing. The pressure applied was under 50 psi since confinement, not compression, was the objective. A constant nitrogen flow was provided around the melt press platens to reduce oxidative

degradation. After annealing, the films were quenched in ice water, dried, and stored over desiccant.

To take into account the effect of interdiffusion in a multilayered system on the gas barrier of the polymer components, a series of compositional blends of the LLDPE-g-MA (PEMA110) and LDPE (PE2030) were melt processed from pure polymer pellets in a Prism TSE 16TC twin screw extruder at 200°C and a screw speed of 70 rpm. The polymers were dried for a minimum of 24 hours under vacuum at 80°C prior to melt blending. The polymer blend extrudates were cooled in ice water, pelletized, and dried under vacuum at 80°C with the process repeated four times to achieve maximum mixing and match the thermal history of the nanocomposites. Film specimens were produced by compression molding at 200°C and 3000 psi on a non-stick PTFE coated surface in a 1 mm thick mold for oxygen transport measurements.

Characterization

^{1}H NMR was used to determine the MA-grafting levels of the LLDPE-g-MA resins used in this study. The solvent was deuterated tetrachloroethane (TCE). All spectra were acquired on a Varian UNITYINOVA spectrometer operating at a frequency of 499.8 MHz and using a standard 5 mm two-channel probe. A 90° flip angle of 19.75 μs and an acquisition time of 1.9 s were used. The number of co-added scans was 192, with a delay of 19.6 s implemented between transients. A Lorentzian filter of 0.53 Hz was applied prior to application of the Fourier transform. Peak shifts were referenced to the residual proton signal for the deuterated TCE solvent (6.0 ppm). Peak assignments for the

maleic anhydride sites were based on previously reported values [35-36]. Weight percentages were calculated using proton integral values.

One dimensional X-ray diffraction spectra were collected on a Rigaku Ultima III diffractometer (Cu Kα radiation, λ = 1.542 Å) at room temperature using Bragg-Brentano parafocusing geometry (reflection mode XRD) on the sample films.

Melt flow indices (MFI) were determined according to ASTM D1238 using a Dynisco melt flow indexer at 200°C with applied weights of 2.16 kg and 5.0 kg.

Oxygen barrier of the nanocomposite films and controls were measured at 25°C, 0% RH, and 1 atm partial oxygen pressure difference using a commercially manufactured diffusion apparatus, OX-TRAN® 2/21 ML (MOCON). This instrument employs a continuous-flow method (ASTM D3985-81 and ASTM F1249-01) with nitrogen as the carrier gas to measure oxygen flux, *J(t)*, through polymeric films. The film specimens were carefully conditioned in the instrument, as described previously [16]. The permeability coefficient, *P*, was calculated directly from the steady-state flux, J_∞, value as $P = J_\infty l/\Delta p$, where *l* is the film thickness and Δp is the oxygen partial pressure difference across the film. We use throughout this article the following standard permeability units, $cc_{gas}(STP)\cdot cm)/(m^2\cdot day\cdot atm)$, designated here as SPU.

For the optical microscopy (OM) analysis of the multilayered films, 5 μm thick sections were microtomed perpendicular to the film surface using a glass knife. Phase contrast images were captured on film and the layer thicknesses were determined by image analysis utilizing Digimizer Version 4.2.4.0. Changes in layer thicknesses of the annealed multilayered samples were quantified utilizing image analysis of the OM data.

For transmission electron microscopy (TEM), 90 nm thick sections were cut at T = -100°C in the direction perpendicular to the film surface using a Leica cryo-ultramicrotome FC6 and a diamond knife, where they were deposited on a copper grid. The sections were imaged using a Zeiss 109T TEM operated at an accelerating voltage of 80 kV under bright field conditions. Since the MMT layers have a higher electron density than the surrounding polymer matrix, they appear darker in the images. Image analysis of TEM micrographs was used to quantify clay particle dimensions. The micrographs were analyzed at 20K magnification which allowed for sufficient resolution to observe individual clay nanoplatelets as well as providing a suitable area from which to extract a large population sampling. Clearly focused and well stigmated micrographs were utilized, since image clarity and resolution were critical to this analysis, especially for individual MMT nanoplatelets, due to their nanoscale dimensions proving difficult to discriminate from the polymer matrix. Within the designated area, each and every discernible clay layer was traced using Adobe Photoshop. These tracings were saved separately in bitmap format and imported into the image analysis program, Digimizer 4.2.4.0, where the clay particle characteristic dimensions were measured. Particle lengths were determined as the end-to-end distance. Particle thicknesses were determined by dividing the particles into six equidistant sections, where five thickness measurements were taken at these divisions to average the particle thickness. For clay particle sections consisting of a single MMT layer, the thickness could not accurately be measured due to resolution limitations and were assigned a thickness of 1 nm corresponding to the thickness of an individual MMT sheet. To achieve statistical validity in this analysis, at least 400 particles were measured for length and thickness per sample.

Results and Discussion

Clay Morphology in Bulk Nanocomposites

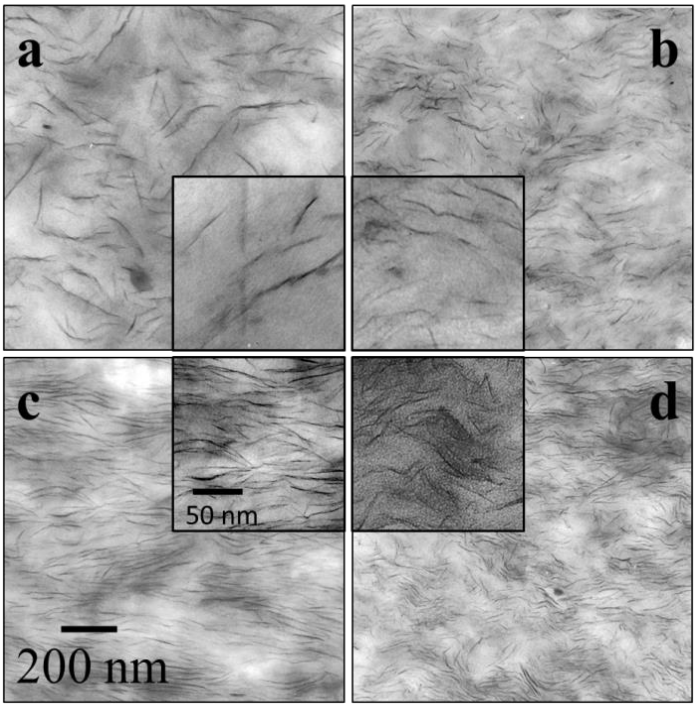

Figure 3.1 Representative TEM micrographs of clay morphologies in bulk nanocomposite films with the following MMT volume fractions (v/v): (a) 1.0%; (b) 2.1%; (c) 3.2%; (d) 4.4%

Representative TEM micrographs of PEMA528/Cloisite®20A compression molded films (microtomed cross-sections) are shown in Figure 3.1. The inserts are images taken at higher magnification. All of the nanocomposites exhibited a highly delaminated morphology. One can see in the micrographs single nanoplatelets but more often tiny clay particles (aggregates) consisting of several (2-4) nanoplatelets. In many instances the individual silicate platelets forming these small aggregates were skewed in a staircase fashion forming the striations that are longer than the individual nanoplatelets. Figure 3.2a displays a schematic of one of these clay particles consisting of several

skewed platelets and Figure 3.2b shows a real example revealed by TEM at high magnification of the PEMA528 nanocomposite with a MMT content of 1.0% (vol/vol).

Skewing of nanoplatelets due to shear stresses upon melt mixing has been discussed in detail elsewhere [33, 37]. One of the goals of this project is to appraise the clay particles dimensions and relate this information to the nanocomposite gas barrier performance. Of note, skewed aggregates were a predominant morphological feature in every PE based nanocomposite system we studied including the multilayer film. A very high resolution image of the nanocomposite layer in the multilayer film shown as Figure 3.1s in the Supplementary Information part helps the reader to zoom in at a scale that allows one to see the individual clay layers.

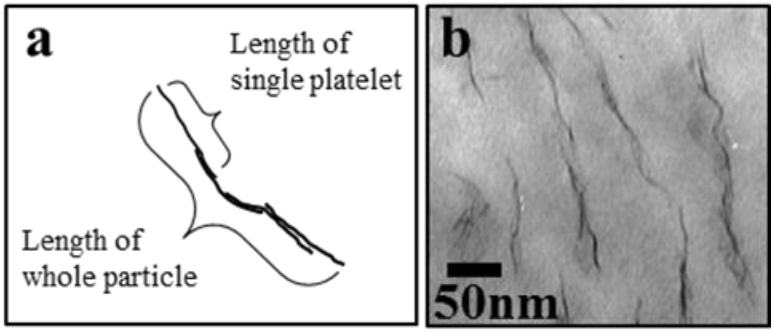

Figure 3.2 Skewed agglomerate consisting of several single clay platelets (a) schematic; (b) as revealed by TEM at higher magnification in a bulk nanocomposite with 1.0 % vol/vol MMT

With increasing MMT content, a decrease in clay particle length ($2R$) was noticeable while the particle thickness seemed to vary insignificantly. To quantitatively characterize the particle dimensions a series of statistical histograms were generated for the clay particle half-length (R_i), thickness (a), and aspect ratio (α). The histograms are shown in Figure 3.3 while the corresponding number average quantities with standard

deviations are reported in Table 3.1. The average half-length, $\overline{R}$, gradually decreased with increasing MMT content, approximately by a factor of two, from 46 to 24 nm, and the R_i distribution narrowed with the right side of the distribution noticeably shortened. The average thickness, $\overline{a}$, as well as the distribution remained unchanged, therefore the average individual particle aspect ratio, $\overline{\alpha}$, decreased along with the particle length, i.e., from 29 to 14, and the distribution became more narrow.

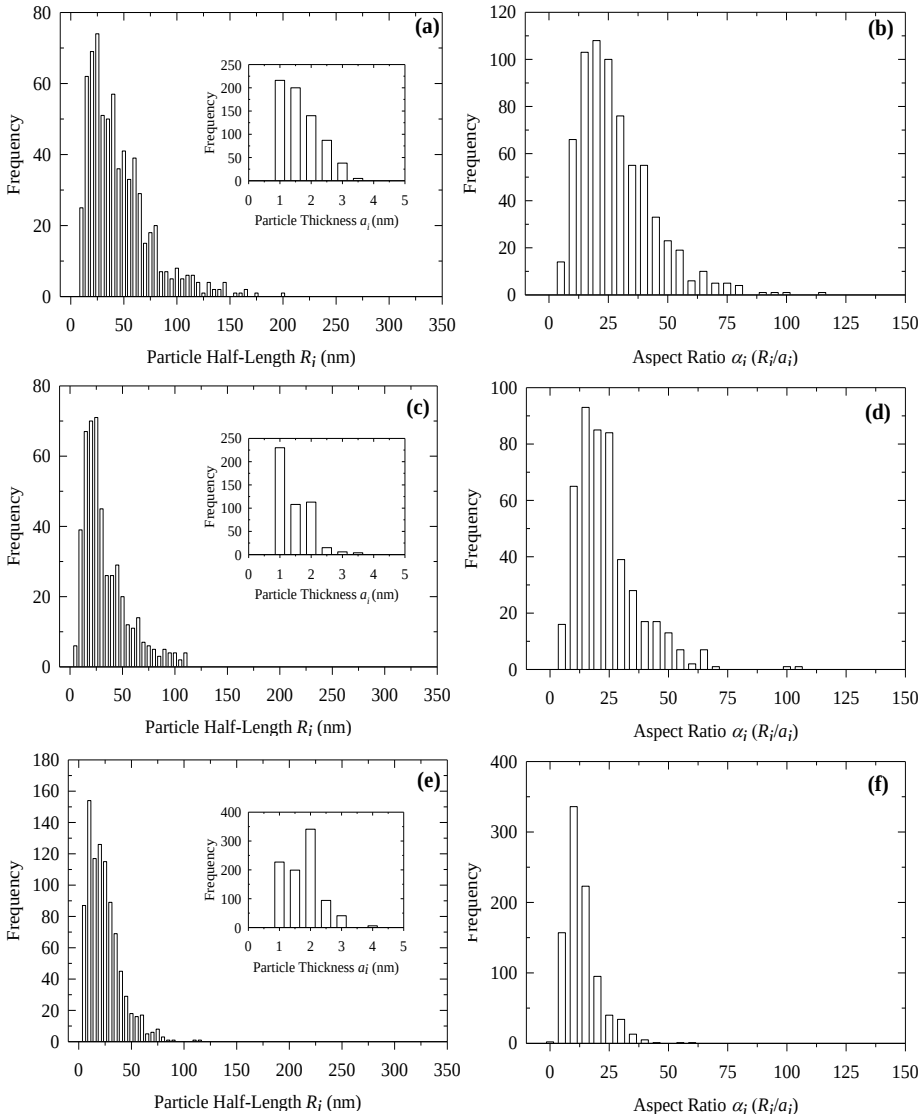

Figure 3.3 Histograms of nanoclay particle dimensions in PEMA528 nanocomposites. Frequency plots are shown for particle half-lengths, R_i, thicknesses, a_i (inserts), and aspect ratios, α_i. Plots arranged according to the mineral volume fractions as follows: (a,b) 1.0 %; (c,d) 2.1 %; (e,f) 4.4%

Table 3.1 TEM image analysis of clay particle dimensions in PEMA528/Cloisite®20A nanocomposites

MMT content (ϕ, vol/vol)	Total number of particles measured	Particle half-length ($\bar{R}$, nm)	Particle thickness ($\bar{a}$, nm)	Aspect ratio ($\bar{\alpha}$)
0.010	686	46 ± 30	1.7 ± 0.7	29 ± 16
0.021	476	33 ± 22	1.4 ± 0.5	24 ± 14
0.032	975	37 ± 27	1.8 ± 0.6	21 ± 13
0.043	908	24 ± 16	1.7 ± 0.6	14 ± 7

The decrease in particle aspect ratio with increasing clay content was consistent with previous findings and attributed mainly to the increase of the nanocomposite melt viscosity [38-39]. It has been demonstrated in polymer clay nanocomposites in general and in maleated polyolefin based systems, in particular, that as the content of nanoclay increases the melt viscosity of the nanocomposite also increases [38, 40]. Increased melt viscosity led to higher shear stresses applied to the clay particles. Under these more vigorous mixing conditions individual silicate nanoplatelets were peeled off more efficiently and as the number of single layers per skewed aggregate was reduced the particles appeared shorter [33]. With the PEMA528 based systems employed in this study, the MFI of the nanocomposites decreased dramatically with clay content, i.e., from 10.8 g/10min for the pure PEMA528, to 2.3 g/10min at 0.010 vol/vol MMT, to 0.3 g/10min at 0.021 vol/vol MMT, with an applied weight of 5.0 kg at 200°C, indicating

large increases in viscosity. At higher clay contents, the viscosity was too high to measure the MFI at this temperature.

The clay particles were preferentially oriented in the plane parallel to the film surface. The particle orientation somewhat improved with the addition of more MMT. The reason for this behavior is not exactly clear. One plausible argument is that it could be due to the increased mechanical coupling between the particles with decreasing the characteristic distance between them leading to more cooperative orientation behavior.

WAXS and TEM are complementary experimental approaches used to access the clay layer dispersion state in the nanocomposites. WAXS scans of the bulk nanocomposite samples are shown as Figure 3.2s in the Supplementary Information part. For comparative purposes, virgin PEMA528 and dry nanoclay are also included in the figure. The lack of any clear basal reflections in the PEMA528 nanocomposites were in agreement with the highly delaminated individual clay layers and the incoherently stacked skewed aggregates observed by TEM.

Layer Structure and Clay Morphology in Nanocomposite Multilayers

Optical micrographs of the multilayer films (cross-sections) are shown in Figure 3.4 for films that were held in the melt at 200°C for various times and the as-made (un-annealed) films. A continuous and rather uniform microlayer structure can be clearly observed. In the un-annealed multilayer the nanocomposite and LDPE layer widths were 5.25 ± 1.42 μm and 5.03 ± 1.50 μm respectively. In the OM images the nanocomposite layers appear darker than the LDPE layers. We are not exactly sure about the nature of this optical contrast; however, several factors may be at issue such as the alternating layer

height difference from microtoming, the crystalline morphology variance, and the refractive index dissimilarity caused by MMT. Clay nanoparticles cannot be seen directly with the optical microscope. A 3-D schematic of the multilayer films before and after annealing in the melt is also included in Figure 3.4.

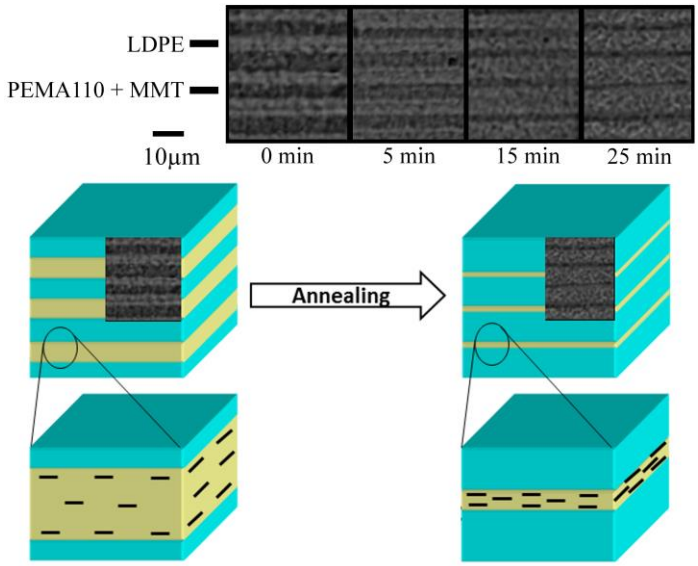

Figure 3.4 Optical Micrographs of the multilayered films after annealing at 200°C for the time indicated and a schematic of the multilayer nanocomposite before and after annealing/ particle concentration (OM inserts)

Upon annealing, the nanocomposite layers rapidly contracted and the LDPE- rich layers rapidly expanded, indicating that the PEMA110 chains had diffused into the LDPE layers much faster than the LDPE chains in the reverse direction. Slower dynamics of the LDPE was expected because the LDPE chains contain long branches. These long branches can form additional entanglements. In contrast, the LLDPE chains diffuse faster because they contain short branches which do not form these additional entanglements.

For a more quantitative analysis of the moving boundary phenomenon, the average layer widths determined by OM are plotted in Figure 3.5 versus the annealing

time root square ($t^{1/2}$). The layer thickness data are also reported in Table 3.2. The kinetics of the moving boundary effect in the multilayer was fairly rapid. Already after 25 minutes at 200°C the nanocomposite layers contracted roughly by a factor of 4 while the LDPE layers expanded by a factor of 2. At longer annealing times the films visibly degraded and were not further explored. The sum of the LDPE and the nanocomposite layer widths remained unchanged during the annealing process. The layer widths changed linearly with $t^{1/2}$. The $t^{1/2}$ dependence of a marker (boundary) movement in a polymer-polymer diffusion couple was predicted and experimentally confirmed in the past by Kramer et al. [24].

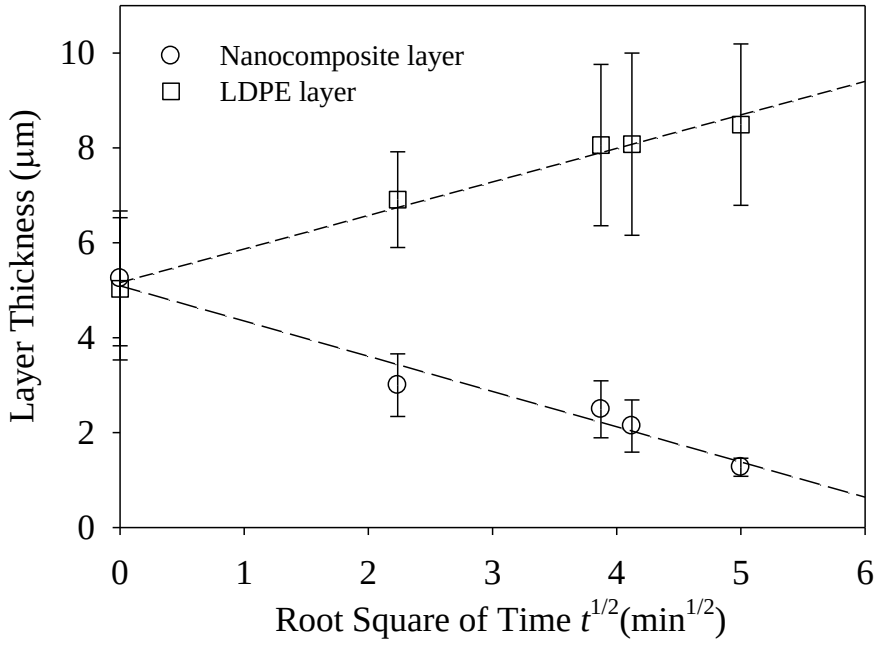

Figure 3.5 Average layer thicknesses of the multilayered film plotted as a function of the root square of annealing time

The moving boundary effect in the PEMA110-nanocomposite/LDPE multilayer caused the filled layers to contract and to concentrate the nanoclay. Since the clay

remained within the nanocomposite layers, the MMT volume fraction directly correlated with the narrowing of these layers. Therefore, the MMT average volume fraction in the nanocomposite layers upon annealing can be readily calculated. The data are reported in Table 3.2. The volume fraction of MMT in the nanocomposite layers varied from 1.0 % (v/v) in the as-made (un-annealed) multilayer to 4.3% (v/v) in the multilayer annealed for 25 minutes at 200°C.

Table 3.2 Nanocomposite and LDPE layer thicknesses for un-annealed and annealed (for various times at 200°C) multilayers. MMT volume content in the nanocomposite layers was calculated using the layer thickness information.

Annealing time (t, min)	Nanocomposite layer Thickness ($L_{f\text{-}l}$, μm)	LDPE-rich layer thickness (L_{LDPE}, μm)	Nanocomposite layer MMT content (ϕ, v/v)
0	5.3 ± 1.4	5.0 ± 1.5	0.010
5	3.0 ± 0.7	6.9 ± 1.0	0.018
15	2.5 ± 0.6	8.1 ± 1.7	0.022
17	2.1 ± 0.6	8.1 ± 1.9	0.025
25	1.3 ± 0.2	8.5 ± 1.7	0.043

One might anticipate that high aspect ratio clay particles would obstruct transport of the polymer chains during interdiffusion by increasing the length of the diffusion path, an effect that is expected to increase with clay particle concentration. However, the linear trends of the layer thickness with $t^{1/2}$ showed no changes in slope suggesting that the polymer chain reptation process apparently was not impeded by the clay particles, at least within the annealing time scale and mineral composition range studied.

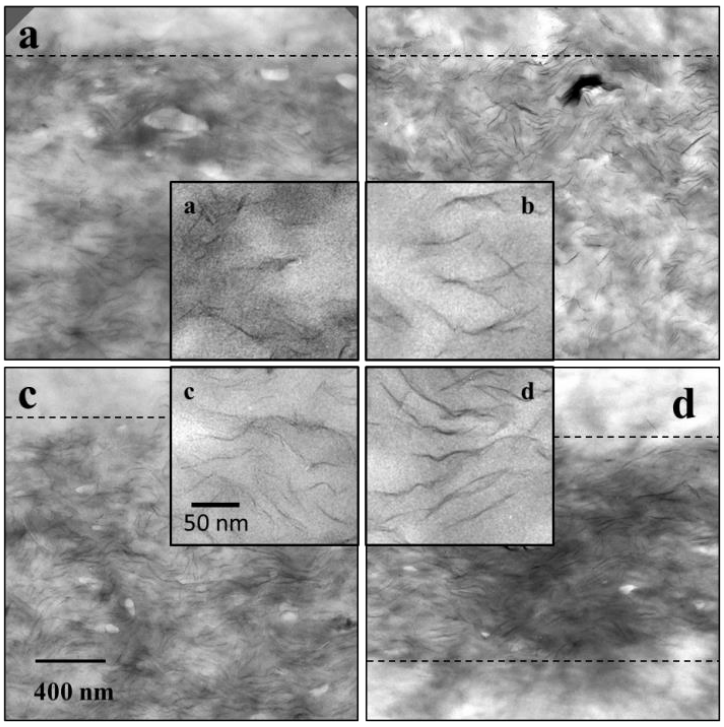

Figure 3.6 TEM micrographs of nanocomposite layers in the as-made multilayer (a) and after annealing at 200°C for 5 min (b); 15 min (c); and 25 min (d). Dotted lines indicate approximate layer boundaries. Inserts exhibit TEM micrographs at larger magnification.

Figure 3.6 displays TEM micrographs of nanocomposite layers in un-annealed and annealed at 200°C multilayers. To help the reader, the dotted lines indicate approximate layer boundaries when they appear in the field of view. The inserts show fragments of the TEM micrographs taken at higher magnification. The nanoclay seemed to be distributed uniformly within the layers in the as-made and annealed multilayer samples. The nanocomposite layers, similarly to the bulk nanocomposites presented in the previous section, exhibited a similar delaminated morphology in which the individual silicate nanoplatelets were skewed forming longer than individual platelet clay particles. Geometric constraints imposed by layer multiplying normally leads to extensive orientation of platelet microparticles, such as talc or metal flakes, in the plane of the layers [15, 20]. In the nanocomposite multilayers studied in this work, clay particle

orientation along the extrusion direction was also observed but certainly it was not as pronounced as in the case of previously studied multilayers containing microparticles. It is not exactly clear what the reason for this behavior is, but it could be due to the fact that the characteristic length of the clay particles is considerably smaller than the nanocomposite layer thickness. Because the nanoparticles are not as constricted upon coextrusion as previously employed microparticles, the nanoplatelets orientation appeared somewhat more prominent closer to the layer interfaces and certainly improved considerably after the nanocomposite layers narrowed sizably at longer annealing times. After longer annealing times, the clay particles in the nanocomposite layers also appeared longer. Interdiffusion and nanocomposite layer contraction apparently allowed for the growth of skewed aggregates as the nanoplatelets and clay particles impinged upon one another. This behavior is in contrast to that we earlier described for the bulk nanocomposites prepared by melt mixing in a twin screw extruder. A pictorial description of the clay particle evolution upon annealing and contraction of the nanocomposite layers in a multilayer is displayed in Figure 3.7.

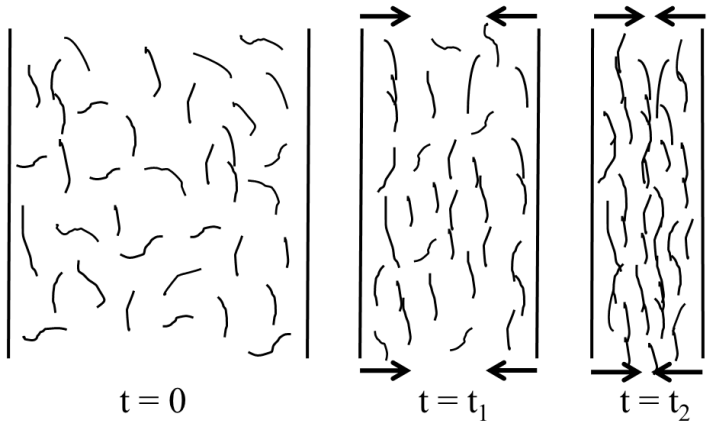

Figure 3.7 Pictorial model illustrating the evolution of skewed aggregates upon annealing and contraction of the nanocomposite layers in the multilayer

For a more quantitative description, a statistical analysis of the clay particle dimensions in the nanocomposite layers upon contraction was conducted in a manner similar to that described for the bulk nanocomposite controls. The histograms are shown in Figure 3.8 while the corresponding number average quantities with standard deviations are reported in Table 3.3. As one can see from the histograms, the average particle half-length, $\bar{R}$, gradually increased with annealing time from about 36 to 87 nm. Particularly noticeable in the histograms is a broadening of the distribution with the time of annealing toward longer particles. The average particle thickness, $\bar{a}$, practically did not change, nor did the distribution, hence the average aspect ratio, $\bar{\alpha}$, also increased from 30 to 55 with the distribution broadened towards larger aspect ratios.

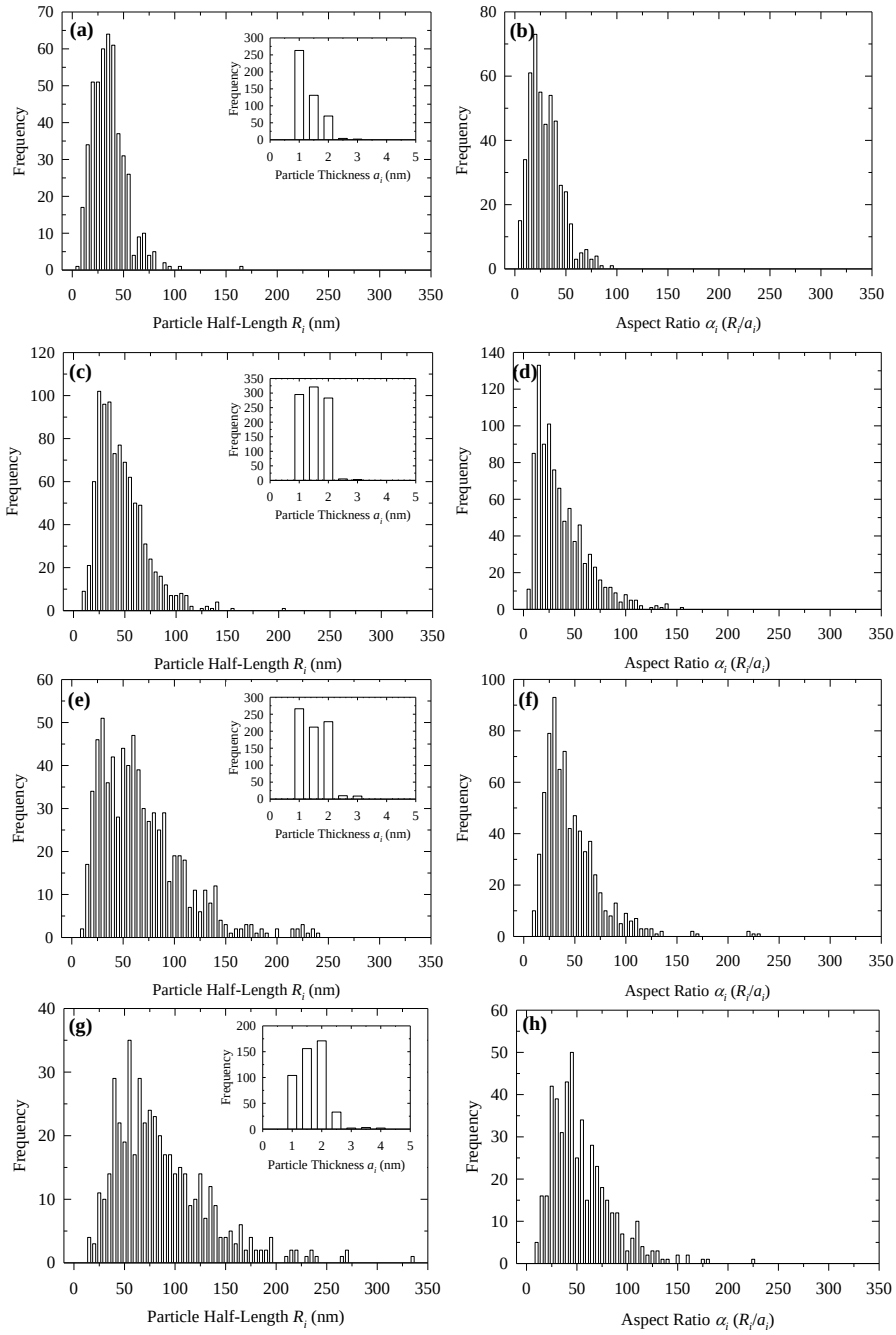

Figure 3.8 Histograms of nanoclay particle dimensions in the nanocomposite layers of the as-made and annealed at 200°C multilayer. Frequency plots are shown for particle half-lengths, R_i, thicknesses, a_i (inserts), and aspect ratios, α_i. Plots are arranged according to the calculated mineral volume fraction of the nanolayers in the multilayer (annealing time is also shown in brackets) as follows: (a,b) 1.0% (0 min); (c,d) 1.8% (5 min); (e,f) 2.2% (15 min); (g,h) 4.3% (25 min)

Table 3.3 TEM image analysis of clay particle dimensions in nanocomposite layers of un-annealed and annealed multilayer

Annealing time (t, min)	Nanocomposite layer MMT content (ϕ, v/v)	Total number of particle measured	Particle half-length ($\bar{R}$, nm)	Particle thickness ($\bar{a}$, nm)	Aspect ratio ($\bar{\alpha}$)
0	0.010	470	36 ± 17	1.3 ± 0.5	30 ± 16
5	0.018	907	47 ± 23	1.5 ± 0.5	37 ± 25
15	0.022	725	68 ± 41	1.5 ± 0.5	47 ± 28
17	0.025	829	73 ± 47	1.5 ± 0.5	53 ± 34
25	0.043	471	87 ± 47	1.7 ± 0.5	55 ± 30

In addition to TEM, un-annealed and annealed multilayers were also probed by WAXS to see if the coextrusion process or annealing produced any ordered intercalated clay morphology. The diffractograms of the PEMA110/ nanoclay clay control with 1.0% (v/v) of mineral phase and three diffractograms of un-annealed multilayer and a multilayer annealed at 200°C for 17 and 25 minutes are shown as Figure 3.3s in the Supplementary Information part. There were no observable changes in the XRD scans that would have indicated the clay layers had reagreggated into ordered tactoid structures. The clay particles did not possess the long range stacking order necessary for coherent basal reflections to arise.

Oxygen Permeability of LDPE/LLDPE-g-MA blends

The dependence of oxygen permeability for LDPE (PE2030)/LLDPE-g-MA (PEMA110) blends on volume fraction of PEMA110 is shown in Figure 3.9. We found the trend to be perfectly linear ($r^2 = 0.996$) and this we believe indicates that the blends

are miscible. Immiscible blends would undergo phase inversion and display a sigmoidal permeability trend with composition [41]. Miscibility in the melt of maleated and pure polyolefin blend systems has been observed before at maleic anhydride concentrations low enough not to cause phase separation due to unfavorable chain interaction [42].

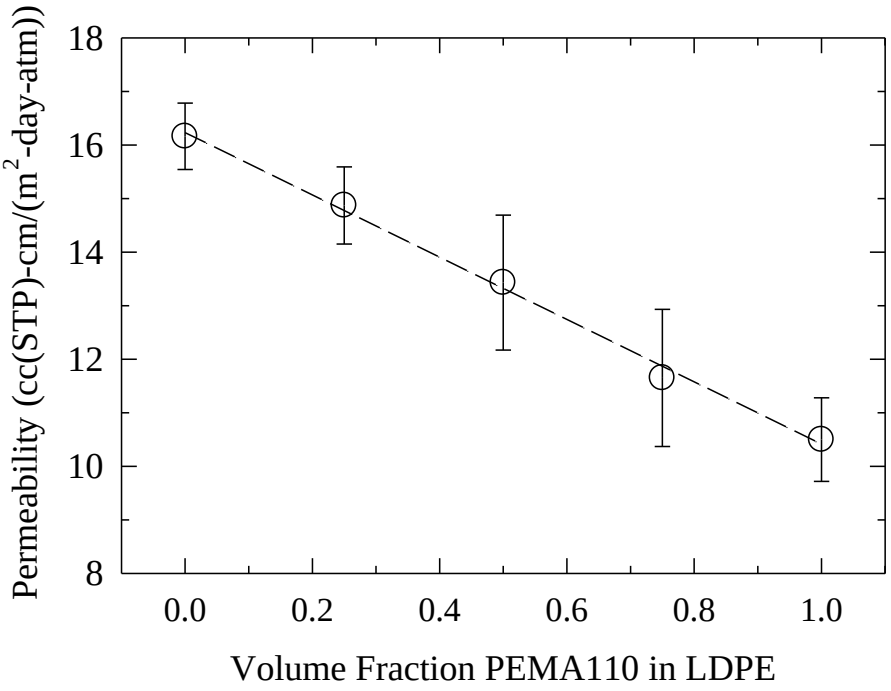

Figure 3.9 Oxygen permeability of LDPE/PEMA110 blends

It is noteworthy to mention that oxygen transport probes the amorphous phase. The crystalline phase of polymers is generally impermeable and insoluble for even small gas molecules like oxygen. Therefore, our gas permeability measurements point to the miscibility of LDPE and LLDPE-g-MA in the amorphous regions of the semicrystalline blends. Among the different polyolefin systems, the miscibility of LLDPE/LDPE blends seems to be the least studied and the available reports provide inconsistent conclusions on the miscibility. Some LLDPE/LDPE compositions were found to be miscible, some

partially miscible, and some even immiscible. Structural factors such as molecular weight, length of chain branches, and chain branch content were shown to affect the miscibility [43-46].

Oxygen permeability of PEMA110, 10.5 ± 0.8 SPU (standard permeability units, see Experimental section), was found to be lower than that of LDPE, 16.2 ± 0.6 SPU. One of the main reasons for the lower oxygen permeability of PEMA110 could be a larger maleic anhydride content which makes a polymer more polar. Polar polymers typically exhibit higher gas barrier [47].

Oxygen Permeability of Bulk Nanocomposites

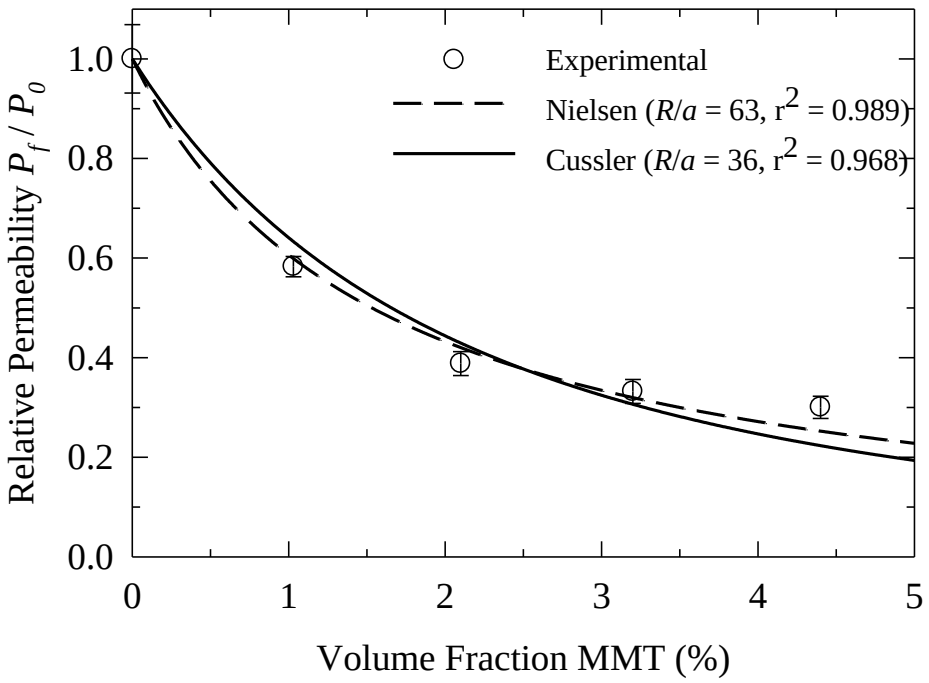

Figure 3.10 Relative oxygen permeability of PEMA528 nanocomposite films versus volume fraction of MMT: Experimental data and fits using Nielsen and Cussler equations

Oxygen permeabilities of PEMA528/Cloisite®20A nanocompoites are reported in Table 3.4. As one can see, adding nanoclay significantly enhances the gas barrier performance of a polymer. Oxygen permeability decreased by 42 and 67% after adding 1.0 and 4.4% (vol/vol) of the nanoclay, respectively. Figure 3.10 exhibits a traditional plot of the relative oxygen permeability ($\frac{P_f}{P_0}$), where P_f is the permeability of a filled nanocomposite system and P_0 is the permeability of a pure polymer (in this case PEMA528), plotted versus the MMT volume fraction. Two models originally proposed by Nielsen and by Cussler were employed to fit the data [11, 13]. The models predict the relative permeability of composite films with well dispersed platelets oriented in the direction parallel to the film surface. It is generally accepted that the Nielsen equation (Equation 3.1) is more applicable in the dilute particulate concentration regime defined as follows, $\phi << 1$, $\alpha\phi << 1$. Where, ϕ, is the platelet volume fraction and $\alpha = \frac{R}{a}$ is the platelet aspect ratio. The platelets in this regime are set apart by a distance greater than their average half-length, *R*, and contribute independently to the gas transport. In turn, the Cussler equation (Equation 3.2) is more applicable in the semidilute concentration regime defined as follows, $\phi << 1$, $\alpha\phi >> 1$. The platelets are spaced by a distance comparable to their average half-length in this regime so they contribute more cooperatively to the transport mechanism which in this case becomes more localized and confined [10].

$$\frac{P_f}{P_0} = \frac{1-\phi}{1+\alpha\phi} \tag{3.1}$$

$$\frac{P_f}{P_0} = \frac{1-\phi}{(1+\frac{2\alpha\phi}{3})^2} \tag{3.2}$$

Both models assume that the relative permeability, $\frac{P_f}{P_0}$, is related to the reduced cross-section area, $\frac{A_f}{A_0}$, and the tortuosity factor, τ, as follows, $\frac{P_f}{P_0} = \frac{A_f/A_0}{\tau}$. The tortuosity factor is similarly defined to be a ratio of the length of the tortuous path, l_f, associated with turning around the discs while traveling across the film to the length of the direct path, l_0. Both models effectively calculate the tortuosity factor by counting the number of platelets a permeant meets as it travels through the film. There is a relatively small difference between the final expressions for the tortuosity factors presented by the two models, i.e., $(1 + \alpha\phi)$ in the Nielsen model and $(1 + 2\alpha\phi/3)$ in the Cussler model. The major difference, however, arises in the way the two models define and calculate the reduced area, $\frac{A_f}{A_0}$. The Nielsen model defines the reduced area to be the area fraction of the polymer phase on a section typically calculated by employing the Delesse principle in stereological analysis [48]. According to this principle the volume fraction of the embedded phase must be equal to the area fraction on a section. Therefore, the reduced area in the Nielsen model is equal to the volume fraction of a polymer phase, $\frac{A_f}{A_0} = (1 - \phi)$. The Cussler model defines and calculates the reduced area very differently. The corresponding average volumes accessible for permeation in the unfilled and subsequently filled films are assumed to be a product of the corresponding bulk average accessible areas times the corresponding diffusion paths as follows, $V_0 = A_0 \cdot l_0$ and $V_0 - V_f = A_f \cdot l_f$. This leads to the final expression for the reduced area, $\frac{A_f}{A_0} = (1 - \phi)/(1 + 2\alpha\phi/3)$.

Table 3.4 Oxygen permeabilities of LDPE, PEMA528, and PEMA110 poly(ethylene) controls, PEMA110/LDPE blends, PEMA528/Cloisite®20A bulk nanocomposites with various MMT volume fractions, and PEMA110/Cloisite®20A composite with MMT content 1% (v/v)

Material	MMT Content (ϕ, vol/vol)	Permeability (SPU)
PEMA528	0	16.6 ± 1.2
PEMA528/Cloisite®20A	0.010	9.7 ± 0.3
PEMA528/Cloisite®20A	0.021	6.4 ± 0.4
PEMA528/Cloisite®20A	0.032	5.5 ± 0.4
PEMA528/Cloisite®20A	0.044	5.0 ± 0.3
LDPE	0	16.2 ± 0.6
PEMA110	0	10.5 ± 0.8
PEMA110/LDPE (25/75) Blend	0	14.9 ± 0.7
PEMA110/LDPE (50/50) Blend	0	13.4 ± 1.2
PEMA110/LDPE (75/25) Blend	0	11.7 ± 1.3
PEMA110/Cloisite®20A	0.010	5.4 ± 0.5

Standard permeability units (SPU): $(cc_{gas}(STP)\cdot cm)/(m^2\cdot day\cdot atm)$

The best fits of equations (1) and (2) to the experimental data ($\frac{P_f}{P_0}$ vs. ϕ) generated for PEMA528/Cloisite®20A nanocomposites are shown as the lines in Figure 3.10. Both models describe fairly well the experimental data with the aspect ratio, $\alpha = \frac{R}{a}$, to be the only fitting parameter. With an optimal value of α = 63, the Nielsen equation showed a slightly better fit (r^2 = 0.989) to the experimental data than the Cussler equation with α = 36 (r^2 = 0.968). One point at 4.4% (v/v), however, noticeably deviated from the best fits. The relative permeability for this composition was found to be larger than the values predicted by the models which we believe was due to a sizable decrease of the clay particle aspect ratio at this clay composition as it was reported earlier in the morphology

section for PEMA528/Cloisite®20A bulk nanocomposites. Despite the Nielsen model overall showing a better fit to the experimental data, the α value predicted by this model was larger than the average aspect ratios, $\bar{\alpha}$, determined by TEM for the various compositions by about a factor of 3 (see Table 3.1). In contrast, the aspect ratio predicted by the Cussler model exhibited a satisfactory agreement with the TEM data, excluding the point at ϕ = 4.4% (v/v). A question can therefore be posed as to which of the two equations provides a more accurate description. It may be difficult to come to a definitive answer with the existing morphological information because there is a general problem with TEM analysis as it has a tendency to overestimate the fraction of smaller particles imbedded in the polymer matrix due to a "cross-section" effect [49]. If the particle centers are situated outside the microtome slice their characteristic dimensions will appear smaller on the corresponding TEM images and the average particle size representing a distribution also will be affected, as it will appear smaller. More dramatic underestimation of the particle sizes is expected if the slice thickness is considerably smaller than the measured particle dimension. In our case the slice thickness, about 100 nm, was, however, comparable with the clay particle lateral dimension. So, it is quite unlikely that the particle size distribution was significantly affected by the "cross-section" effect. This argument is in favor of using the Cussler equation to describe the permeation data as it appears to agree better with the morphological observations. The Cussler equation has been previously shown in other multilayered/highly filled film systems to better represent permeation behaviors than does the Nielson model [50].

Oxygen Permeability of Un-annealed and Annealed Nanocomposite Multilayers

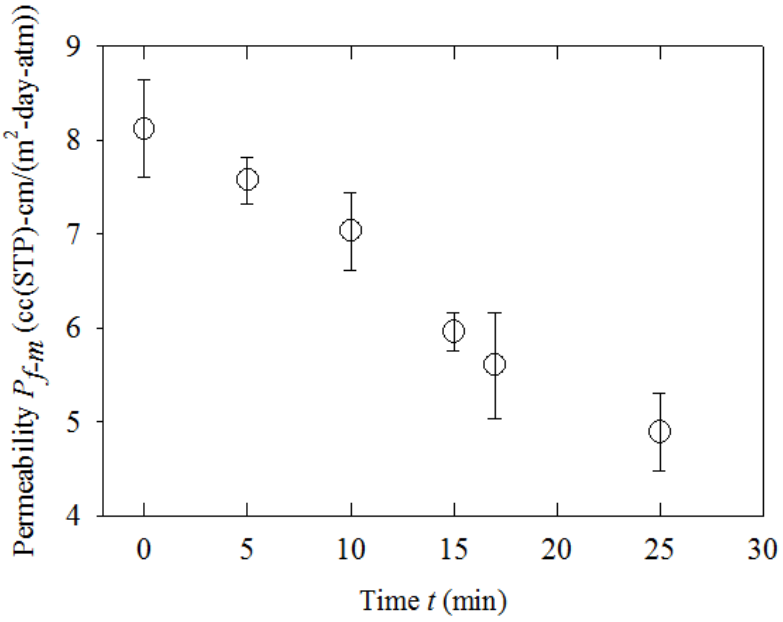

Figure 3.11 Oxygen permeability, $P_{f\text{-}m}$, of a nanocomposite multilayer versus annealing time at 200°C

Figure 3.11 shows the permeability, $P_{f\text{-}m}$, of the filled nanocomposite multilayer films versus annealing time, t. The permeability data are also reported in Table 3.5. The multilayers exhibited a gradual decrease in oxygen permeability with annealing time from the initial value, 8.1 SPU, prior to annealing (t = 0 min), to 4.9 SPU after annealing for 25 minutes corresponding to a 40% permeability decrease relative to the un-annealed film, which is significant. It is also interesting to estimate the relative permeability, $\frac{P_{f-m}}{P_{0-m}}$, prior to and after annealing assuming a value for the unfilled multilayer film, $P_{0\text{-}m}$, of 13.4 which corresponds to the experimentally determined permeability of a 50/50 blend of LDPE and PEMA110. Viscosity differences between the unfilled PEMA110 and LDPE prevented the multilayering of these two polymers. With an overall MMT content of 0.5% (v/v) (nanoclay only in half the layers), the relative permeabilities could be approximated for the un-annealed and after annealing for 25 minutes films as 0.60 and

0.37 respectively. For comparison, with the same mineral content, the relative permeability of the PEMA528/Cloisite®20A nanocomposite control is 0.76. Therefore, if the relative permeabilities of a nanocomposite control and a nanocomposite multilayer prior to annealing are somewhat comparable, after annealing the relative permeability of a multilayer is markedly smaller.

Table 3.5 Directly measured oxygen permeability of un-annealed and annealed multilayers, and estimated permeabilities of LDPE- rich and nanocomposite layers

Annealing time (t, min)	Nanocomposite layer MMT volume fraction (v/v)	Volume fraction of PEMA110 in LDPE-rich layer	Multilayer permeability, ($P_{f\text{-}m}$, SPU)	*LDPE-rich layer permeability, (P_{LDPE}, SPU)	*Nanocomposite layer permeability, ($P_{f\text{-}l}$, SPU)
0	0.010	0	8.1 ± 0.5	16.2 ± 0.6	5.5
5	0.018	0.30	7.6 ± 0.3	14.6	3.6
10	0.020	0.33	7.0 ± 0.4	14.4	3.0
15	0.022	0.36	6.0 ± 0.2	14.2	2.1
17	0.025	0.38	5.6 ± 0.6	14.0	1.7
25	0.043	0.44	4.9 ± 0.4	13.7	0.9

Standard permeability units (SPU): $(cc_{gas}(STP)\cdot cm)/(m^2\cdot day\cdot atm)$
*Permeabilities without uncertainty were calculated as described in discussion

A series model was employed to describe the permeability of the un-annealed and annealed PEMA110 nanocomposite/LDPE multilayer, $P_{f\text{-}m}$. The permeability, $P_{f\text{-}m}$, is a function of the permeability, $P_{f\text{-}l}$, and the thickness, $L_{f\text{-}l}$, of the nanocomposite layers, and the permeability, P_{LDPE}, and the thickness, L_{LDPE}, of the LDPE-rich layers as follows:

$$\frac{L_{LDPE}+L_{f-l}}{P_{f-m}} = \frac{L_{f-l}}{P_{f-l}} + \frac{L_{LDPE}}{P_{LDPE}} \tag{3.3}$$

While the information on $P_{f\text{-}m}$, $L_{f\text{-}l}$, and L_{LDPE} is experimentally available (see Table 3.2 and Table 3.5), $P_{f\text{-}l}$ and P_{LDPE} are two unknowns that have to be decoupled. The transport model can be simplified and $P_{f\text{-}l}$ and P_{LDPE} decoupled if it is assumed that interdiffusion occurs solely by diffusing polymer chains from the PEMA110 nanocomposite layers into the LDPE layers. We believe that this assumption is reasonable as the observed prominent moving boundary effect points to a large mismatch of the diffusion coefficients while a short duration of the annealing process in principle suggests that only a negligible amount of slow-moving long branched LDPE can interdiffuse into the nanocomposite layers. We assume that due to a very short processing time during melt coextrusion, the extent of interdiffusion in un-annealed multilayers is minimal; therefore the un-annealed multilayers consist of pure LDPE and pure PEMA110/nanoclay layers. The simplification made above for the transport problem enabled us to calculate the volume composition of the LDPE-rich layers from the layer thickness variation upon annealing (see Table 3.2), and then based on these calculations to estimate the permeability of LDPE-rich layers using the permeability versus composition plot shown in Figure 3.9 for LDPE/LLDPE-g-MA blends. After evaluating the permeability of the LDPE-rich layers, the permeability of the nanocomposite layers, $P_{f\text{-}l}$, was calculated using Equation 3.3. The permeabilities of the LDPE-rich and nanocomposite layers are reported in Table 3.5.

As one can see in Table 3.5, the oxygen permeability of the LDPE-rich layers, P_{LDPE}, rapidly decreased upon annealing by about 10% after the first 5 minutes due to interdiffusion of LLDPE-g-MA chains and then continued to decrease with time but rather slowly. After 25 minutes of annealing the permeability of the LDPE-rich layers

decreased by only 15%. The oxygen permeability of the nanocomposite layers, $P_{f\text{-}l}$, decreased more dramatically. After the first five minutes of annealing the permeability decreased by 35% and after 25 minutes by 84%. The calculated permeability of the nanocomposite layers prior to annealing of a multilayer, 5.5 SPU, was found to be very similar to that experimentally determined for the melt pressed PEMA110/nanoclay bulk nanocomposite film with 1% (v/v) of MMT, i.e. 5.4 ± 0.5 SPU. This fact is in agreement with our early assumption that the extent of interdiffusion during melt coextrusion was minimal. The permeability of the nanocomposite layers after annealing for 25 minutes, 0.9 SPU, was markedly smaller. A question was posed if this substantial reduction of oxygen permeability upon annealing is solely due to the increase of particulate concentration or if it involves additional factors. To answer this question we compared the relative permeabilities, $\frac{P_{f-l}}{P_0}$, of the PEMA110/Cloisite®20A nanocomposite layers after annealing for 25 minutes and the PEMA528/Cloisite®20A bulk nanocomposite control with MMT content 4.4% (v/v), $\frac{P_f}{P_0}$,. Evidently, the relative permeability of nanocomposite layers after annealing, 0.086, is significantly smaller than the relative permeability of the bulk nanocomposite control, 0.30, despite similar MMT content. We believe that an additional reason for this perceptible barrier reinforcement in the nanocomposite layers, upon annealing and interdiffusion, is the formation of longer skewed clay aggregates which is in accord with the morphological observations.

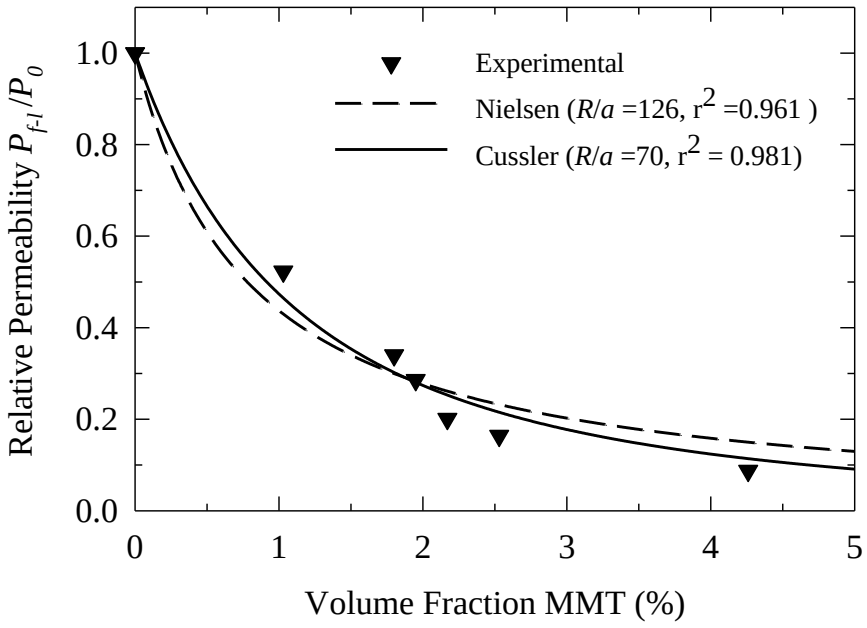

Figure 3.12 Relative oxygen permeability versus volume fraction of MMT for PEMA110/MMT layers in a multilayer annealed for various times: Experimental data and fits using Nielsen and Cussler equations

The relative oxygen permeability, $\frac{P_{f-l}}{P_0}$, of the contracted upon annealing nanocomposite layers versus the volume fraction of MMT in these layers (P_0 is the oxygen permeability of pure PEMA110) is shown in Figure 3.12. The volume fraction of MMT was calculated from the layer thickness analysis (Table 3.2). The composition after 10 minutes of annealing was found by means of extrapolation using the layer thickness dependence vs. $t^{1/2}$ depicted in Figure 3.5. The best fits of Equations (3.1) and (3.2) to the experimental data can be seen in Figure 3.12 as lines. With an optimal value $\alpha = \frac{R}{a} = 70$, the Cussler equation showed a better fit ($r^2 = 0.981$) to the experimental data than the Nielsen equation with $\alpha = 126$ ($r^2 = 0.961$). Moreover, the aspect ratio predicted by the Cussler model also exhibited a much better agreement with the TEM data (see Table 3.3).

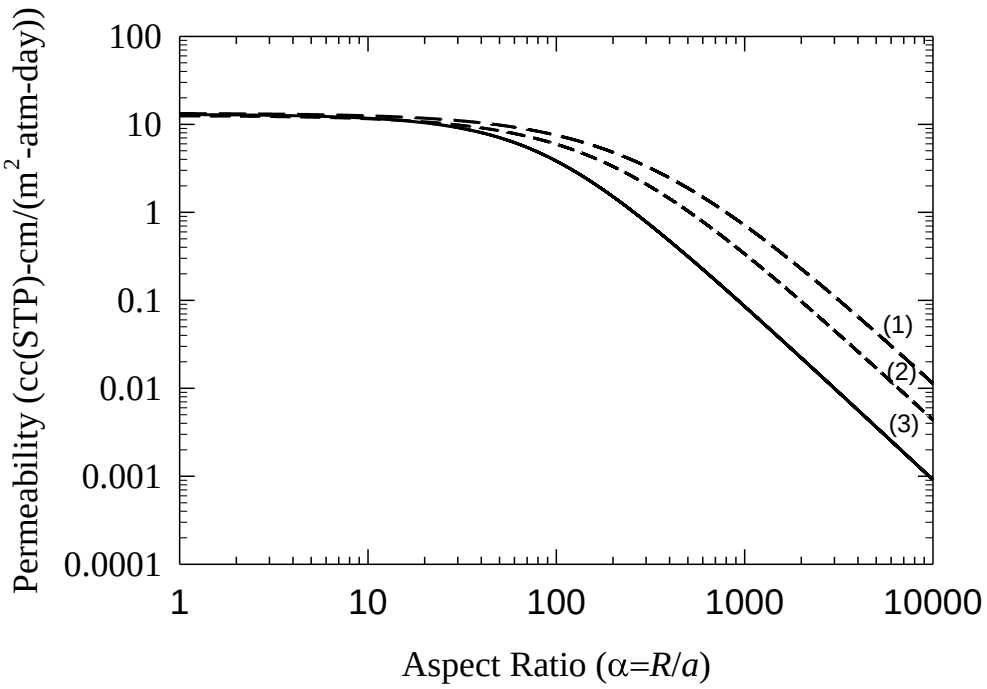

Figure 3.13 Predictions using the Cussler model for oxygen permeability versus platelet aspect ratio for: (1) bulk nanocomposite; (2) un-annealed multilayer; (3) multilayer annealed for 25 minutes. In each system overall MMT content is 0.5% (v/v).

Finally, we want to comment on the prospect of the multilayer approach described in this article, assuming similar polyethylene systems and mineral compositions are used. Evidently, future success depends on the ability to use higher aspect ratio particulates. Figure 3.13 shows the predicted oxygen permeability versus platelet aspect ratio for a bulk nanocomposite with a MMT content of 0.5% (v/v) (1), an un-annealed multilayer (2), and a multilayer annealed at 200°C for 25 minutes (3). In the un-annealed multilayer, the filled layer mineral content is assumed to be 1% (v/v) with a filled-unfilled initial layer thickness ratio 1:1. Subsequently, the overall MMT content in the multilayers is 0.5% (v/v) as well. For the multilayers, the oxygen permeability of the nanocomposite layers was calculated first using the Cussler model (Equation 3.2) and then the overall permeability was estimated via the series model (Equation 3.3). We assumed that the

LDPE and PEMA110-rich layers exhibit the same expansion/contraction behavior due to interdiffusion and the moving boundary effect as reported in Table 3.2. The LDPE/PEMA110 (50/50) blend was assumed to be the matrix for the bulk nanocomposite and the Cussler equation was used to predict the oxygen permeability trend (1) for this system as well. Note, the oxygen permeability for the blend, 13.4 SPU determined experimentally is similar to that for LDPE/PEMA110 (50/50) multilayer estimated using the series model, 12.7 SPU.

The predicted oxygen permeability versus aspect ratio curves in Figure 3.13 qualitatively displayed very similar tendencies. Within the aspect ratio range less than 40 the permeability decreased slowly, essentially showing a plateau on a log-log graph, after which the decrease was fairly rapid. For comparison, the permeability of the annealed multilayers with α =1, 40, 100, 1000, and 10000 was 12.941, 8.050, 3.830, 0.085, and 0.0009 SPU, respectively. As expected, among these three systems the annealed multilayer exhibited the highest and the bulk nanocomposite the lowest gas barrier performance with the trend for the un-annealed multilayer in between. The difference between the trends in the plateau region range, i.e. α ~1-40, however, was very minor gradually becoming more pronounced with larger α permeability trends above α =500 continued to decrease with somewhat comparable rates. For comparison, with α =36, 70, 500, 1000, and 10000, the oxygen permeability was 1.3, 1.6, 6.0, 8.4, and 12.5 times smaller than the permeability of a bulk nanocomposite, and 1.1, 1.3, 3.3, 4.0, and 4.8 times smaller than the permeability of a un-annealed multilayer, respectively. Therefore, if the nanoparticulates that exhibit a very high aspect ratio (α =500-2000), such as synthetic fluorohectorite or graphene (described in Chapter 4) had been dispersed in the

LLDPE-g-MA matrix, the annealed multilayer approach would result in an increase of the gas barrier of about two orders of magnitude relative to the unfilled matrix while an increase of one order of magnitude for a bulk nanocomposite with the same particulate content [51-53]. Multilayering without annealing also improves the gas barrier as compared to the bulk nanocomposite but the effect is clearly smaller. As one can see from the Figure 3.13, MMT nanoparticulates exhibit too small of an aspect ratio and their effect on gas barrier is relatively minor. However, if nanoparticulates with larger aspect ratios are employed, much more impressive barrier enhancement can be anticipated.

Conclusion

A direct melt compounding of organoclay Cloisite®20A with commercial grades of MA-grafted LLDPE (DuPont Fusabond® series) in a twin screw extruder produced bulk nanocomposites with a highly delaminated morphology. The organoclay in the polymer matrix was dispersed to the level of single nanoplatelets that were often arranged in tiny aggregates (particles) consisting of 2-4 nanoplatelets skewed in a staircase fashion. The length and aspect ratio of these skewed aggregates were larger than those of a single nanoplatelet. With increasing the MMT content, the clay particle length and aspect ratio decreased. This effect was attributed to an increase in the bulk nanocomposite melt viscosity which led to higher shear stresses. Under these more vigorous mixing conditions individual silicate layers were peeled off more efficiently. As the number of single layers per skewed aggregate was reduced, the particles appeared shorter.

Layer multiplying coextrusion was employed to create films consisting of alternating layers of LDPE and LLDPE-g-MA/Cloisite®20A nanocomposite. The MMT

concentration within the nanocomposite layers was increased through annealing of the multilayered films in the melt state. This process took advantage of the mismatch in the diffusion coefficients between LDPE and LLDPE-g-MA polymer chains leading to a moving boundary that caused the LLDPE-g-MA rich particulate filled layers to contract while the LDPE rich layers expanded. In contrast to the effect of the shortening of clay particles during the melt compounding of nanocomposites in an extruder, the analysis LLDPE-g-MA/Cloisite®20A layers in the multilayer system revealed an unexpected lengthening of clay particles upon annealing. The lack of a stress field during interdiffusion and nanocomposite layer contraction apparently allowed for the growth of skewed aggregates as nanoplatelets and clay particles impinged upon one another.

The multilayered nanocomposite system exhibited a gradual improvement of oxygen barrier with annealing and the contraction of the filled layers led to a 63% reduction of the oxygen permeability relative to an unfilled LDPE/LDPE-g-MA system. This gas barrier reinforcement effect far exceeded the 24% reduction anticipated assuming the same mineral content in the nanocomposite bulk control. A series model, under the assumption that interdiffusion occurs solely by diffusing polymer chains from the LLDPE-g-MA/nanoclay layers into the LDPE layers, enabled calculating the oxygen permeability of the filled layers upon annealing and contraction. After annealing, the nanocomposite layers exhibited a 91% reduction of the oxygen permeability as compared to the unfilled PEMA110 polymer. In a nanocomposite control with the same mineral content, the oxygen permeability was reduced by 70%. This additional gas barrier enhancement was attributed to the formation of longer skewed aggregates upon annealing and the contraction of the filled layers, in accord with the morphological observations.

Cussler and Nielsen models have been employed to model the permeability data in the nanocomposite controls and the nanocomposite layers in a multilayer. Although both models described fairly well the experimental data, the Cussler model overall showed a better agreement with the morphological observations.

While the increase in gas barrier properties observed using this new methodology is by itself novel and interesting, it is clear from the model analysis that increasing the nanoplatelet aspect ratios, and perhaps the initial nanoclay concentration in the filled layers will lead to even more impressive barrier results. Indeed, with higher aspect ratio fillers, these results may prove remarkable, especially if the same trends of particle length growth are observed.

Acknowledgements

The authors are grateful to the National Science Foundation for support of this work through the Center for Layered Polymeric Systems (DMR 0423914) and the GK-12 fellowship program (DGE-1007911, Award #0947944). Special thanks are to be given to the Dr. Baer and his coextrusion team at Case Western Reserve University for their careful manufacturing of the multilayered films. We also would like to thank Dr. William Jarrett from the School of Polymers and High Performance Materials for the NMR characterization of the polyethylene resins.

References

1] Peacock AJ. Handbook of Polyethylene: Structures: Properties, and Applications. Boca Raton, Florida; CRC Press; 2000.

2] Bissot TC. Performance of High-Barrier Resins with Platelet-Type Fillers, in Barrier Polymers and Structures, ACS Symposium Series 423 (Ed. Koros WJ). Washington, DC; American Chemical Society; 1990: Ch. 11, 225-238.

3] Ray SS, Okamoto M. Polymer/layered silicate nanocomposites: a review from preparation to processing. Prog Polym Sci 2003; 28: 1539-1641. doi:10.1016/j.progpolymsci.2003.08.002

4] Alexander M, Dubois P. Polymer-layered silicate nanocomposites: preparation, properties and uses of a new class of materials. Mater Sci Eng: R: Reports 2000; 28(1): 1-63. doi: 10.1016/S0927-796X(00)00012-7

5] Paul DR, Robeson LM. Polymer nanotechnology: Nanocomposites. Polymer 2008; 49(15): 3187-3204. doi: 10.1016/j.polymer.2008.04.017

6] Choudalakis G, Gotsis AD. Permeability of polymer/clay nanocomposites: A review. Eur Polym J 2009; 45(4): 967–984. doi: 10.1016/j.eurpolymj.2009.01.027

7] Priolo MA, Holder KM, Gamboa D, Grunlan JC. Influence of Clay Concentration on the Gas Barrier of Clay-Polymer Nanobrick Wall Thin Film Assemblies. Langmuir 2011; 27(19): 12106-12114. doi: 10.1021/la201584r

8] Nazarenko S, Meneghetti P, Julmon P, Olson BG, Qutubuddin S. Gas barrier of polystyrene montmorillonite clay nanocomposites: Effect of mineral layer aggregation. J Polym Sci Pol Phys 2007; 45(13): 1733-1753. doi: 10.1002/polb.21181

9] Hotta S, Paul DR. Nanocomposites formed from linear low density polyethylene and organoclays. Polymer 2004; 45(22): 7639–7654. doi: 10.1016/j.polymer.2004.08.059

10] Fredrickson GH, Bicerano JJ. Barrier properties of oriented disk composites. J Chem Phys 1999; 110(4): 2181-2188. doi:10.1063/1.477829

11] Nielsen LE. Models for the Permeability of Filled Polymer Systems. J Macromol Sci A Chem 1967; 1(5): 929-942. doi: 10.1080/10601326708053745

12] Cussler EL, Hughes SE, Ward WJ III, Aris RJ. Barrier membranes. J Membrane Sci 1988; 38(2): 161-174. doi: 10.1016/S0376-7388(00)80877-7

13] Lape NK, Nuxoll EE, Cussler EL. Polydisperse flakes in barrier films. J Membrane Sci 2004; 236(1-2): 29-37. doi: 10.1016/j.memsci.2003.12.026

14] Mueller C, Nazarenko S, Ebeling T, Schuman TL, Hiltner A, Baer E. Novel structures by microlayer coextrusion-talc-filled PP, PC/SAN, and HDPE/LLDPE. Polym Eng Sci 1997; 37(2): 355-362. doi: 10.1002/pen.11678

15] Nazarenko S, Hiltner A, Baer E. Polymer microlayer structures with anisotropic conductivity. J Mater Sci 1999; 34(7): 1461 – 1470. doi: 10.1023/A:1004527205239

16] Sekelik DJ, Stepanov EV, Nazarenko S, Hiltner A, Baer E. Oxygen barrier properties of crystallized and talc-filled poly(ethylene terephthalate). J Polym Sci Pol Phys 1999; 37(8): 847-857. doi: 10.1002/(SICI)1099-0488(19990415)37:8<847::AID-POLB10>3.0.CO;2-3

17] Im J, Hiltner A, Baer E. Microlayer Composites, in High Performance Polymers (Eds. Baer E, Moet A). New York; Hanser 1991: 175.

18] Wang HP, Keum JK, Hiltner A, Baer E. Confined Crystallization of PEO in Nanolayered Films Impacting Structure and Oxygen Permeability. Macromolecules 2009; 42(18): 7055–7066. doi: 10.1021/ma901379f

19] Song H; Singer K, Lott J, Wu Y, Zhou J, Andrews J, Baer E, Hiltner A, Weder C. Continuous melt processing of all-polymer distributed feedback lasers. J Mater Chem 2009; 19(40): 7520-7524. doi: 10.1039/B909348F

20] Nazarenko S, Dennison M, Schuman T, Stepanov EV, Hiltner A, Baer E. Creating Layers of Concentrated Inorganic Particles by Interdiffusion of Polyethylenes in Microlayers. J Appl Polym Sci 1999; 73(14): 2877-2885. doi: 10.1002/(SICI)1097-4628(19990929)73:14<2877::AID-APP11>3.0.CO;2-O

21] Klein J. The Interdiffusion of Polymers. Science 1990; 250(4981): 640-646. doi: 10.1126/science.250.4981.640

22] Kausch HH, Tirrell M. Polymer Interdiffusion. Annu Rev Mater Sci 1989; 19: 341-377. doi: 10.1146/annurev.ms.19.080189.002013

23] Smigelskas AD, Kirkendall EO. Zinc Diffusion in Alpha Brass. Trans. AIME 1947; 171: 130–142.

24] Kramer EJ, Green P, Palmstrøm CJ. Interdiffusion and marker movements in concentrated polymer-polymer diffusion couples. Polymer 1984; 25(4): 473-480. doi: 10.1016/0032-3861(84)90205-2

25] Green PF, Palmstrram CJ, Mayer JW, Kramer EJ. Marker displacement measurements of polymer-polymer interdiffusion, Macromolecules 1985; 18(3): 501-507. doi: 10.1021/ma00145a033

26] Keskkula H, Paul DR. Diffusion of miscible polymers in multilayer films. J Appl Polym Sci 1987; 34(5): 1861-1877. doi: 10.1002/app.1987.070340506

27] Pollock G, Nazarenko S, Hiltner A, Baer E. Interdiffusion in microlayered polymer composites of polycarbonate and a copolyester. J Appl Polym Sci 1994; 52(2): 163-176. doi: 10.1002/app.1994.070520205

28] Lai CY, Ponting MT, Baer E. Influence of interdiffusion on multilayered gradient refractive index (GRIN) lens materials. Polymer 2012; 53(6): 1393-1403. doi: 10.1016/j.polymer.2012.01.036

29] Zhao R, Macosko CW. Polymer-Polymer Mutual Diffusion via Rheology of Coextruded Multilayers. AICHE J 2007; 53(4): 978-985. doi: 10.1002/aic.11136

30] Schuman T, Stepanov EV, Nazarenko S, Capaccio G, Hiltner A, Baer E. Interdiffusion of Linear and Branched Polyethylene in Microlayers Studied via Melting Behavior. Macromolecules 1998; 31(14): 4551-4561. doi: 10.1021/ma971758e

31] Schuman T, Nazarenko S, Stepanov EV, Magonov S, Hiltner A, Baer E. Solid state structure and melting behavior of interdiffused polyethylenes in microlayers. Polymer 1999; 40(26): 7373 – 7385. doi: 10.1016/S0032-3861(99)00013-0

32] Shah RK, Paul DR. Organoclay degradation in melt processed polyethylene nanocomposites. Polymer 2006; 47(11): 4075-4084. doi: 10.1016/j.polymer.2006.02.031

33] Fornes TD, Yoon PJ, Keskkula H, Paul DR. Nylon 6 nanocomposites: the effect of matrix molecular weight. Polymer 2001; 42(25): 9929-9940. doi: 10.1016/S0032-3861(01)00552-3

34] Mueller CD, Kerns J, Ebeling T, Nazarenko S, Hiltner A, Baer E. Polymer Process Engineering 97; Coates PD Ed; The Institute of Materials: London, 1997:137-157.

35] Russell KE, Kelusky EC. Grafting of maleic anhydride to n-eicosane. J Polym Sci Pol Chem 1988; 26(8): 2273-2280. doi: 10.1002/pola.1988.080260821

36] Miyauchi K, Saito K. 1H NMR assignment of oligomeric grafts of maleic anhydride-grafted polyolefin. Magn Reson Chem 2012; 50(8): 580-583. doi: 10.1002/mrc.3839

37] Chavarria F, Paul DR. Comparison of nanocomposites based on nylon 6 and nylon 66. Polymer 2004; 45(25): 8501-8515. doi: 10.1016/j.polymer.2004.09.074

38] Lee H-S, Fasulo PD, Rodgers WR, Paul DR. TPO based nanocomposites. Part 1. Morphology and mechanical properties. Polymer 2005; 46(25): 11673-11689. doi: 10.1016/j.polymer.2005.09.068

39] Nam PH, Maiti P, Okamoto M, Kotaka T, Hasegawa N, Usuki A. A hierarchical structure and properties of intercalated polypropylene/clay nanocomposites. Polymer 2001; 42(23): 9633-9640. doi: 10.1016/S0032-3861(01)00512-2

40] Galgali G, Ramesh C, Lele A. A Rheological Study on the Kinetics of Hybrid Formation in Polypropylene Nanocomposites. Macromolecules 2001; 34(4): 852-858. doi**:** 10.1021/ma000565f

41] Hopfenberg HP, Paul DR. Transport Phenomena in Polymer Blends, in Polymer Blends (Eds. Paul DR, Newman S). New York, New York, Academic Press Inc. 1978; 1: 445-489.

42] Gonzalez-Montiel A, Keskkula H, Paul DR. Morphology of nylon 6/ polypropylene blends compatibilized with maleated polypropylene. J Polym Sci Pol Phys 1995; 33(12): 1751-1767. doi: 10.1002/polb.1995.090331206

43] Cho K, Ahn T, Park I, Lee BH, Choe S. Influence of the Melt Index of Low Density Polyethylene on the Properties in the Blend with Linear Low Density Polyethylenes. J Ind Eng Chem 1997; 3(2): 147-154.

44] Shin TJ, Lee B, Lee J, Jin S, Sung BS, Han YS, Lee C, Stein RS, Ree M. Small-angle neutron scattering study of the miscibility of metallocene-catalyzed octene linear low-density polyethylene and low-density polyethylene blends. J Appl Crystallogr 2009; 42(2): 161-168. doi: 10.1107/S0021889809002854

45] Hussein IA, Williams MC. Rheological study of heterogeneities in melt blends of ZN-LLDPE and LDPE: Influence of M_w and comonomer type, and implications for miscibility. Rheol Acta 2004; 43(6): 602-614. doi: 10.1007/s00397-004-0356-9

46] Utracki LA, Schlund B. Linear low density polyethylenes and their blends: Part 4 shear flow of LLDPE blends with LLDPE and LDPE. Polym Eng Sci 1987; 27(20): 1512-1522. doi: 10.1002/pen.760272006

47] Salame M. Polym. Prediction of gas barrier properties of high polymers. Polym Eng Sci 1986; 26(22): 1543-1546. doi: 10.1002/pen.760262203

48] Chan SL. Image Analysis, in Fractography and Failure Mechanisms of Polymers and Composites (Ed. Roulin-Moloney AC). London; Elsevier Applied Science, 1989; 145-92.

49] Corté L, Leibler L. Analysis of polymer blend morphologies from transmission electron micrographs. Polymer 2005; 46(17): 6360-6368. doi: 10.1016/j.polymer.2005.05.109

50] Gupta M, Lin Y, Deans T, Baer E, Hiltner A, Schiraldi DA. Structure and gas barrier properties of poly(propylene-graft-maleic anhydride)/ phosphate glass composites prepared by microlayer coextrusion. Macromolecules 2010; 43(9): 4230-4239. doi: 10.1021/ma100391u

51] Kamena K. Nanoclays and Their Emerging Markets, in Functional Fillers for Plastics (Ed. Xanthos M). Weinheim, Germany; Willey-VCH Verlag GmbH & Co. KGaA, 2005; 163-174.

52] Souza DHS, Dahmouche K, Andrade CT, Dias ML. Structure, morphology and thermal stability of synthetic fluorine mica and its organic derivatives. Applied Clay Science 2011; 54(3–4): 226-234. doi: 10.1016/j.clay.2011.09.006

Supplementary Data

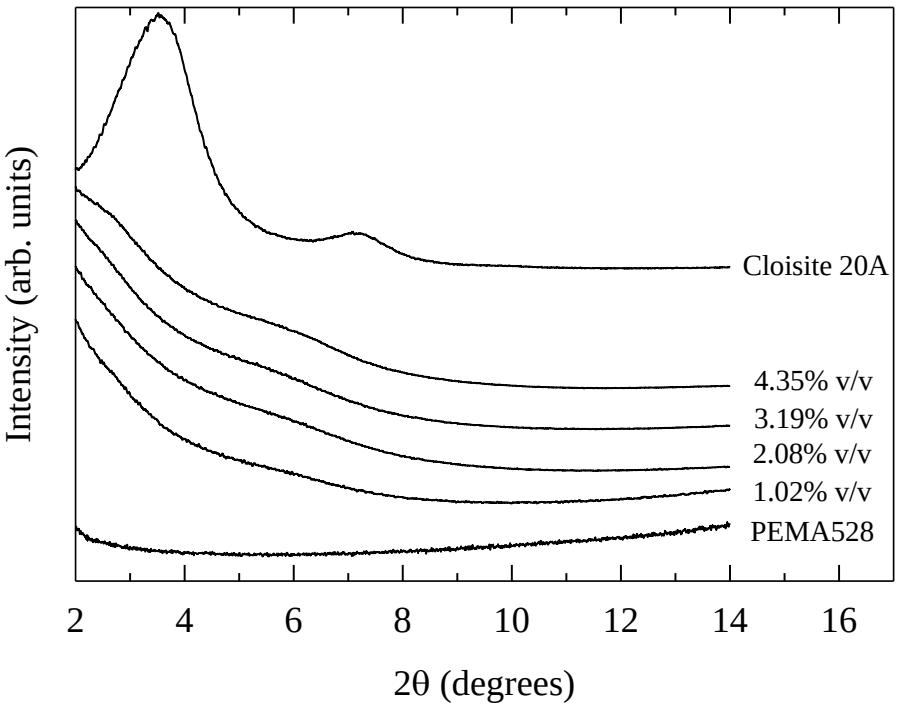

Figure 3.1 WAXS of pristine organoclay and PEMA528, and various bulk nanocomposites. Curves vertically offset for clarity

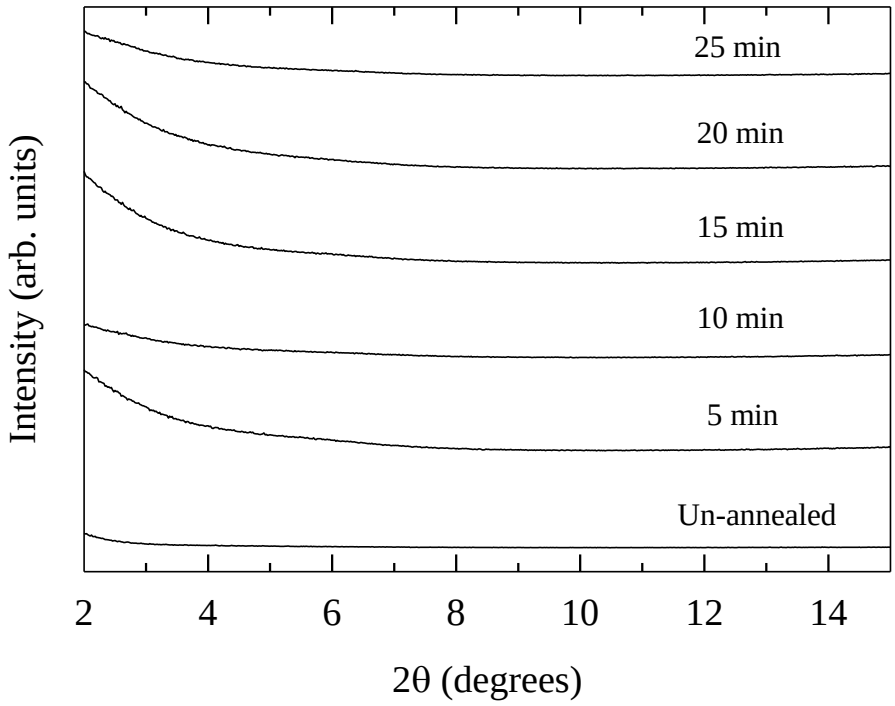

Figure 3.2 WAXS scans of as-made and annealed nanocomposite multilayers after annealing for various times at 200°C

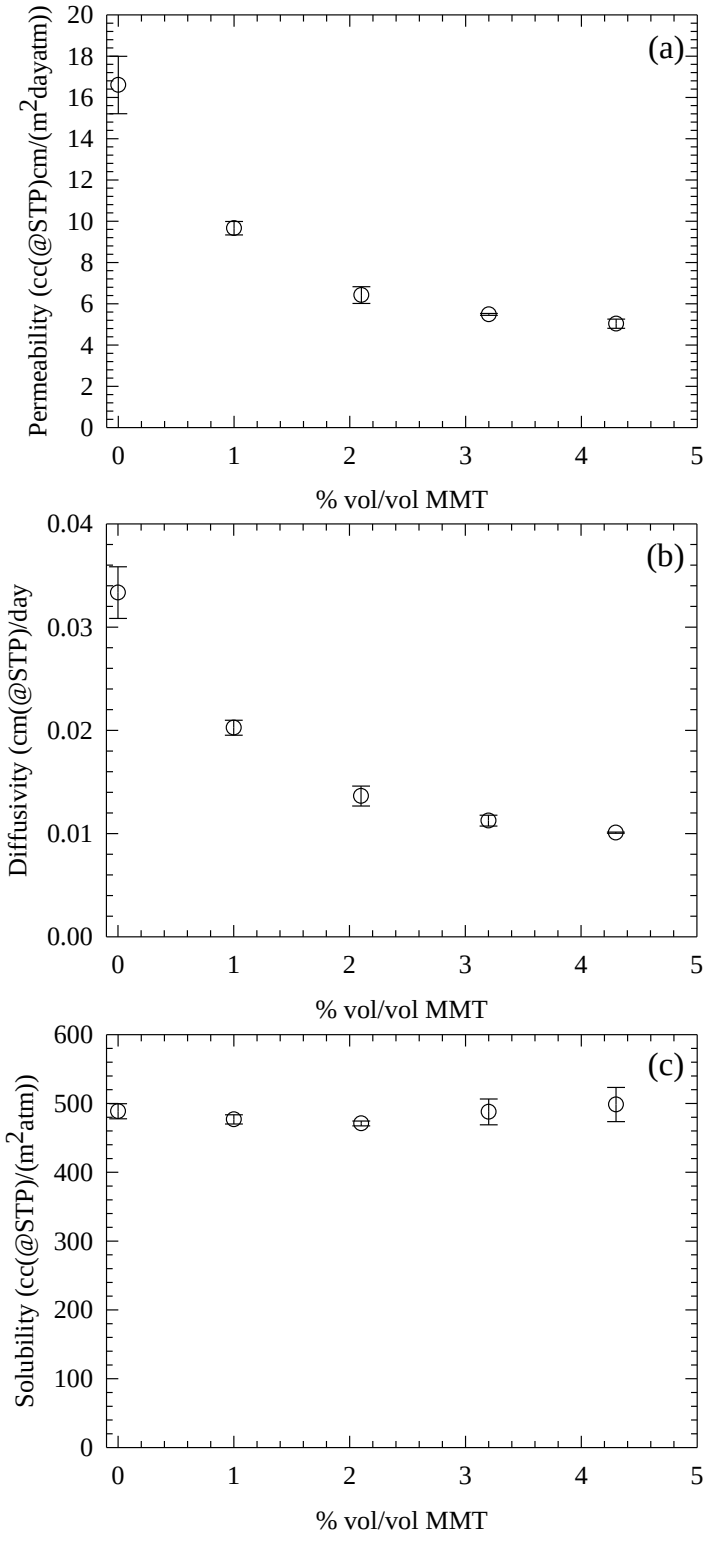

Figure 3.3 Effect of % volume fraction MMT on oxygen permeability (a), diffusivity (b), and solubility (c) for PEMA528 nanocomposites.

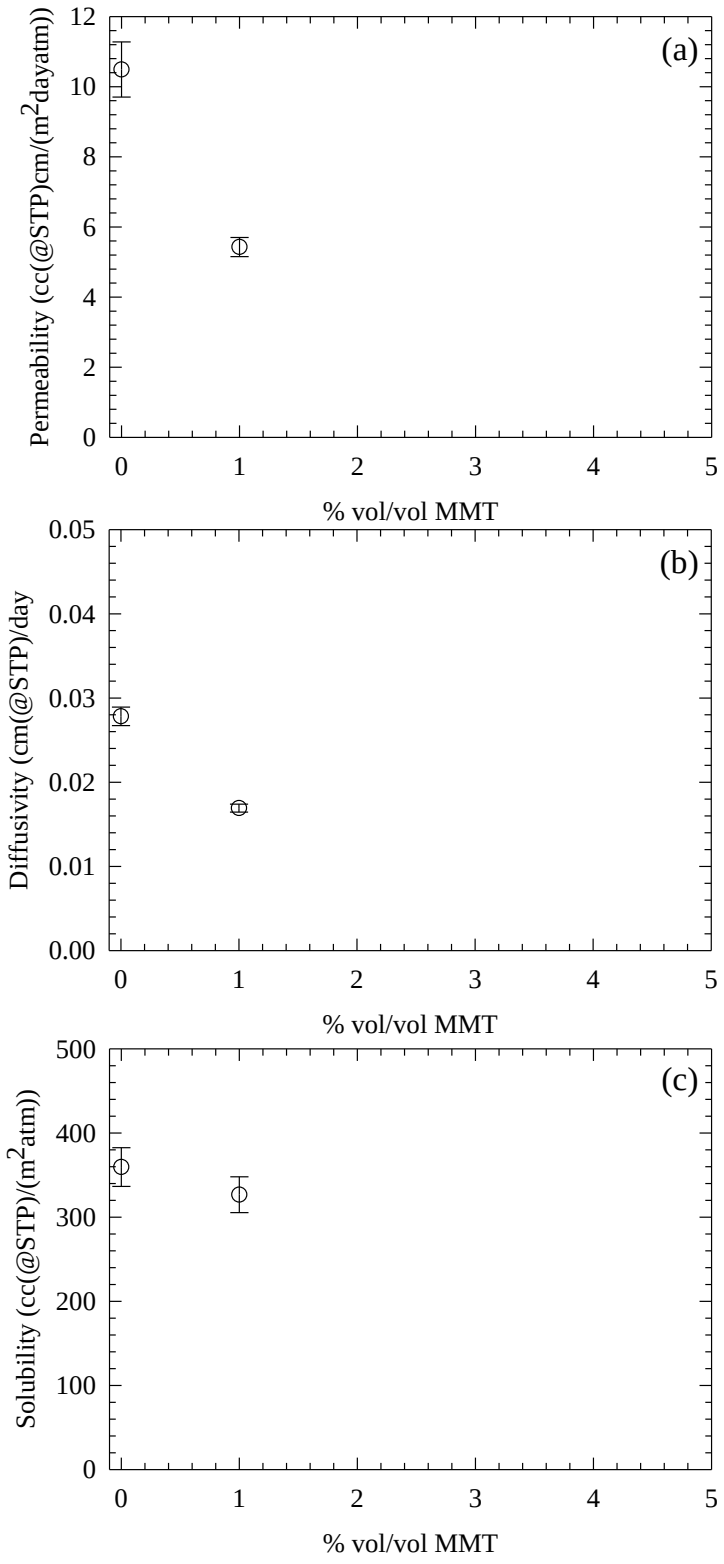
(a)
Permeability (cc(@STP)cm/(m2dayatm))
0
2
4
6
8
10
12
0
1
2
3
4
5
% vol/vol MMT
(b)
Diffusivity (cm(@STP)/day
0.00
0.01
0.02
0.03
0.04
0.05
0
1
2
3
4
5
% vol/vol MMT
(c)
Solubility (cc(@STP)/(m2atm))
0
100
200
300
400
500
0
1
2
3
4
5
% vol/vol MMT

Figure 3.4 Effect of % volume fraction MMT on oxygen permeability (a), diffusivity (b), and solubility (c) for PEMA110 nanocomposite utilized in multilayered systems.

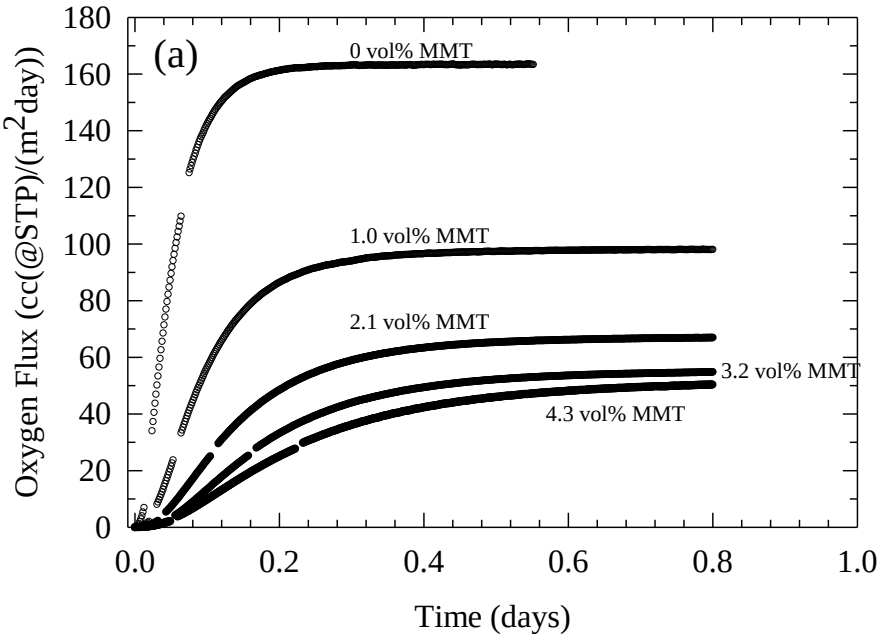

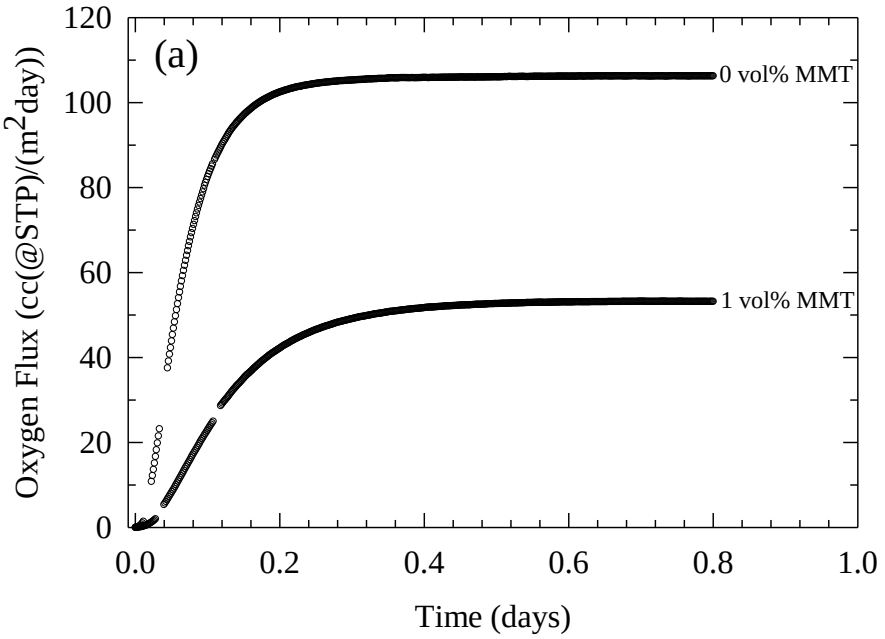

Figure 3.5 Experimental oxygen flux versus time data for the PEMA528 nanocomposites (a) and the PEMA 110 nanocomposite utilized in the multilayered systems.

CHAPTER IV – MECHANICAL AND BARRIER ANALYSIS OF GRAPHENE FILLED POLYETHYLENE FILMS: EFFECTS OF CONTROLLED INTERDIFFUSION ON MULTILAYERED GRAPHENE COMPOSITE FILMS

This chapter was co-authored with Vivek Vasagar, Beibei Chen, Jeremy J Decker, and Sergei Nazarenko

Abstract

Gas and fire barrier, mechanical, and thermal property enhancement of flexible polyethylene/ short stack graphene nanoplatelet (xGnP) composite systems were thoroughly analyzed in bulk composites and expanded to coextruded multilayers films. The xGnP platelets are desirable for nanocomposite formation due to their impermeable high aspect ratios and the potential for higher particulate loadings than conventional nanoclay platelet fillers allow for. Through incorporation of only a small amount of graphene nanoplatelets in LLDPE, a substantial increase in gas and fire barrier along with mechanical strength was observed. I.e., the oxygen/carbon dioxide permeability of the LLDPE system was halved with the addition of only 2 vol% xGnP while the tensile modulus increased almost three fold. The analyzed composites were also formulated into microlayer systems consisting of alternating linear low density polyethylene (LLDPE)/xGnP composites and pure low density polyethylene (LDPE) layers as a continuation of our studies exploiting the moving boundary phenomenon (asymmetric interlayer interdiffusion in the melt) in an effort to produce films with even better barrier properties that would only be expected at much higher particle loadings. Composite layer shrinkage was confirmed through optical microscopy and resulted in a decrease in

permeability for the coextruded films that reflected the barrier properties of composites multilayers with ~3-5 wt% more graphene nanoplatelets.

Introduction

Previously studied organoclay/ polyethylene composites left much to be desired in the way of processability and barrier enhancement. Therefore, graphene platelets were chosen as an alternative due to their perceived higher aspect ratios and potential for many other properties improvement. In contrast to most other readily available nanoplatelets, graphene is highly electrically and thermally conductive with a low density and high surface area, all while remaining relatively inexpensive when compared to nanoparticles like carbon nanotubes as its source material graphite is naturally abundant [1].

Graphene consists of a monolayer of sp^2-hybridized carbon atoms bonded in a "honeycomb" hexagonal lattice. Graphene sheets are derived from graphite which is made up of a crystal lattice comprised of stacks of parallel single carbon atom thick graphene sheets held together by weak van der Waals forces, separated from each other by 0.335 nm. These weak forces holding the graphene sheets together allow the sheets to slide against each other, giving graphite its commonly exploited lubricating properties. The distribution of the π orbital over an entire graphene sheet makes it both thermally and electrically conductive [1].

This research will utilize stacked graphene sheets, also known as graphitic/graphene nanoplatelets (GNPs). GNPs are multiple graphene sheets stacked together; however, they still exhibit high aspect ratios with lengths measured in micrometers and thicknesses typically less than 10 nanometers. GNPs are primarily obtained through either sulfuric acid-intercalated graphite or graphene oxide

intermediaries. xGNP, used in this study, starts as a sulfuric acid based intercalated graphite that is exfoliated by rapid heating in a microwave environment. The resultant expanded graphite is then pulverized with an ultrasonic processor to break the particles into individual graphene nanoplatelets of the desired dimensions [2].

Individual graphene sheets have been shown to exhibit an exceptional elastic modulus parallel to the plane, even higher than that of diamond. Perfect graphene sheets have been shown to obtain a Young's modulus of 1.0 TPa and fracture strength of 130 GPa through AFM nanoindentation [3]. Graphene sheets, without defects, are also reported to be impermeable to all gas molecules, even helium [4]. These excellent properties have led to countless efforts to improve the properties of deficient materials, namely polymeric systems, through incorporation of these breakthrough nanoplatelets.

To optimally utilize graphene as a filler in a polymer composite, it is desired for the individual sheets to remain separated and dispersed in the polymer matrix. Three primary mixing techniques, or combinations, are typically utilized in an effort to realize this feat, all with their advantages and drawbacks. These blending techniques include *in situ* polymerization, solution compounding, and melt blending. *In situ* polymerization has proven quite efficient in dispersing graphitic platelets in a polymer matrix and has been shown to produce materials with better mechanical properties, lower percolation thresholds, than the other techniques; however, the process requires substantial energy resources which limit its industrial practicality. Solution compounding has been shown to result in composites with low electrical conduction percolation thresholds; however, industrial implementation is limited by the large amount of potentially environmentally unfriendly solvents that must be used and removed during the process. Melt blending is

industry's mixing method of choice as it has been shown to be both cost effective from an energy consumption standpoint and less harmful to the environment. Unfortunately, the percolation thresholds attained from melt blending are typically higher than from the other techniques [1]. Various other niche techniques have been utilized in combination with these before mentioned mixing methods to further increase graphitic platelet dispersions including both particulate [5] and polymer functionalization [6] and the use of compatibilizers [7].

Of particular interest to this research, incorporation of graphene has enabled gas barrier performance similar to that of clay inclusion in some polymer nanocomposites, but at much lower loadings [5]. However, optimal graphene dispersion can be quite difficult to achieve [8], commonly leading to lower than expected barrier property enhancement, attributed to subpar dispersions consisting of heterogeneous composites with agglomerates. This compromise in graphene dispersion can be more than made up for in the ability to create easily scalable composites without polymer or particle modifications and utilize loadings in a range that would be unprocessable for most nanoclays.

In this study, the GNP particles are dispersed in pure linear low density polyethylene (LLDPE). LLDPE is a rapidly growing commodity plastic used for a variety of applications due to its balance of rigidity and strength along with its ease of processing as compared to other polyethylenes. Even though LLDPE is so prevalent and commercially utilized, the available research on LLDPE/graphene nanoplatelet properties is quite limited [9]. Therefore, the mechanical, thermal, and barrier properties of these

composites were thoroughly analyzed and compared to other relevant systems in the literature.

Lastly, in this study an attempt was made to continue and improve on our previous investigation (Chapter III) which employed coextruded multilayer films consisting of alternating low density polyethylene (LDPE) and maleic anhydride grafted linear low density polyethylene (LLDPE-g-MA)/modified montmorillonite organoclay nanocomposites [10]. Through careful polymer resin choice and a short post-processing annealing step, interlayer interdiffusion could be harnessed to increase the gas barrier properties of the composite films (moving boundary phenomenon). In this research, the modified LLDPE and clay composites were substituted with our easily processable pure LLDPE and unmodified graphene nanoplatelet composites in the filled layers. The high aspect ratios of the graphene nanoplatelets and the ability to disperse large volumes of fillers with minimal viscosity increases were the main impetus for this research. Our modeling in our previous work showed that exceptionally high barrier could be achieved through increasing either or both of these parameters.

The moving boundary phenomenon/ particle concentration effect is briefly explained as follows. If a system of alternating layers of polymers of highly different mobilities is taken into the melt, convective flow (moving boundary) of the more slowly diffusing material can be observed opposite to the fast diffusing molecules in order to relax the sudden increase in density from the diffusion of the more mobile molecules into the sluggish polymer phase [10-16]. If the more mobile polymer phase is blended with high aspect ratio platelets, gas barrier improvement can be observed through the depletion of the polymer layer and concentration of the platelets parallel to the film

surface, thus creating a highly torturous pathway for diffusing gas molecules [10]. This particle concentration brought on through imbedding particulates in the more mobile polymer phase (LLDPE) allows for nanocomposite concentrations in the shrunken LLDPE layers that would not be possible to reach from any other melt processing technique. Nanocomposites typically increase in viscosity with filler concentration, thus high content composites which are beneficial for gas barrier improvements are typically difficult to process.

Experimental

Materials

Graphene composites included the use of short stacks of graphene sheets (xGnP®) from XG Sciences. The particles have an average thickness of approximately 6-8 nanometers, a typical surface area of 120-150 m^2/g, and density of 2.2 g/cm^3. Composites of 25xGnP and 5xGnP with an average particle diameter of 25 and 5 μm respectively were each melt blended in an unmodified LLDPE (Dowlex™ 2035) matrix (MFI 6 g/10 min @190°C, 2.16 kg). Melt blended composites were alternated with Marflex 4517 LDPE (MFI 5 g/10 min @190°C, 2.16 kg) in the multilayer systems analyzed. Addition of xGnP did not substantially alter the melt viscosity of the nanocomposites as they remained processable up to much higher loadings than were previously experienced with clays.

Melt processing

The nanoparticles and the LLDPE were dried for a minimum of 24 h in a vacuum oven at 80°C and were cooled to room temperature under vacuum prior to melt processing. Nanocomposites were melt compounded in a Prism TSE 16TC twin screw extruder using a barrel temperature of 200 °C, a screw speed of ~70 rpm, and maximal feed rate to generate kilogram quantities of pellets. The extruder was blanketed in nitrogen gas to prevent water uptake. The extrudate was cooled in an ice water bath, pelletized, and dried at 80°C under vacuum for 2 hours, then reintroduced to the hopper and extruded again under the same conditions. Film specimens for characterization were generated by compression molding in a Carver melt press at 200 °C and ~3,000 psi. A Dynisco Model D4001 melt flow indexer was used for viscosity estimations where the viscosity is calculated as the shear stress at the well divided by the shear rate at the wall. This viscosity matching of polymers is critical for successful multilayer coextrusion.

Microlayering

Microlayer films comprised of alternating LDPE and LLDPE nanocomposites layers (exterior film layers of LDPE) were extruded in a 1:1 feed ratio using the microlayer coextrusion system at Case Western Reserve University. The LDPE resin was chosen to prevent viscosity mismatch with the nanocomposites during processing which can cause layer breakage or encapsulation. Multilayer films (2-3 kg of material) were coextruded in an extruder that consists of ¾ inch single screw extruders with melt pumps, a coextrusion block, a series of layer multiplier elements, and a film die. Films of 17 layers, LDPE as external layers, and ~300 μm thicknesses were prepared. The layer

thicknesses were chosen to enable interdiffusion to reach completion in minutes to hours, so as to avoid polymer degradation that could occur at longer annealing times.

Multilayer annealing

The microlayer films composed of LDPE and nanocomposite were annealed under nitrogen atmosphere in a melt press. Film specimens were annealed in a confining mold specifically fabricated to match the film thickness. Films were carefully cut to fit these molds, in order to prevent distortion of the film dimensions during annealing. A small amount of pressure was applied to the mold for confinement, as no compression on the sample was the objective. A constant nitrogen flow was provided around the melt press to reduce oxidative degradation. After annealing, the films were quenched in ice water, dried, and stored over desiccant.

Characterization

One dimensional X-ray diffraction spectra were collected on a Rigaku Ultima III diffractometer (Cu Kα radiation, λ = 1.542Å) (WAXD) at room temperature. Oxygen barrier of nanocomposite films and controls were measured at 25°C, 0% RH, and 1 atm partial oxygen pressure difference using a commercially manufactured diffusion apparatus OX-TRAN® 2/21 ML (MOCON). This instrument employs a continuous-flow method (ASTM D3985-81 and ASTM F1249-01) with nitrogen as the carrier gas to measure oxygen flux through polymeric films. The oxygen flux *J(t)* was measured. The permeability coefficient *P* was calculated directly from the steady-state flux J_∞ value as follows $P = J_\infty l/\Delta p$. To complement the MOCON method, an alternative method to

measure gas permeation was also utilized. This method is a constant volume, variable pressure (manometric) technique utilizing a custom-built gas permeation device previously described by our group [17] and the literature [18-20]. Permeation measurements for the gases (CO_2 and O_2) were conducted at ~50 psia applied pressure. The permeation cell was maintained at a constant temperature of 23 °C via a recirculating chiller. The film samples were degassed under high vacuum prior to testing.

Thermal property analysis of each of the LLDPE/graphene nanocomposite films were tested using Thermogravimetric Analysis (TGA) (model TA Instruments TGA Q500). TGA was used to monitor the thermal decomposition of the nanocomposites with increasing temperature through sample weight loss. The TGA ramp rate was 10 °C/ minute up to 600 °C. Nitrogen with a flow rate of 10 mL/min was used as the sample gas. A cone calorimeter (Govmark Cone) was used to investigate the fire properties of the LLDPE and nanocomposite blends. The device operates on the principle that the heat released through the combustion of any organic material is directly related to the amount of oxygen used in the combustion process (oxygen depletion calorimeter). Cone calorimeter measurements were performed according to ASTM E 1354 at 50 kW/m^2 incident heat fluxes with an exhaust flow set to 24 L/sec. Samples were compression molded to a size of 3 x 100 x 100 mm^3. The data obtained from cone calorimetery include the time to ignition, peak heat release rate (PHRR), heat of combustion, and mass loss by the samples.

Mechanical testing was conducted utilizing a MTS Insight 10 Electromechanical Testing System according to ASTM D638 with a Type IV sample of thickness of ~ 1mm in multiples. Tests were conducted at a strain rate of 2.6 mm/min (0.1 in/min).

Morphological analysis of the composites was conducted using optical microscopy (OM). For the OM analysis, sections ~ 5 μm thick were microtomed perpendicular to the film surface using a glass knife.

Results and Discussion

xGnP Nanocomposites

WAXD of the graphene nanocomposites confirm that the ultra-thin graphene nanoplatelets were not completely exfoliated into single graphene sheets but are most likely a mixture of aggregates and dispersed graphene stacks **(**Figure 4.1**)**. The peak at $2\Theta \sim 26°$ demonstrates the short stack nature of the nanoparticles through the graphitic peak. Polymer intercalation was not observed in these systems as no noticeable shifts in the graphitic peak with xGnP inclusion were observed. The mixed aggregated nature of the composites is also demonstrated in the sample optical micrographs in Figure 4.2 which depict LLDPE composites containing 1 and 10 wt% 5xGnP platelets. Aggregates of many micrometers in length and thicknesses are clearly visible in the micrographs.

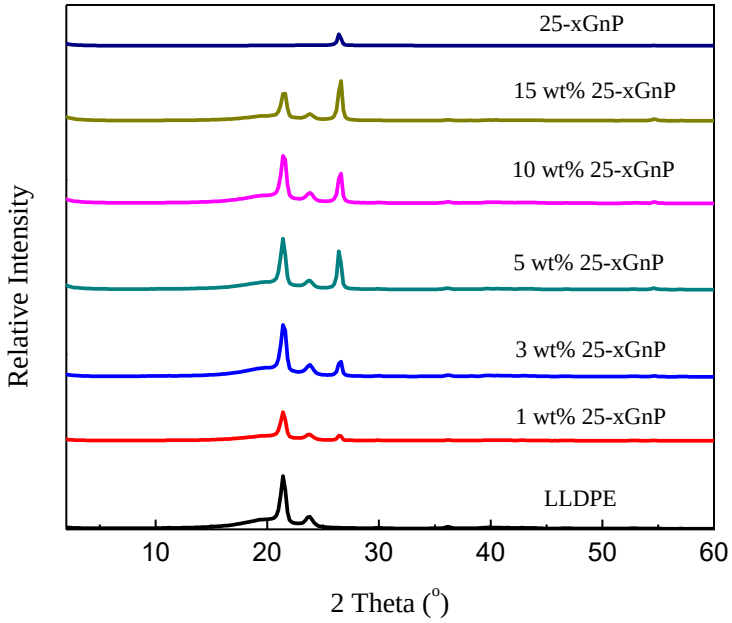

Figure 4.1 WAXD of bulk 25-xGnP, pure LLDPE, and 25-xGnP nanocomposites. WAXD of 5-xGnP showed similar results.

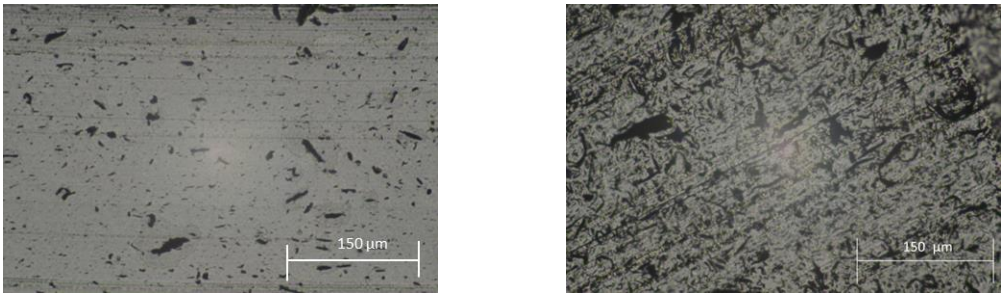

Figure 4.2 Optical micrographs of 1 and 10 wt% 5xGnP in LLDPE.

Thermal analysis of the graphene nanoplatelets by TGA confirms the particle loadings through residual char (graphene nanoplatelets are significantly more thermally stable than the LLDPE matrix) and shows the effect the xGnP particles have on the overall composite thermal stability. A tradeoff in thermal stability effects, from the particles' increased thermal stability and ability to block diffusion of gas combustibles [21] along with an increase in the thermal conductivity of the graphene, is most likely

observed. The net result is a slightly lower onset of degradation (~20°C) for most of the nanocomposites. This lowering of the onset of degradation temperature is not typical, as most graphitic particles tend to impart some thermal stability on a polymer matrix [22], but not unique. This trend has been previously demonstrated at high loadings of graphitic composites for instance in the polypropylene/ GNPs composites analyzed by Liang et al [23]. The slower decomposition rate of the composites as compared to the pure polymer has been attributed to the restricted chain mobility of the polymer near the graphene surface [4]. These trends are shown in Figure 4.3 for the 5xGnP nanocomposites; however, the 25xGnP composites showed very similar results coinciding with the observations of Drzal et al. for a series of xGnP/HDPE composites [24].

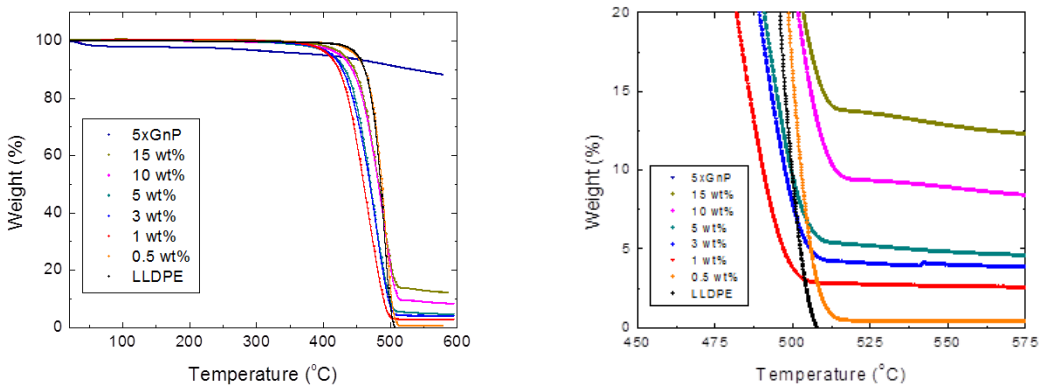

Figure 4.3 TGA thermal stability analysis of bulk 5xGnP, pure LLDPE, and 5xGnP nanocomposites.

Fire property analysis of the graphene nanocomposites were conducted at multiple concentrations. These tests were performed to determine the effect of the graphene addition and particle concentration from interdiffusion has on fire barrier properties. Previously multilayered systems of alternating LDPE and LLDPE-g-MA with 5 wt% organically modified synthetic mica showed significant fire retardancy compared to

nanocomposites of increased loadings. A multilayered mica system with only 2.5 wt% (nanocomposite in only half the layers) showed Peak Heat Release Rates, a measure of a fire's intensity, well below that of mica nanocomposites with 5 wt% and consistent with 10 wt% loadings [25].

The xGnP LLDPE composites showed noticeable fire barrier improvement with increases in xGnP loadings (Figures 4.4-4.6). Continuous char residue forms at loadings above 3 wt % (Figure 4.7). This resulted in a lowering of the time to ignition and a PHHR reduction by up to 70% at higher loadings. The graphene sheets act as a barrier for the escaping gas combustibles (from polymer degradation) that fuels the fire [21].

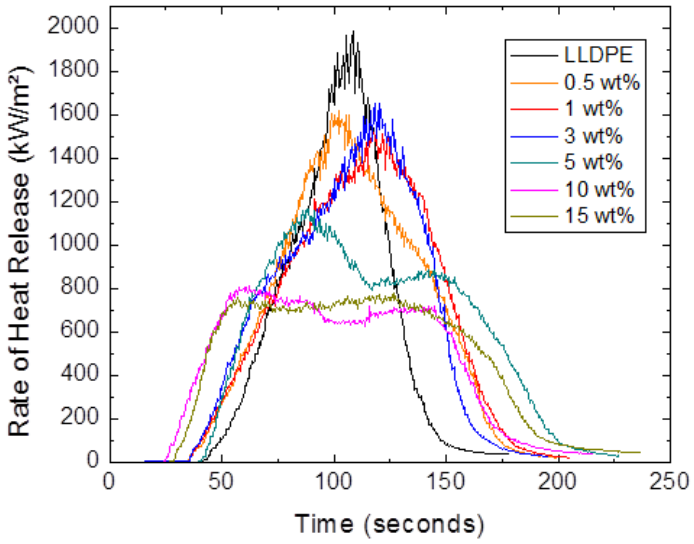

Figure 4.4 PHRR curves for 25xGnP + LLDPE nanocomposites from cone calorimetry

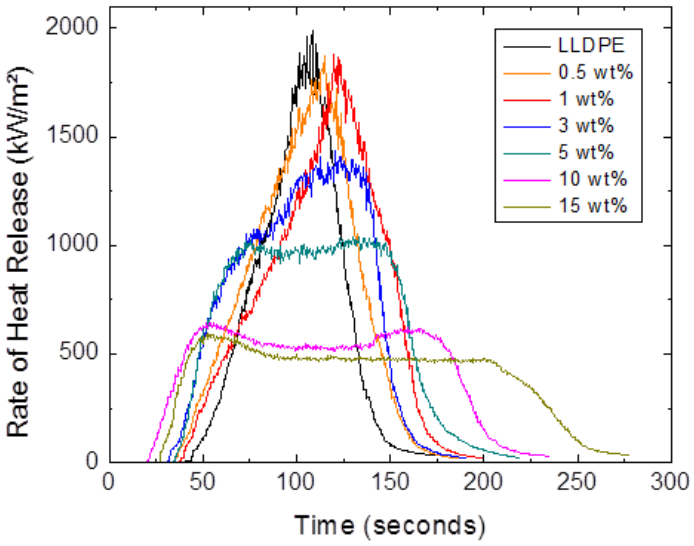

Figure 4.5 PHRR curves for 5xGnP + LLDPE nanocomposites from cone calorimetry

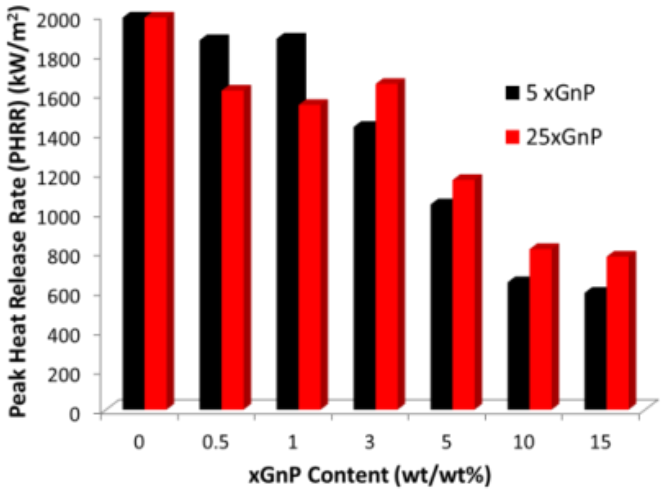

Figure 4.6 Comparison of PHRR values for 25xGnP and 5xGnP nanocomposites of different graphene loadings (wt%).

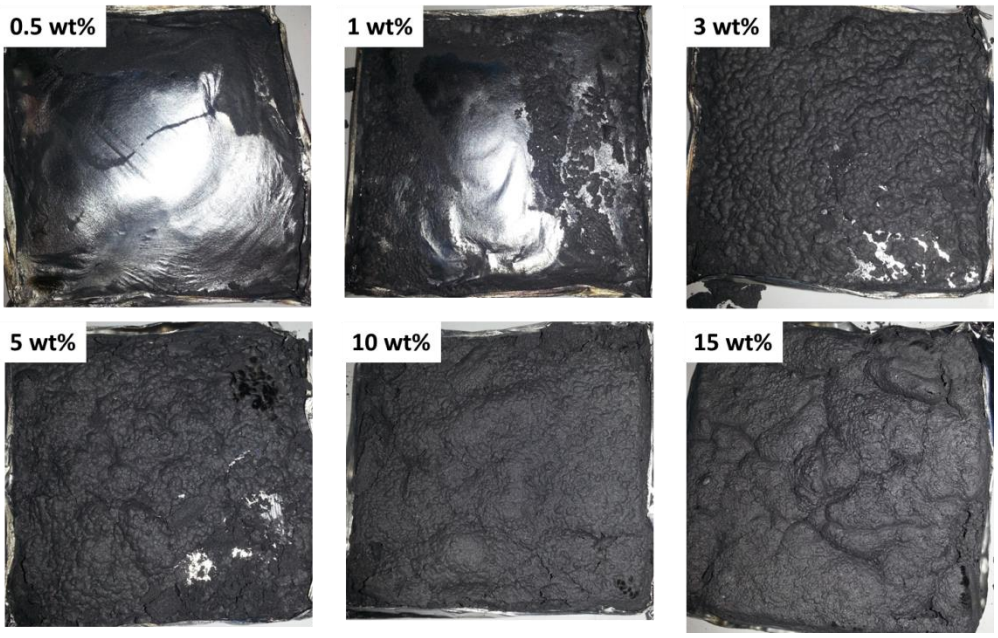

Figure 4.7 Char formation for 5xGnP + LLDPE blends.

Table 4.1 Fire property data from cone calorimetry for 25xGnP + LLDPE composites. Data includes the total heat released, average mass loss rate, peak heat release rate (PHRR), percent reduction of PHRR, time of ignition (t_{ign}), and average effective heat of combustion.

25xGnP	Total Heat Released	Avg Mass Loss Rate	PHRR	Percent Reduction of PHRR	t_{ign}	Avg Eff Heat of Combustion
wt%	MJ/m^2	g/m^2s	kW/m^2	%	s	MJ/kg
0	92.1	28.4	1989	n/a	47.2	47.6
0.5	115.8	16.1	1618	18.6	35.0	40.2
1	118.6	24.9	1546	22.3	36.8	48.6
3	115.9	25.4	1652	16.9	36.9	48.7
5	115.1	19.3	1165	41.4	43.6	47.1
10	91.0	15.2	814	59.1	29.4	46.9
15	99.3	15.3	776	61.0	33.8	46.7

Table 4.2 Fire property data from cone calorimetry for 5xGnP + LLDPE composites.

5xGnP	Total Heat Released	Avg Mass Loss Rate	PHRR	Percent Reduction of PHRR	t_{ign}	Avg Eff Heat of Combustion
wt%	MJ/m^2	g/m^2s	kW/m^2	%	s	MJ/kg
0	92.1	28.4	1989	n/a	47.2	47.6
0.5	113.4	27.4	1874	5.76	36.9	49.4

1	120.7	25.4	1882	5.37	41.1	49.3
3	118.1	24.8	1434	27.8	32.6	48.9
5	116.5	20.6	1041	47.6	34.6	48.1
10	93.2	12.1	646	67.5	20.2	47.0
15	99.5	10.4	593	70.2	28.3	47.0

Mechanical properties of the composites were also analyzed through tensile testing of the composites. As expected the inclusion of the graphene nanoplatelets in the polymer matrix imparted significant tensile modulus and strength increases on the system. With just 5 wt% 5xGnP, the tensile modulus is increased by almost 300%. The stiffness of the graphene systems can also be observed as the higher loading composites fractured at much lower strains. Table 4.3 attempts to compare these results with some other systems found in the literature.

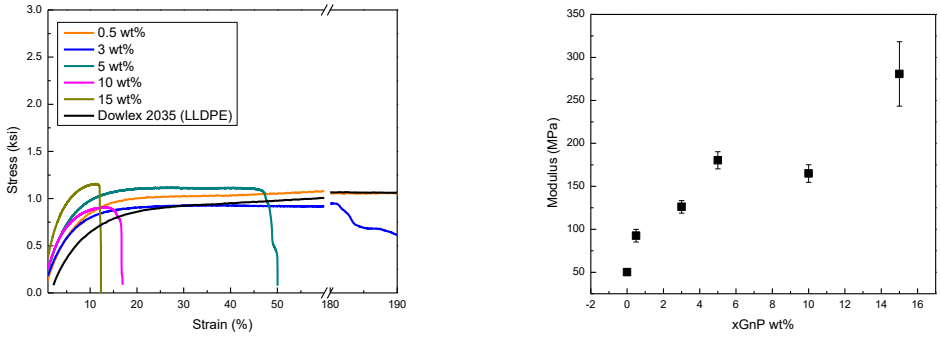

Figure 4.8 Tensile tests of for 5xGnP composites.

Table 4.3 Relevant mechanical property improvements of polymer systems through incorporation of graphene like particles.

Polymer matrix	Filler	Filler loading	Processing	Tensile Modulus Increase (%)	Reference
IMPP + PP-g-MA	5xGnP	8 wt%	melt	34	[7]
TPU	CRG	1 wt%	sol	120	[26]
Epoxy	TEG	0.1 wt%	In situ	31	[27]
Silicone Foam	TEG	.25 wt%	In situ	200	[28]
LLDPE	TRG	3 wt%	sol	147	[6]

LLDPE	TRG	3 wt%	melt	81	[6]
HDPE	GNP	7.5 wt%	melt	160	[24]
HDPE	EG	3 wt%	melt	16.8	[29]
HDPE	EG	10 wt%	melt	~26	[30]
HDPE	EG	20 wt%	melt	~63	[30]
LLDPE	5xGnP	0.5 wt%	melt	85	This work
LLDPE	5xGnP	5 wt%	melt	259	This work
LLDPE	5xGnP	15 wt%	melt	460	This work

*IMPP=impact modified polypropylene, PP-g-MA= maleic anhydride modified polypropylene, CRG=chemically reduced graphene, TEG=thermally expanded graphite, GNP= graphene nanoplatelets, EG=expanded graphene

Gas transport analysis was also performed on the xGnP-LLDPE blends. Example oxygen transmission curves for samples with film thicknesses of ~1.5 mm can be seen in Figure 4.9a. Gas permeability decreased with xGnP loadings as expected. The relative permeabilities of the graphene platelets of different characteristic diameters can be seen in Figure 4.9b. The trends are quite similar for the two xGnPs which can be attributed to the limited dispersion/ aggregation of the graphene platelets. Table 4.4 attempts to put these results into context with a gas barrier comparison with some other relevant nanoplatelet composites.

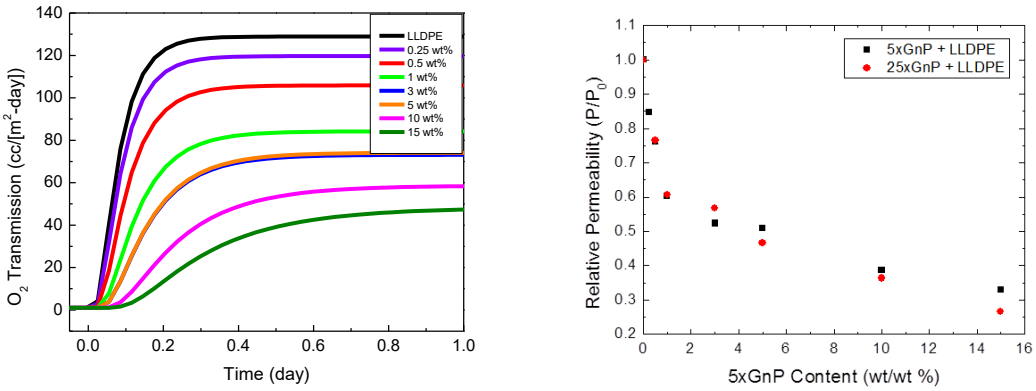

Figure 4.9 (a-left) Oxygen transmission curves for 5xGnP nanocomposites (film thickness ~ 1.5 mm). (b-right) Relative permeabilities of 5xGnP and 25xGnP nanocomposites.

Table 4.4 Gas permeability reduction from literature for comparison

Polymer matrix	Filler	Filler loading	Processing	Gas	Permeability Reduction (%)	Reference
LLDPE	xGnP	1 wt% (0.4 vol%)	Melt	O_2	40	This work
LLDPE	xGnP	5 wt% (2.2 vol%)	Melt	O_2	50	This work
LLDPE	xGnP	15 wt% (6.9 vol%)	Melt	O_2	67	This work
LLDPE-g-MA	MMT	1 vol%	Melt	O_2	42	[16]
LLDPE-g-MA	MMT	4.4 vol%	Melt	O_2	70	[16]
LLDPE	DA-G	1 wt%	Sol	O_2	47	[31]
HDPE	xGnP-M-15	5-7 wt%	melt	O_2	50	[24]
HDPE	DA-GO (RGO)	1 wt%	sol	O_2	67	[32]
PP	xGNP-15	3 vol%	melt	O_2	20	[33]
PP	xGNP-1	3 vol%	melt	O_2	10	[33]
Sty-acrylic	GO	0.7 vol%	sol	O_2	78	[34]
PS	func graphene	0.02 vol%	sol	O_2	20	[5]
PS	func graphene	2.27 vol%	sol	O_2	61	[5]
PET	GNP	1.5 wt%	Melt	O_2	99	[35]
Cellulose	GNP	5 wt%	sol	O_2	27	[36]
PMMA	Graphene	0.5 wt%	In situ	O_2	70	[37]
PAN	EG	4 wt%	In situ	O_2	92	[38]

*DA-GO (DA-G)= dodecyl amine functionalized graphene oxide and dodecyl amine functionalized graphene, RGO= reduced graphene oxide.

To gain further insight on the oxygen gas transport mechanism in the composite systems, the experimental oxygen flux data was fit with a solution to Fick's second law (Equation 4.1). Δp is the oxygen partial pressure difference across the film, 1 atm here, l is the thickness of the film and t is the time. From a two parametric fit the permeability P and diffusivity D were calculated.

$$J_{(t)} = \frac{P\Delta p}{l}\left[1 + 2\sum_{n=1}^{\infty}(-1)^n \exp\left(-\frac{D\pi^2 n^2 t}{l^2}\right)\right] \qquad (4.1)$$

The solubility S was calculated from the relationship $P = D \times S$. The permeability coefficient P was also calculated directly from the steady-state flux J_∞ value as follows: $P = J_\infty l/\Delta P$.

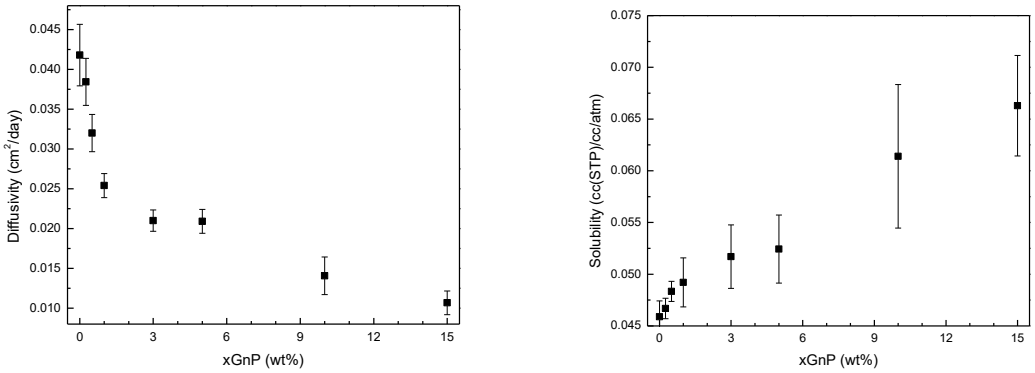

Figure 4.10 Diffusivity (left) and solubility (rights) coefficient plots of 5xGnP/LLDPE composites.

The decrease in diffusivity with increasing xGnP content was expected from the tortuosity models as the gas molecules must circumvent the impermeable platelets; however, the increase in solubility with increasing particle fraction was unexpected. One would expect a decrease in solubility with added filler particles due to the excluded volume occupied by the perceived insolubility of gases in the particles. Decreases in solubility for systems with good polymer-filler interactions are typically described by Equation 4.2 where S_p describes the solubility in the pure polymer and φ the volume fraction of filler. Compton et. al [5] and Guan et. al [34] observed an even more significant decrease in solubility with increases in modified crumpled graphene in polystyrene and graphene oxide in a styrene-acrylic latex, respectively. Compton contributed this decrease in solubility to a densification at the polymer-graphene interface.

$$S = S_p(1 - \varphi) \tag{4.2}$$

An alternative gas transport testing mechanism was thus employed to determine the diffusivity and solubility values. This method is a constant volume, variable pressure

(manometric) technique utilizing a custom-built gas permeation device previously described by our group [17]. The slopes of the increase in pressure vs. time experimental data (Figure 4.11) were determined via a linear fit. Using this slope, permeability values were calculated according to Equation 4.3, where P is the permeability, V_d is the downstream volume, l is the membrane thickness, p is the applied upstream pressure, A is the testing area, R is the universal gas constant, T is the temperature, and dp/dt is the steady-state slope. Diffusion coefficients, D, were then calculated from time lag values, t_L, according to Equation 4.4, where t_L is the intersection of the steady-state line extrapolation to the x-axis. Solubility coefficients, S, were then calculated from known permeability and diffusivity coefficients as follows: $P = DS$. The results are depicted in Table 4.5.

$$\mathrm{P} = \frac{V_d l}{pART}\frac{dp}{dt} \tag{4.3}$$

$$\mathrm{D} = \frac{l^2}{6t_L} \tag{4.4}$$

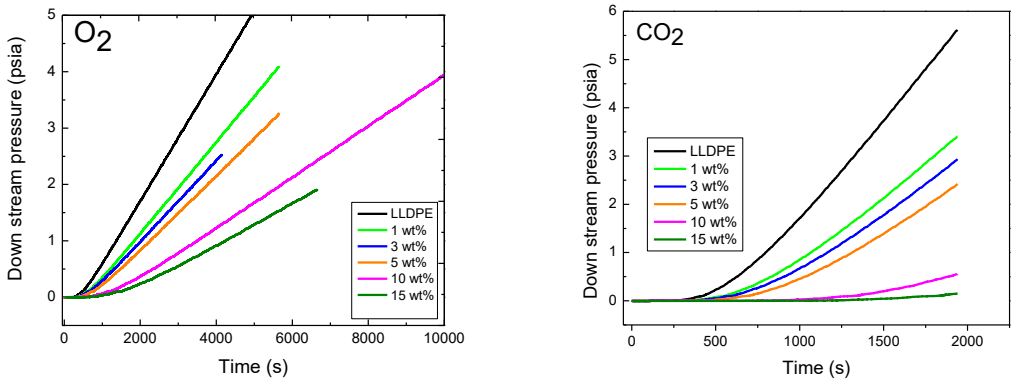

Figure 4.11 CVVP raw data plots for O_2 (left) and CO_2 (right) gas flux through films ~300μm in thickness.

Table 4.5 CVVP oxygen and carbon dioxide gas diffusion results for 5xGnP/LLDPE composites.

		O_2							
5xGnP wt%	5xGnP vol%	P CVVP Barrer	P MOCON Barrer	S CVVP cc(STP)cm^{-3}atm^{-1}	S MOCON cc(STP)cm^{-3}atm^{-1}	D CVVP cm^{2}s^{-1}	D MOCON cm^{2}s^{-1}	Relative P CVVP P/ P_0	Relative P MOCON P/ P_0
0	0	2.34	3.16	0.0381	0.0459	4.66E-07	4.84E-07	1.00	1.00
0.25	0.10	1.45	2.67	0.0355	0.0467	3.09E-07	4.45E-07	0.62	0.85
0.5	0.21	1.46	2.40	0.0415	0.0483	2.68E-07	3.70E-07	0.62	0.76
1	0.42	1.46	1.90	0.0423	0.0492	2.62E-07	2.94E-07	0.62	0.60
3	1.28	1.29	1.65	0.0385	0.0517	2.55E-07	2.43E-07	0.55	0.52
5	2.15	1.21	1.61	0.0436	0.0524	2.11E-07	2.42E-07	0.52	0.51
10	4.44	1.04	1.22	0.0447	0.0614	1.77E-07	1.63E-07	0.45	0.39
15	6.87	0.88	1.04	0.0430	0.0663	1.56E-07	1.24E-07	0.38	0.33

		CO_2			
5xGnP wt%	5xGnP vol%	P Barrer	S cc(STP)cm^{-3}atm^{-1}	D cm^{2}s^{-1}	Relative P P/ P_0
0	0	8.79	0.189	3.54E-07	1.00
0.25	0.10	5.92	0.188	2.40E-07	0.67
0.5	0.21	5.91	0.217	2.07E-07	0.67
1	0.42	5.57	0.230	1.84E-07	0.63
3	1.28	4.85	0.204	1.81E-07	0.55
5	2.15	4.96	0.274	1.38E-07	0.56
10	4.44	3.92	0.247	1.21E-07	0.45
15	6.87	3.23	0.268	9.16E-08	0.37

This method also demonstrates a slight increase in solubility with increasing volume fraction of graphene platelets. This leads to a few hypotheses for the origin of this phenomenon that need further investigation. The first is that delamination at the graphene/polymer interface from the unfavorable interactions results in gaps of unoccupied volume, capable of solvating the gas molecules [39]. This seems unlikely as one would not think that these gaps would be large enough to make up for the sheer size of the graphene aggregates. A second hypothesis is that the crystallinity of the system is affected by the incorporation of the graphene nanoplatelets into the system. Hoor et al. noticed this occurance when adding graphene platelets to a super tough polyamide 6 system using SEBS [40]. With only 3 wt% graphene added, the crystallinity droped by ~ 8%. Another explanation is that for some reason the graphene platelets have an affinity

for oxygen and carbon dioxide and adsorb gas molecules on the platelet surface or in the interlayer spacings. Lastly, these models for decoupling the diffusivity and solubility parameters from flux data were not developed for composite systems. They work on the assumption that gas transport through a film follows the diffusion solution model and that solubility follows Henry's law [39]. If the graphene nanoplatelets cause the system to be in a state of disequilibrium, these models may not hold.

These hypotheses are currently being tested. A more through morphological exampination of the composites utilizing transmission electron microscopy should shed light on the particle dispersion state, i.e. if the systems are in fact mixtures of exfoliated and aggregated particles. It may also be able to observe delamination at the particle surface. If not, a thorough density analysis or free volume analysis is also possible. The crystallinity is currently being tested with DSC. A drop in crystallinity could definitely account for an increase in solubility as there would be more volume for the gases to solvate. Finnaly, direct sorption measurements are also being conducted to confirm that this solubility trend is indeed a reality and not a problem with the models utilized to extract the diffusion coefficient parameters.

Multilayers

One of the factors in choosing the graphene platelets for nanocomposite formation was the larger processability window available for multilayer coextrusion. This increased processability window for loadings of 25xGnP graphene nanoplatelets can be seen in Figure 4.12. This allowed for successful multilayer coextrusion of LLDPE/xGnP composites with loadings as high as 10 wt%.

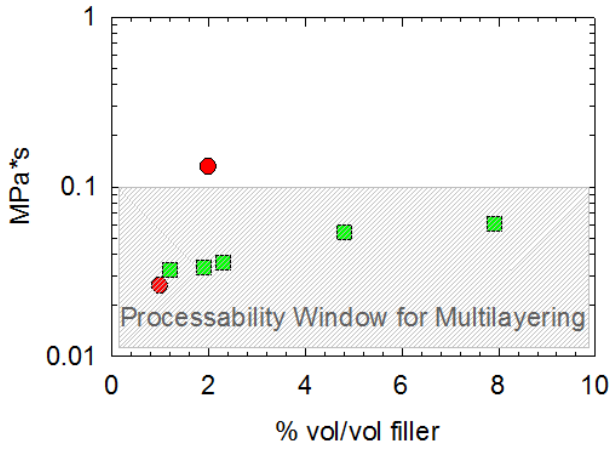

Figure 4.12 MFI viscosity data for 5xGnP graphene nanocomposites (■) compared to montmorillonite nanocomposites (●) Note availability of high volume fractions.

The multilayers chosen for analysis in this study contain 1 wt% and 10 wt% 5xGnP in the filled LLDPE layers alternated with unfilled LDPE layers. The effect of particle concentration from interdiffusion on the layers sizes (Figure 4.13) and gas transport properties can be seen in Figure 4.14 for a 17 layered LLDPE/LDPE multilayered system with 1 (Figure 4.13/ Figure 4.14a) and 10 wt% (Figure 4.14b) 5xGnP in the LLDPE layers before and after annealing at 200 °C. Particle concentration imparts a limited decrease in permeability as compared to the as received multilayer films. However, the permeability values of the annealed samples do reflect values of nanocomposites with higher loadings as predicted by the series model (dashed lines).

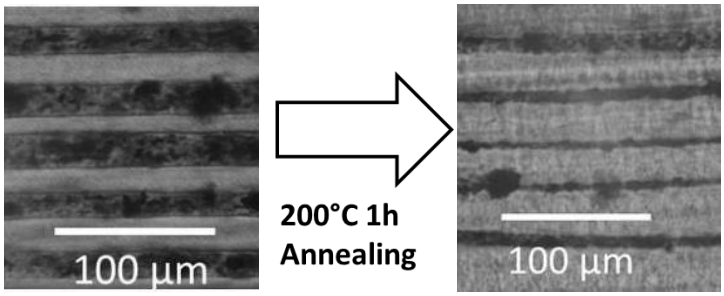

Figure 4.13 Optical micrograph of internal layers of 17 layer coextruded multilayer film with alternating layers of 1 wt% 5xGnP + LLDPE composite and unfilled LDPE layers before (left) and after (right) annealing (interdiffusion) for 1h at 200°C.

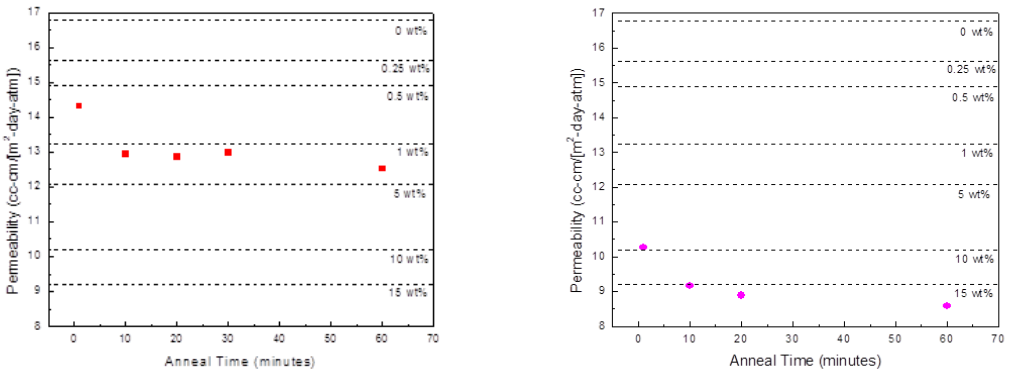

Figure 4.14 Effect of interdiffusion/ particle concentration on gas barrier. (■) 17 layered multilayered LLDPE + 1 wt% 5xGnP/ LDPE and (●) 10 wt% 5xGnP/ LDPE films (wt% graphene in initial filled layers) before and after annealing at 200 °C. The dashed lines predict the initial permeability of identical multilayer composites with different xGnP loadings.

Conclusions

Gas and fire barrier, mechanical, and thermal property enhancement of flexible polyethylene/ short stack graphene nanoplatelet (xGnP) composite systems were thoroughly analyzed in bulk composites and expanded to coextruded multilayers films. Through incorporation of the xGnP platelets, with their impermeable high aspect ratios, in LLDPE, substantial increases in gas and fire barrier along with mechanical strength were observed. The graphene composites outperformed our previously investigated organoclay composites without the need for extra particle and polymer modification steps to promote dispersion. I.e., the oxygen/carbon dioxide permeability of the LLDPE system was halved with the addition of only 2 vol% xGnP while the tensile modulus increased almost three fold. The analyzed composites were also formulated into microlayer systems consisting of alternating linear low density polyethylene (LLDPE)/xGnP composites and

pure low density polyethylene (LDPE) layers as a continuation of our studies exploiting the moving boundary phenomenon for further gas barrier enhancement. Composite layer shrinkage was confirmed through optical microscopy and resulted in a decrease in permeability for the coextruded films that reflected the barrier properties of composites multilayers with ~3-5 wt% more graphene nanoplatelets. While this data proved interesting, the desirable very high barrier was unachieved because of the dispersion state of the graphene platelets. A better processing technique will thus have to be discovered/ utilized for this to realize this goal.

Acknowledgements

The authors are grateful to the National Science Foundation for support of this work through the Center for Layered Polymeric Systems (DMR 0423914) and the GK-12 fellowship program (DGE-1007911, Award #0947944). Special thanks are to be given to the Dr. Baer and his coextrusion team at Case Western Reserve University for their careful manufacturing of the multilayered films.

References

1] Sengupta R, Bhattacharya M, Bandyopadhyay S, Bhowmick AK. A review on the mechanical and electrical properties of graphite and modified graphite reinforced polymer composites. Prog Polym Sci 2011; 36(5): 638-670

2] Kalaitzidou K, Fukushima H, Drzal LT. Mechanical properties and morphological characterization of exfoliated graphite-polypropylene nanocomposites. Compos Part A-Appl S. 2007; 38(7): 1675-1682.

3] Lee C, Wei XD, Kysar JW, Hone J. Measurement of the elastic properties and intrinsic strength of monolayer graphene. Science 2008; 321(5887): 385-388

4] Bunch JS, Verbridge SS, Alden JS, van der Zandle AM, Parpia JM, Craighead HG, McEuen PL. Impermeable Atomic Membranes from Graphene Sheets. Nano Lett. 2008; 8(8): 2458-2462

5] Compton OC, Kim S, Pierre C, Torkelson JM, Nguyen ST. Crumpled Graphene Nanosheets as Highly Effective Barrier Property Enhancers. Adv Mater 2010; 22(42): 4759-4763.

6] Kim H, Kobayashi S, AbdurRahim MA, Zhang MJ, Khusainova A, Hillmyer MA, Abdala AA, Macosko CW. Graphene/polyethylene nanocomposites: Effect of polyethylene functionalization and blending methods. Polymer 2011; 52(8): 1837-1846

7] Duguay A, Nader JW, Kiziltas A, Gardner DJ, Dagher HJ. Exfoliated graphite nanoplatelet-filled impact modified polypropylene nanocomposites: influence of particle diameter, filler loading, and coupling agent on the mechanical properties. Appl Nanosci 2014; 4(3): 279-291.

8] Khanam PN, AlMaadeed MA, Ouederni M, Harkin-Jones E, Mayoral B, Hamilton A, Sun D. Melt processing and properties of linear low density polyethylene-graphene nanoplatelet composites. Vacuum 2016; 130: 63-71.

9] Tripathi SN, Rao GSS, Mathur AB, Jasra R. Polyolefin/graphene nanocomposites: a review. RSC Adv 2017; 7: 23615-23632.

10] Decker J, Meyers KP, Paul DR, Schiraldi DA, Hiltner A. Polyethylene-based nanocomposites containing organoclay: A new approach to enhance gas barrier via multilayer coextrusion and interdiffusion. Polymer 2015; 61(20): 42-54.

11] Green PF, Palmstrom CJ, Mayer JW, Kramer EJ. Marker Displacement Measurements of Polymer-Polymer Interdiffusion. Macromolecules 1985; 18(3): 501-507.

12] Kramer EJ, Green P, Palmstrom CJ. Interdiffusion and Marker Movements in Concentrated Polymer-Polymer Diffusion Couples. Polymer 1984; 25(4): 473-480.

13] Nazarenko S, Dennison M, Schuman T, Stepanov EV, Hiltner A, Baer E. Creating Layers of Concentrated Inorganic Particles by Interdiffusion of Polyethylenes in Microlayers. J Appl Polym Sci 1999; 73(14): 2877-2885.

14] Pollock G, Nazarenko S, Hiltner A, Baer E. Interdiffusion in Microlayered Polymer Composites of Polycarbonate and a Copolyester. J App Polym Sci 1994; 52(2): 163-176.

15] Schuman T, Stepanov EV, Nazarenko S, Capaccio G, Hiltner A, Baer E. Interdiffusion of Linear and Branched Polyethylene in Microlayers Studied via Melting Behavior. Macromolecules 1998; 31(14): 4551-4561.

16] Schuman T, Nazarenko S, Stepanov EV, Magonov SN, Hiltner A, Baer E. Solid State Structure and Melting Behavior of Interdiffused Polyethylenes in Microlayers. Polymer 1999; 40(26): 7373-7385.

17] Kwisnek L, Heinz S, Wiggins JS, Nazarenko S. Multifunctional thiols as additives in UV-cured PEG-diacrylate membranes for CO_2 separation. J Membr Sci 2011; 369(1-2): 429-436.

18] Bondar VI, Freeman BD, Pinnau I. Gas transport properties of poly(ether-b-amide) segmented block copolymers. J Polym Sci, Part B: Polym Phys 2000; 38(15): 2051-2062.

19] Lin H, Freeman BD. Gas solubility, diffusivity and permeability in poly(ethylene oxide). J. Membr Sci 2004; 239(1): 105-117.

20] Lin H, Kai T, Freeman BD, Kalakkunnath S, Kalika DS. The Effect of Cross-Linking on Gas Permeability in Cross-Linked Poly(Ethylene Glycol Diacrylate). Macromolecules 2005; 38(20): 8381-8393.

21] Kashiwagi T, Du F, Douglas JF, Winey KI, Harris RH, Shields, JR. Nanoparticle networks reduce the flammability of polymer nanocomposites. Nature Mater 2005; 4(12): 928-933.

22] Verdejo R, Bernal MM, Romasanta LJ, Lopez-Manchado MA. Graphene filled polymer nanocomposites. J Mater Chem 2011; 21(10): 3301-3310.

23] Liang JZ, Wang JZ, Tsui GCP, Tang CY. Thermal properties and thermal stability of polypropylene composites filled with graphene nanoplatelets. J Thermoplast Compos 2017; 1-19

24] Vautard F, Honaker-Schroeder T, Drzal LT, Sui L. High Density Polyethylene-Exfoliated Graphene Nanoplatelet Nanocomposites for Automotive Fuel Line and Fuel Tanks Applications. Polym Bull 2013; 70: 939-951.

25] Wu, Y. 2013 Nanoparticle Filled Polymeric Systems for Gas Barrier and Flame Retardant Properties (Doctoral dissertation). Retrieved from AQUILA.

26] Liang JJ, Xu YF, Huang Y, Zhang L, Wang Y, Ma YF, Li FF, Guo TY, Chen YS. Infrared-Triggered Actuators from Graphene-Based Nanocomposites. J Phys Chem C 2009; 113(22): 9921-9927.

27] Rafiee MA, Rafiee J, Wang Z, Song H, Yu ZZ, Koratkar N. Enhanced Mechanical Properties of Nanocomposites at Low Graphene Content. ACS Nano 2009; 3(12): 3884-3890.

28] Verdejo R, Barroso-Bujans F, Rodriguez-PerezMA, de Saja JA, Lopez-Manchado. Functionalized graphene sheet filled silicone foam nanocomposites. J Mater Chem 2008; 18(19): 2221-2226.

29] Zheng W, Lu X, Wong S. Electrical and Mechanical Properties of Expanded Graphite-Reinforced High-Density Polyethylene. J Appl Poly Sci 2004; 91(5): 2781-2788

30] Li Y, Chen G. HDPE/Expanded Graphite Nanocomposites Prepared via Masterbatch Process. Polym Eng Sci 2007; 47(6): 882-888.

31] Kuila T, Bose S, Mishra AK, Khanra P, Kim NH, Lee JH. Effect of functionalized graphene on the physical properties of linear low density polyethylene nanocomposites. Polym Test 2012; 31(1): 31-38.

32] Ren PG, Wang H, Huang HD, Yan DX, Li ZM. Characterization and performance of dodecyl amine functionalized graphene oxide and dodecyl amine functionalized graphene/high-density polyethylene nanocomposites. J Appl Polym Sci 2014; 131(2): 39803

33] Kalaitzidou K, Fukushima H, Drzal LT. Multifunctional polypropylene composites produced by incorporation of exfoliated graphite nanoplatelets. Carbon 2007; 45(7): 1446-1452

34] Guan Y, Meyers KP, Mendon SK, Hao G, Douglas JR, Trigwell S, Nazarenko SI, Patton DL, Rawlins JW. Ecofriendly Fabrication of Modified Graphene Oxide Latex Nanocomposites with High Oxygen Barrier Performance. Appl Mater Interfaces 2016; 8(48): 33210-33220.

35] Al-Jabareen A, Al-Bustami H, Harel H, Marom G. Improving the oxygen barrier properties of polyethylene terephthalate by graphite nanoplatelets. J Appl Polym Sci 2013; 128(3): 1534-1539.

36] Mahmoudian S, Wahit MU, Imran M, Ismail A, Balakrishnan H. A facile approach to prepare regenerated cellulose/graphene nanoplatelets nanocomposite using room-temperature ionic liquid. J Nanosci Nanotechnol 2012; 12(7):5233-5239.

37] Chang KC, Ji WF, Lai MC, Hsiao YR, Hsu CH, Chuang TL, Wei Y, Yeh JM, Liu WR. Synergistic effects of hydrophobicity and gas barrier properties on the anticorrosion property of PMMA nanocomposite coatings embedded with graphene nanosheets. Polym Chem 2014; 5(3): 1049-1056.

38] Prusty G, Swain SK. Synthesis and characterization of conducting gas barrier polyacrylonitrile/graphite nanocomposites. Polym Compos 2011; 32(9):1336-1342.

39] Cui Y, Kundalwal SI, Kumar S. Gas barrier performance of graphene/polymer nanocomposites. Carbon 2016; 98: 313-333

40] Hoor FA, Morshedian J, Ahmadi S, Rakhshanfar M, Bahramzadeh A. Effect of Graphene Nanosheets on the Morphology, Crystallinity, and Thermal and Electrical

Properties of Super Tough Polyamide 6 Using SEBS Compounds. J Chem-NY 2015; 2015.

CHAPTER V – PROBING THE CONFINING EFFECT OF CLAY PARTICLES ON AN AMORPHOUS INTERCALATED DENDRITIC POLYESTER

This chapter was co-authored with Jeremy J Decker, Brian G Olson, Jun Lin, Alexander M Jamieson, and Sergei Nazarenko

Abstract

The fourth generation of a hydroxylated dendritic hyperbranched polyester (HBP) was combined with sodium montmorillonite clay (Na^+MMT) using water to generate a broad range of polymer clay nanocomposites from 0 to 100% wt/wt Na^+MMT. Analysis with differential scanning calorimetry (DSC) showed a deviation in heat capacity, ΔC_p, with clay content at the T_g from a two-phase trend which was attributed to the formation of an immobilized rigid amorphous fraction (RAF) in the interlayer spacing of the intercalated system. This deviation occurred in a step-like fashion which we attributed to 0.5 nm incremental changes in the interlayer spacing, previously observed through X-ray diffraction analysis. A simple series model was utilized to quantify these interlayer spacings based on the ΔC_p values and showed good correspondence with the X-ray results. The RAF was quantified from changes in heat capacity with clay content and was verified by an alternative novel positron annihilation lifetime spectroscopy (PALS) approach. The PALS quantification of the RAF was possible through an analysis of changes in the hole size thermal expansivity of the nanocomposites as a function of clay composition. Results indicated that as much as 32% by weight of the system is made up of the RAF at its maximum.

Introduction

Polymer clay nanocomposites often exhibit chemical and physical properties that are superior to those of conventional composite materials [1-3]. The morphology of these nanocomposites can generally be classified as phase separated, intercalated, disordered intercalated, or exfoliated, depending on the interactions between the nanoclay and the polymer as well as the processing conditions [1-3]. To promote dispersion in a polymer matrix, layered silicates such as sodium montmorillonite (Na^+MMT) typically require modification by surfactants to increase the organophilicity of the clay surfaces.

Various water-soluble linear polymers, such as poly(ethylene oxide) (PEO), poly(vinyl alcohol) (PVA), and poly(vinylpyrrolidinone) (PVP), have successfully been intercalated into unmodified Na^+MMT clay galleries by aqueous solution casting methodologies [1-2]. However, the high viscosities of these systems can require shear intensive processing procedures, especially at high clay contents [4]. Hyperbranched polymers (HBPs) possess lower solution viscosities than linear polymers due to their more compact globular structures [5], which facilitate solution processing, even at high clay concentrations, without shear intensive procedures.

Due to their facile synthesis [6-9], dendritic hyperbranched polyester polyols (also known as Boltorn^{TM} dendritic polyols) based on 2,2-bis-methylopropionic acid (bis-MPA) with an ethoxylated pentaerythritol core are popular model systems which preserve the essential features of dendrimers, namely high end-group functionality and a globular architecture, but possess imperfect branching and large polydispersities [5-16]. These HBPs are hydrophilic due to the presence of branch-terminal hydroxylated end groups [17], and hence are compatible with clay gallery surfaces. Experimental [18-22] and theoretical [23] studies indicate that a high interaction strength between the end

functional groups of the dendritic polymers and a substrate leads to the collapse and flattening of the globular dendritic structure on the substrate.

The incorporation of polymer into clay galleries exposes numerous interfaces to the polymer matrix and the resulting polymer-substrate interactions can be probed by bulk techniques. Månson et al. [24-27] explored the structure of intercalated nanocomposite films based on surfactant-free Na^+MMT clays mixed with second, third, and fourth pseudogeneration Boltorn™ dendritic polyols. X-ray diffraction (XRD) data demonstrated that, at intermediate Na^+MMT contents, the interlayer spacings of the intercalated nanocomposites correlated closely with estimates of the molecular diameters of the different HBP generations. It was concluded that the HBPs maintained their globular architecture in an intercalated state throughout approximately half of the compositional range. However, at the higher clay contents, the HBPs flattened within the clay galleries, leading to equivalent interlayer spacings for the 2nd, 3rd, and 4th HPB generations.

Subsequently, we carried out a more detailed morphological analysis of the same intercalated nanocomposite system [28], specifically comprising of the 2nd and 4th pseudogenerations of Boltorn dendritic polyols and ecompassing polymer clay nanocomposite compositions from 0 to 95% wt/wt Na^+MMT. Intercalation peaks were observed by powder XRD at and above 15% wt/wt Na^+MMT content for both HBP systems. In fact, intercalation was present at all clay loadings, as evidenced by TEM, but, at lower clay contents, exfoliated and disordered intercalated states were also present. The number of clay layers per intercalated stack increased with increases in Na^+MMT content. The interlayer spacings for the 2nd and 4th pseudogenerations (HBP2 and

HBP4) were observed to decrease in increments of approximately 0.5 nm as the clay content increased. Importantly, the interlayer spacings for the 2nd and 4th generations of HBP were nearly identical at the same clay compositions, indicative that the interlayer spacings were independent of the HBP generation number. The interlayer spacings for both HBP2 and HBP4 decreased with increasing clay content until finally reaching a minimum spacing of 0.5 nm at the highest clay contents. These step-wise changes in interlayer spacings are consistent with the presence of discrete layers of flattened HBP between the clay layers. It was proposed that the HBP adsorbed onto the clay layers in solution and re-aggregated, upon solvent removal, into intercalated stacks of clay and flattened HBP. Recently, layer-by-layer intercalation of flattened Boltorn™ HBPs into Na^+MMT clay galleries was confirmed by Androulaki et al. [29]. Analogous behavior was observed for Na^+MMT clay based nanocomposites with a hyperbranched polyesteramide (Hybrane™) and a polyamidoamine (PAMAM) dendrimer, each prepared via aqueous solution intercalation methodology [30-31]. Therefore, this trend appears to be fairly general for hydrophilic dendritic systems.

The confinement of collapsed HBP between multiple clay layers is expected to result in a sizable amount of immobilized polymer. The nature of this immobilized polymer is viewed as analogous to the concept of a rigid amorphous fraction (RAF) in semi-crystalline polymers, introduced to explain an observed discrepancy between the degree of crystallinity and the change in heat capacity, ΔC_p, at the glass transition, T_g [32]. In simplest terms, RAF represents the fraction of the amorphous phase that does not contribute to the change in ΔC_p at either the T_g or T_m (melting). It is well-established [32-44] that the RAF is due to an immobilization of the disordered polymer chains that

connect the crystalline lamellae. These chains are unable to undergo long range translational motions when crystalline constraints are imposed during crystallization of the polymer melt, implying that the RAF vitrifies in the vicinity of the crystallization temperature, T_c. In contrast, the un-constrained amorphous chains, the mobile amorphous fraction (MAF), remain in the molten state at T_c and vitrify upon cooling at the regular T_g. Complete devitrification of RAF occurs at T_m.

It is also established that the immobilized amorphous phase in nanocomposites exhibits some of the characteristics of a RAF, such as the suppression of the glass transition [45-48]. The majority of recent research on RAF at the particle interface has involved SiO_2 nanocomposites that utilize ΔC_p analysis at the T_g to measure the amount of RAF [49-54] and has focused on semicrystalline polymer nanocomposite systems [55-61].

Unlike crystalline phases, however, inorganic clay does not melt within the thermal stability range of the polymers. This means that, if the interactions between polymer and inorganic substrate are maintained at elevated temperatures, devitrification of the immobilized chains does not occur [45]. Indeed, this was demonstrated in a study of the dynamics of an amorphous hyperbranched polyesteramide intercalated in Na^+MMT layers via quasi elastic-neutron scattering [62]. It was observed that the polymer chains confined within the clay galleries exhibit dynamical behavior above the bulk T_g similar to that of the bulk polymer below the T_g. The HBP dynamics were frozen due to the clay nanoconfinement, consistent with observed decreases in ΔC_p at the T_g [62].

In the current paper we study the behavior of the immobilized RAF in surfactant-free Na^+MMT clay nanocomposites generated using the 4th generation of a Boltorn™ dendritic polyol over a very broad range of compositions (0-100% wt/wt). Since the Na^+MMT exhibits no thermal transitions within the investigated temperature ranges, it is ideally suited to investigate polymer immobilization solely at the clay interfaces. Heat capacity measurements were used to quantify the amount of RAF as described by Wunderlich et al. for semicrystalline polymers [32]. We demonstrate that the heat capacity behavior shows a strong correlation with the earlier observed step-like behavior of interlayer spacing in these intercalated nanocomposites [28-29]. To probe the structure of the RAF, free volume measurements using positron annihilation life-time spectroscopy (PALS) were employed.

PALS is a well-established, quantitative probe for free volume in polymeric materials [63-64]. In a PALS experiment, high energy positrons are injected from a radiation source into a polymer sample. The positrons thermalize via collisions with atoms and either annihilate or form a hydrogen-like pair with a secondary electron created via collision-induced ionization. In polymers, the more stable pair system, called an ortho-positronium (o-Ps), tends to localize in regions of low density, i.e. holes. Annihilation of such localized o-Ps occurs via a pickoff mechanism in which the o-Ps positron annihilates with an electron of the medium with an opposite spin. Quantitative comparisons have been established between the characteristic parameters, obtained via PALS, viz. the intensity, I_3, and lifetime, τ_3, of the o-Ps annihilation component, and the fractional free volume, f_v, of amorphous polymers, as computed by statistical mechanical theory [65-66]. The o-Ps intensity, I_3, is typically regarded as a measure of the number

density of the free volume holes. The o-Ps lifetime, τ_3, can be related to a spherical hole radius, *R*, via the Tao-Eldrup equation, which is based on quantum mechanical and empirical arguments [67-68] as follows:

$$\tau_3 = 0.5\ (ns)\left[1 - \frac{R}{R_0} + \frac{1}{2\pi} sin\left(\frac{2\pi R}{R_0}\right)\right]^{-1} \qquad (1)$$

where *R* is the hole radius in Å. R_0 equals $R + \Delta R$ where ΔR is a fitted empirical electron layer thickness of 1.66 Å. From *R*, the average hole free volume $v_h = (4\pi/3)R^3$ may be calculated. It follows that f_v is proportional to the product $I_3 v_h$.

As mineral silicate layers are too dense for o-Ps species to form, PALS is only sensitive to the HBP content of the HBP/clay nanocomposites. PALS experiments were used to assess, as a function of clay content, the average free volume hole size below and above the glass transition of the nanocomposites. The broad range of compositions prepared in this study enabled a novel opportunity to examine the free-volume behavior in intercalated polymer/clay nanocomposites. We anticipated that the RAF, which remains in the vitrified state above T_g, and the MAF, which becomes liquid at $T > T_g$, contribute in an additive fashion to the overall hole volume thermal expansion coefficient. Therefore, we looked forward to estimate the amount of RAF in the nanocomposites by PALS, and hence verify the DSC methodology based on the measurements of ΔC_p at the T_g.

Experimental

Materials and Sample Preparation

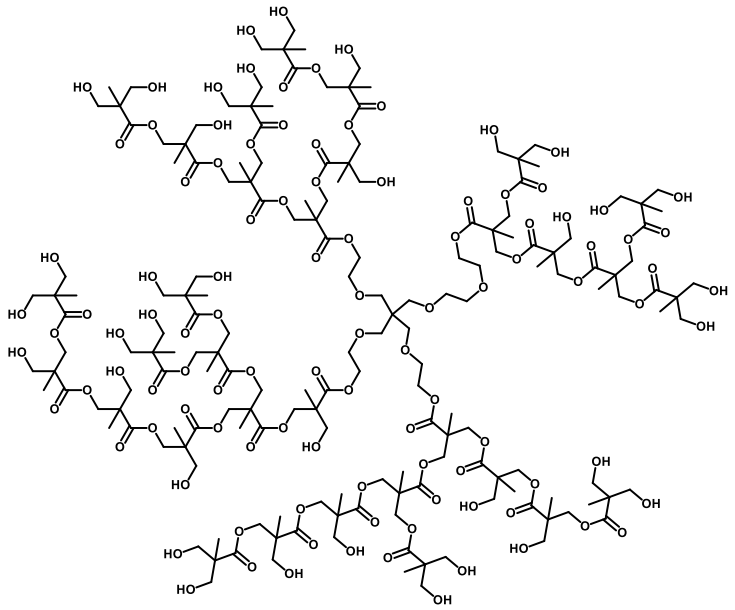

Scheme 5.1 Example of a fourth generation hydroxyl-functional dendritic hyperbranched polyester, Boltorn™ H40 (HBP4) accounting for imperfect branching.

Sodium montmorillonite clay (Na^+MMT) Cloisite® with a cation exchange capacity (CEC) of 92.6 meq/100 g was purchased from Southern Clay Products. As received clay powder was sifted through a 75 micron sieve, dried at 150 °C under vacuum overnight, and stored over desiccant prior to use. The hydroxyl-functional dendritic hyperbranched polyester, Boltorn™ H40 (HBP4), was obtained from Perstorp Specialty Chemicals AB in the form of pellets. A schematic representation of the hyperbranched structure of HBP4 is shown in Scheme 5.1.

The nanocomposites utilized in this study were created via a solution-intercalation method and were from the same batches investigated previously [28]. The required amount of Na^+MMT clay was first dispersed in deionized water at 50 °C and stirred for at least 8 hours to optimize clay delamination. The aqueous concentration of the clay was kept below 1% wt/wt in order to ensure that individual clay layers were well dispersed.

When sufficiently diluted, Na^{+}MMT particles are known to delaminate into single layers [69].

The required amount of Boltorn™ polyol was dissolved in boiling DI water. The concentration of polymer in water was kept at or below 10% wt/wt as this concentration was observed to effectively disperse and dissolve the HBP4. This solution was then quantitatively transferred into the clay dispersion. This combined solution was rapidly stirred in open air at 50 °C until the dispersion approached the level of the stir bar but remained in a liquid state. It was then transferred to Teflon trays and dried for two days in a convection oven at 50 °C. Two further days of drying followed, under vacuum, at 120 °C. This temperature was demonstrated as optimal for removing water from Boltorn™ polyols [70]. The resulting nanocomposite films were stored over desiccant at room temperature. The mineral volume fraction of clay in the nanocomposites, ϕ_m, was calculated from the corresponding mineral weight fractions, w_m, and the nanocomposite densities were measured by a buoyancy method as reported in our previous publication [28]. As also reported in our previous study, no changes in density of the amorphous HBP4 were observed in the nanocomposites [28].

Characterization

The thermal behavior of the nanocomposite and control films was evaluated using a TA Instruments Q2000 Differential Scanning Calorimeter. Heating and cooling scans were carried out at a 10 °C/min rate over a range of -50 to 150 °C under a dry nitrogen atmosphere. The nanocomposites were taken directly from the desiccator and placed into sealed aluminum pans to prevent water uptake. Second heating scans were utilized for the

analysis to eliminate any physical ageing effects. Second and third heating scans were self-consistent. The T_g of the nanocomposites and the ΔC_p, at T_g, were determined according to previously established methodology reported elsewhere [71-72]. The T_g was taken as the point where half of the polymer was devitrified as determined from the heat capacity increase, where a line drawn median to the heat capacity lines for the glass and liquid behavior intersects the DSC curve.

The positron annihilation lifetime spectroscopy (PALS) experiments were conducted using a fast-fast coincidence system with a time resolution of 220 ps. 1 x 1 cm^2 area pieces were cut from each sample film for analysis. On each side of a 30 μCi ^{22}Na positron source, pieces of the sample films were stacked to a total thickness of 1 mm. The sample cell was kept under vacuum during the experiments. All measurements were taken over one hour, for a total of 1 x 10^6 counts in each PALS spectrum. Temperature measurements were taken by first decreasing the temperature to -30 °C then waiting for one hour to allow for equilibrium before beginning the first experiment. The temperature was then sequentially increased in 10 °C steps, collecting a spectrum at each step, after waiting 10 min to allow for equilibration. The PALS spectra were tested against three and four component fits using the PATFIT 88 software package [73].

For transmission electron microscopy (TEM), the nanocomposite films were embedded in epoxy resin and microtomed. Approximately 90 nm thick sections were cut at -30 °C perpendicular to the film surface using a Leica cryo-ultramicrotome FC6 equipped with freshly cut glass knives. These sections were imaged using a Zeiss 109T TEM operated at 80 kV under bright field conditions. Since the silicate layers possess a

higher electron density than the surrounding HBP matrix, they appear darker in the images.

Results and Discussion

Probing the amorphous phase of nanocomposites by DSC

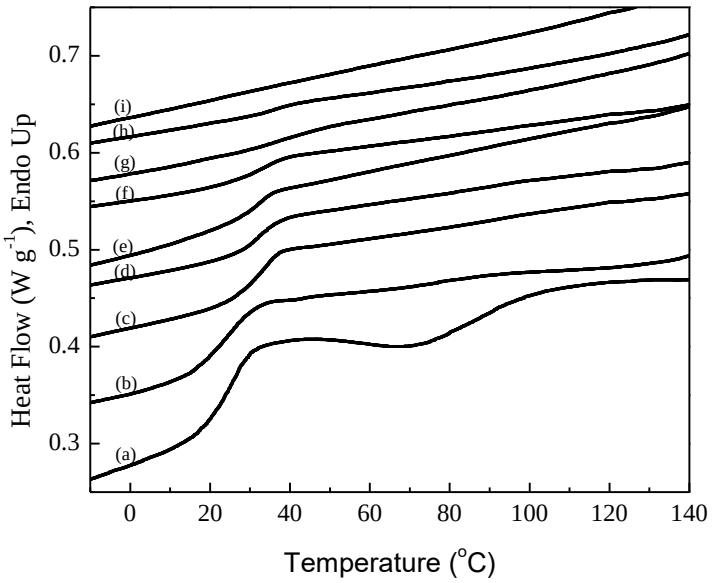

Figure 5.1 DSC thermograms of HBP4/Na^+MMT nanocomposites with different clay loading a) 0 wt%, b) 10 wt%, c) 20 wt%, d) 30 wt%, e) 40 wt%, f) 50 wt%, g) 60 wt%, h) 70 wt%, and i) 80 wt% Na^+MMT. Curves vertically offset to aid the viewer.

Representative thermal scans of the nanocomposite systems and the pure HBP4 control are shown in Figure 5.1. The HBP4 control exhibited a glass transition temperature at 24.2 ± 1.2 °C followed first by exothermic and then endothermic events with corresponding minima and maxima at around 70 °C and 110 °C. Žagar et al. previously attributed these exo- and endo- events to the formation and cleavage of H-bonds between multiple hydroxyl groups [9-10]. However, our most recent results, to be reported in a forthcoming publication, led us to attribute the exothermic and endothermic

events, respectively, to the formation and melting of an ordered mesophase involving the lateral attachment of the HBP linear segments, via hydroxyl-hydroxyl or hydroxyl-carbonyl group H-bonding. The magnitude of these exo and endo events dramatically decreased with clay content until they were completely undetectable above 20% wt/wt Na^{+}MMT, suggesting that adding clay suppresses the formation of the mesophase, likely due to a disruption of the interchain H-bonding under confinement. Consistent with this interpretation, based on the measurements of the activation energy for the dielectric γ-relaxation, which is due to the hydroxyl group motions in similar nanocomposites, Androulaki et al. concluded [29] that the flattening of dendritic HBPs in the presence of clay surfaces impedes H-bond formation.

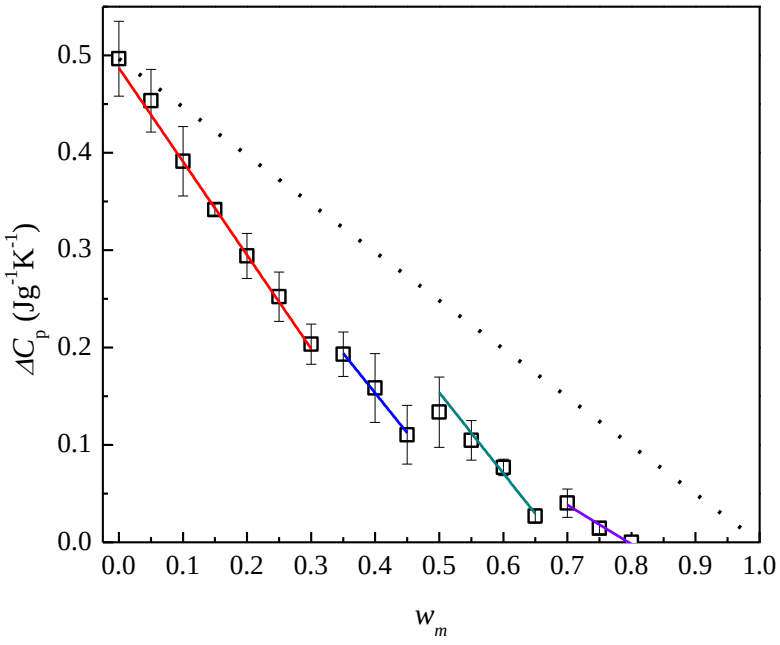

Figure 5.2 ΔC_p at T_g for HBP4 nanocomposites as a function of Na^{+}MMT weight fraction, w_m. The dashed line represents the standard two-phase model prediction. Error bars represent standard deviations from multiple DSC runs. The colored shifted striations help visualize the step-wise changes in ΔC_p.

The bulk T_g exhibited a moderate, approximately 12 °C, increase while the ΔC_p at T_g decreased dramatically with the addition of clay (Figure 5.1). At 80% wt/wt and higher clay content, the glass transition in the nanocomposites was fully suppressed. The measured T_g and ΔC_p at T_g are displayed in Table 1. Standard deviations listed are based on numerous discrete DSC measurements made on each sample. Figure 5.2 depicts the heat capacity changes for the nanocomposites as a function of weight fraction of Na^+MMT, w_m. In the case of a two phase composite system consisting of an amorphous polymer phase and inorganic clay particles, the ΔC_p can be expected to decrease linearly with the clay content as depicted by the dashed line in Figure 5.2. However, in reality, the ΔC_p behavior for the nanocomposites deviated significantly from this linear trend. The segmental mobility of a considerable portion of the amorphous HBP polymer is clearly suppressed in the presence of the clay surfaces.

The deviation from the two-phase prediction in Figure 5.2 grew in significance as the clay content increased linearly to approximately 30% wt/wt, then exhibited a series of step-like decreases, punctuated by linear increases, which can be seen in Figure 5.2 as the colored shifted linear striations. These linear groupings will be described in more depth later, but are attributed to the different intercalation interlayer spacing groups as shown in Figure 5.3 and depicted as color-coordinated layers in Schematic 2. For each group, the ΔC_p deviates increasingly from the two phase model as more clay layers per tactoid allow for more constrained polymer. This trend follows with increasing clay content until the interlayer spacing changes (decreases) and an increase in the amount of unconstrained polymer is observed as there is less polymer immobilized between each clay layer.

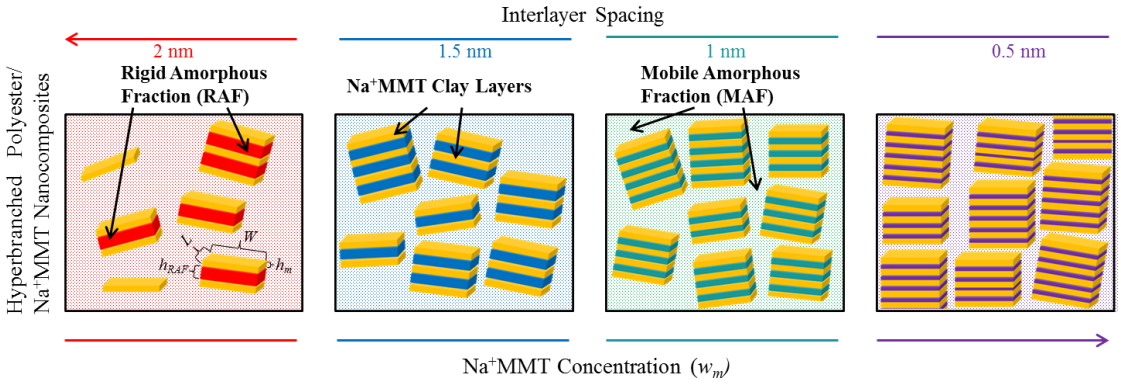

Scheme 5.2 Depiction of the decrease in the intercalated clay interlayer spacing with increased clay concentration. The different colors of the confined polymer phase (RAF) represent groupings of nanocomposite concentrations with distinct interlayer spacing thicknesses from 2 to 0.5 nm. The MAF is represented by the patterned lighter shaded area surrounding the clay tactoids.

The weight fraction of the amorphous polymer phase which contributed to the step in the heat capacity at T_g, mobile amorphous fraction (MAF), was calculated based on the corresponding ΔC_p for the nanocomposite and ΔC_p^o for the pristine HBP4 polymer, $w_{MAF} = \frac{\Delta C_p}{\Delta C_p^0}$. The fraction of the immobilized amorphous phase, the rigid amorphous fraction (RAF), of the HPB4 polymer was calculated assuming $w_m + w_{RAF} + w_{MAF} = 1$.

Table 5.1 Glass transition temperatures (T_g), changes in heat capacity (ΔC_p), and calculated amorphous fractions with Na$^+$MMT content.

Weight fraction Na$^+$MMT (w_m)	Volume fraction Na$^+$MMT (φ_m)	Glass transition temperature ± std deviation (T_g)	Heat capacity jump at T_g ± std deviation (ΔC_p)	Rigid Amorphous Fraction (w_{RAF})	Mobile Amorphous Fraction (w_{MAF})
0.00	0.000	24.2 ± 1.2	0.497 ± 0.038	0.0	1.0
0.05	0.023	23.6 ± 1.2	0.453 ± 0.032	0.04 ± 0.09	0.91 ± 0.09
0.10	0.048	24.7 ± 0.5	0.391 ± 0.036	0.11 ± 0.09	0.79 ± 0.09
0.15	0.075	29.2 ± 1.2	0.342 ± 0.006	0.16 ± 0.05	0.69 ± 0.05
0.20	0.102	31.4 ± 1.0	0.294 ± 0.023	0.21 ± 0.06	0.59 ± 0.06

0.25	0.132	30.4 ± 0.7	0.252 ± 0.025	0.24 ± 0.06	0.51 ± 0.06
0.30	0.164	31.7 ± 1.2	0.203 ± 0.011	0.29 ± 0.04	0.41 ± 0.04
0.35	0.197	31.7 ± 0.7	0.193 ± 0.023	0.26 ± 0.05	0.39 ± 0.05
0.40	0.233	30.7 ± 0.6	0.158 ± 0.035	0.28 ± 0.07	0.32 ± 0.07
0.45	0.272	32.3 ± 1.6	0.110 ± 0.030	0.33 ± 0.06	0.22 ± 0.06
0.50	0.313	29.2 ± 1.4	0.134 ± 0.036	0.23 ± 0.08	0.27 ± 0.08
0.55	0.358	30.4 ± 1.1	0.105 ± 0.020	0.24 ± 0.04	0.21 ± 0.04
0.60	0.406	37.8 ± 2.8	0.077 ± 0.008	0.25 ± 0.02	0.15 ± 0.02
0.65	0.459	35.0 ± 1.4	0.027 ± 0.007	0.30 ± 0.01	0.05 ± 0.01
0.70	0.516	36.0 ± 0.8	0.040 ± 0.015	0.22 ± 0.03	0.08 ± 0.03
0.75	0.578	36.3 ± 2.3	0.014 ± 0.006	0.22 ± 0.01	0.03 ± 0.01
0.80	0.646	NA	0.000 ± 0.000	0.20	0

As mentioned previously, we attributed the step-like ΔC_p behavior (the colored striations in Figure 5.2) to the step-like intercalation behavior. Naturally, a question was posed if the step-like interlayer spacing variations can be directly calculated from the ΔC_p behavior. The highly ordered intercalated morphology of the nanocomposites enabled us to consider a simple series model in which multiple confined polymer layers are alternated between mineral layers.

We assume that the interlayers are composed entirely of RAF with the thickness of these layers designated as h_{RAF}. The volume of the clay can be expressed as, $V_m = nL_mW_mh_m$, where n equals the number of MMT layers and W and L represent the length and width of the clay stacks respectively. The thickness of the individual MMT layers, h_m , was previously determined to be 0.96 nm. The large lateral dimensions of the clay far exceed the 1 nm layer thickness; therefore edge effects were neglected in this analysis. Since the RAF is assumed to be only within the MMT stacks, the volume of RAF can be

expressed as $V_{RAF} = (n-1)L_{RAF}W_{RAF}h_{RAF}$. Complete surface coverage of the MMT layers by the RAF is assumed within these stacks, thus *L* and *W* for the RAF and MMT are assumed equal and the ratio of V_{RAF}/V_m, which directly relates the heights of the RAF and MMT layers, can be expressed as:

$$\frac{V_{RAF}}{V_m} = \frac{(n-1)h_{RAF}}{nh_m} \approx \frac{h_{RAF}}{h_m} \qquad (2)$$

TEM observations confirm that the number of layers in the intercalated stacks increases with clay content to an extent that enable us to simplify Eqn. 2 by removing the necessity to know the precise number of clay layers. Supplementary Figure 5.1 shows through high and low resolution TEM micrographs that above 15% wt/wt the number of clay layers per stack is greater than 10 (~15-20). This simplification will likely not hold at low clay loadings. By combining Eqn. 2 with the heat capacity prediction stated previously, $w_{MAF} = \frac{\Delta C_p}{\Delta C_p^0}$, and solving for h_{RAF}, an equation was established where the interlayer spacing can be calculated from the observed ΔC_p values, determined by DSC, and the known clay compositions.

$$h_{RAF} = \frac{(1-w_m-\Delta C_p/\Delta C_p^0)h_m\rho_m}{\rho_{RAF}w_m} \qquad (3)$$

As detailed in our previous publication, no changes in density of the HBP4 were observed in the nanocomposites [28]. Therefore, the densities of the MAF, ρ_{MAF}, and the RAF, ρ_{RAF}, were assumed to be identical with a value of 1.306 g/cm^3. A density, ρ_m, of 2.86 g/cm^3 was employed for the Na^+MMT Cloisite® mineral layers in these calculations.

Figure 5.3 shows the consistency between the interlayer spacings observed by XRD and those calculated from Eqn. 3. Moreover, the step-wise nature of the interlayer spacing correlates to the steps observed in Figure 5.2 as marked by the linearly off-set

striations for clarity. Note, the proposed DSC based analysis does not mirror the fact that different intercalated states can coexist in a given nanocomposite leading to two distinct intercalation peaks on the same diffractogram [28]. One plausible argument, why despite this limitation we see a good overall agreement between the interlayer spacing steps observed by XRD and predicted from Eqn. 3, is that in these mixed intercalated states one population always strongly dominates the other and is mainly reflected by DSC.

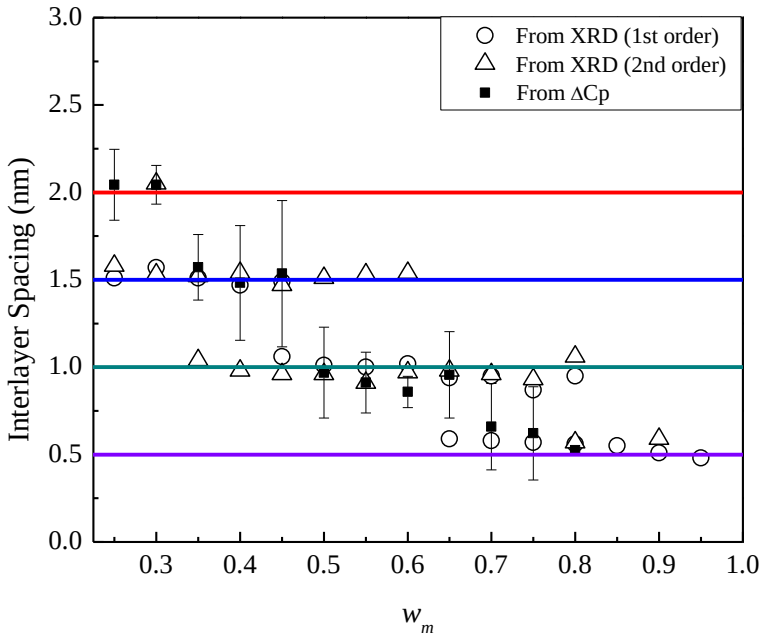

Figure 5.3 Interlayer spacings predicted using Eqn. 3 (■), calculated from the experimentally determined values for ΔC_p at T_g. Interlayer spacings observed directly by XRD for the powdered HBP4 nanocomposites (1st order diffraction,○, and 2nd order diffraction , Δ) are also plotted as a function of weight fraction Na^+MMT. Error bars represent the error propagated from the ΔC_p determinations. Colored gridlines represent the differentiated nanocomposite groupings with different interlayer spacings as observed in Figure 5.2.

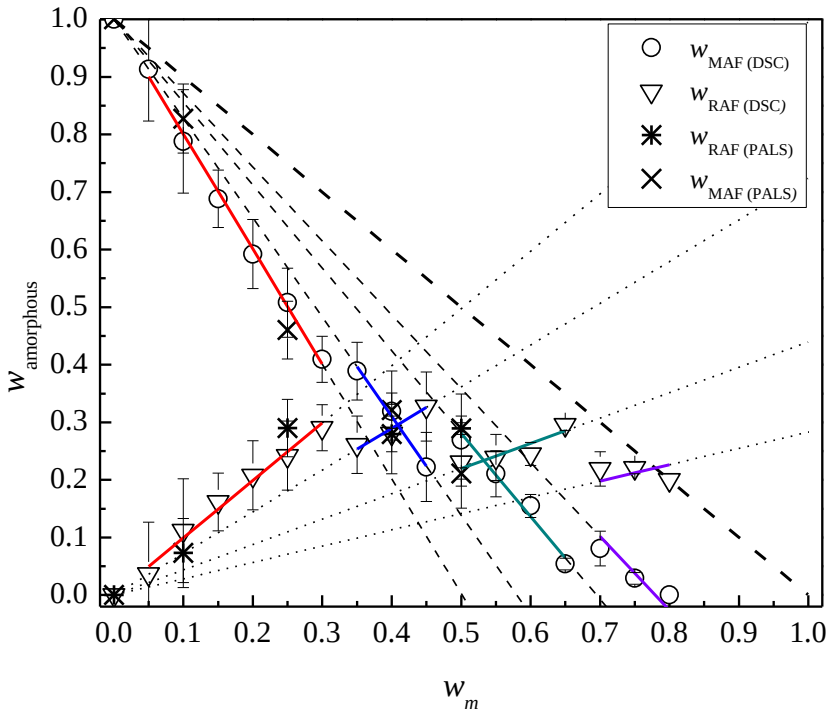

Figure 5.4 Weight fractions of MAF (○) and RAF (▽) as determined from ΔC_p and weight fractions of MAF (✕) and RAF (✳) determined from PALS for HBP4 nanocomposites as a function of w_m. The dashed line represents a two-phase model, ie. just MAF and clay. Colored striations represent linear fits of groups of nanocomposites with increasingly smaller interlayer spacings.

As expected, the amorphous phase fractions are linearly dependent on the interlayer spacing between the platelets, h_{RAF}. From Eqn. 3, w_{RAF} and w_{MAF} are related to h_{RAF} by the relationship $w_{RAF} = \frac{h_{RAF}\rho_{RAF}w_m}{h_m\rho_m}$ and $w_{MAF} = 1 - w_m - \frac{h_{RAF}\rho_{RAF}w_m}{h_m\rho_m}$, respectively. The slopes of the plots of w_{MAF} and w_{RAF} versus w_m for the previously differentiated nanocomposite concentration groups are depicted by the dotted lines. The slopes of the linear fittings of the different nanocomposite groups (labeled by different colors) clearly depict the changes in interlayer spacings with shifts from group to group. i.e., the group labeled green (0.5 to 0.65 wt/wt) has an approximately 50% reduction in its

slope as compared to the group labeled red (0.05 to 0.3 wt/wt). This correlates to the 50% reduction in interlayer spacing between the two groups, from 2 to 1 nm as seen in Figure 5.3. Another observation is the fact that at very low clay concentrations, < 10% wt/wt, it appears that the model still holds for this regime where the clay morphology is a mixture of exfoliated clay platelets and small tactoids with an average interlayer spacing of 2 nm. This would hint that RAF can also form on the surfaces of the exfoliated clay particles (1 nm on each side), contrary to our assumption that RAF is only located in the interlayer spaces. This cannot be confirmed as many more experimental data points at these very low concentrations, with very precise ΔC_p measurements, would be needed before we can conclude on this issue. It is also quite possible that no RAF would be observed in a completely exfoliated system and that even at our lowest clay concentration, 0.05 wt/wt, the system is still predominately intercalated. Above a w_m of 0.8, all of the MAF is depleted and the w_{RAF} would decrease in a linear two phase model manner as the system is comprised of just RAF and clay.

It is clear by comparing the changes in the RAF and MAF versus clay content trends that the RAF and MAF are dependent upon more than just the fraction of clay within the systems. The changing clay morphologies directly impact RAF formation as well.

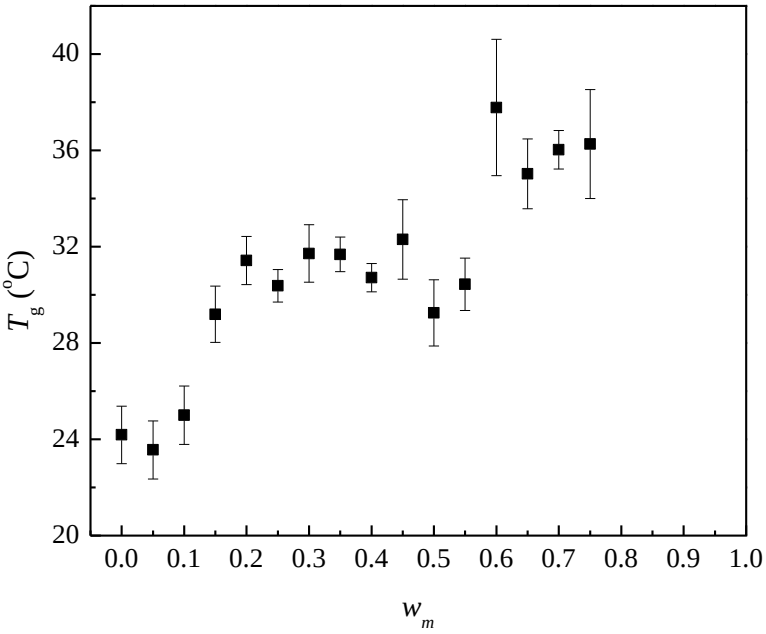

Figure 5.5 Glass transition temperature as a function of weight fraction Na^+MMT for HBP4 nanocomposites. Error bars represent standard deviations.

Finally, the changes observed by DSC in the bulk glass transition temperature with clay content of the nanocomposites are shown in Figure 5.5. The T_g remained near 24 ˚C at low clay concentrations until it increased between ~10-30% wt/wt to a relative plateau region at about 31 ˚C where it remained until ~50-55% wt/wt clay, where it increased to a final plateau at 36 ˚C between 60-75% wt/wt clay. At and above 80% wt/wt Na^+MMT, T_g detection was not experimentally possible due to the small amplitude of the transition peak at such low polymer concentrations (Figure 5.1).

As the T_g is assumed to be solely attributed to the MAF and not the RAF, we believe any increases in T_g with increasing weight fraction of clay loading is a reflection of MAF that has become increasingly affected by proximity to the clay particle surfaces. Thus, we accredit the T_g of these nanocomposites to be a combination of contributions

from two MAF populations. The T_g is affected by perturbed MAF regions, situated in the vicinity of the polymer-clay interfaces, and unperturbed MAF regions, situated at large enough distances between the clay tactoids to exhibit the original polymer T_g. The magnitude in the change in T_g will then depend on the relative amounts of perturbed polymer and unperturbed polymer.

We believe, congruent with the data, that the T_g behavior over the different nanoparticle concentration regimes can be explained when analyzed alongside the interlayer spacing and amorphous fraction data in Figure 5.3 and 5.4. At very low concentrations, less than 10% wt/wt clay, the fraction of perturbed regions, existing only at the clay interfaces, is very small and thus the T_g is only slightly effected by the low amount of clay inclusion. From 10 to 30% wt/wt clay, a dramatic increase in T_g is observed, which can be attributed to the sharp overall decrease in MAF (~0.8 to ~0.4 wt/wt, i.e. red grouping in Figure 5.4) taking place in this regime. As the overall MAF is reduced, the amount of perturbed MAF becomes increasingly significant with the development of more interfaces. Within the range 30-50% wt/wt clay, the increase in T_g of the nanocomposite systems becomes much less pronounced. We attribute this relative constant T_g regime, around 31°C, to the stepwise change in MAF which decreases much less markedly, ~40% to ~30% wt/wt, than for the case of constant interlayer spacing. As the interlayer spacings decrease from one differentiated group to another with increased clay content, the clay tactoids incorporate more clay layers per tactoid, but with less RAF constrained in each clay layer, hence the amount of unperturbed MAF can increase. Thus, there is a trade-off in this regime that keeps the apparent T_g relatively constant. Finally, we attribute the last regime of increased T_g, above 55% wt/wt clay, to the small

concentration of MAF that remains becoming increasingly perturbed by the clay tactoids as they become closer in proximity.

The success in accurately measuring MAF and RAF content in this nanocomposite system led us to explore the use of positron annihilation lifetime spectroscopy (PALS) which we earlier applied successfully to probe free volume changes in the MAF and RAF in semicrystalline polyethylene terephthalate (PET) [35]. Nanocomposites should prove to be even better suited for this technique as, lacking crystallization, they are much less complex, consisting of only amorphous polymer and thermally stable nanoplatelets.

Probing the amorphous fractions by PALS

The use of PALS in the analysis of the RAF is novel with only a few attempts in semi-crystalline polymers that have been reported on. Our previous work focused on using PALS to probe the free volume behavior of the RAF and MAF in a semi-crystalline PET system [35]. It was confirmed that the RAF exhibited a larger free volume in the glassy state than the MAF at ambient temperature due to the differences in their respective vitrification temperatures. The vitrification temperature for the RAF is the crystallization temperature while the MAF vitrifies at the normal glass transition temperature. This difference results in a larger excess hole free volume accumulated by the RAF upon cooling as compared to the MAF. When both fractions are melted on heating their respective free volumes merge.

To our best knowledge relatively few PALS studies have reported on the free volume in the confined amorphous phase in particulate containing nanocomposites. A

few of the early attempts are reviewed in [76]. Practically all of them were limited by the extent of the mineral phase employed, polymer crystallization, and often by using surfactants, all of which made the analysis of this effect very convoluted. In contrast, the important advantages of our amorphous polymer nanocomposite system include no need of using a surfactant and the fact that these composites can be generated within a very broad range of compositions.

In the present study, we employ positron annihilation lifetime spectroscopy (PALS) in a combination with differential scanning calorimetry (DSC) to analyze the amount and nature of free volume of the RAF and MAF in the Na^{+}MMT/HBP4 nanocomposite system. The RAF content, quantified from changes in heat capacity with clay content, is compared with estimates using PALS through analysis of the glassy nature of the RAF through changes in the thermal expansivity of free volume holes as a function of clay composition.

To enable this analysis, a few research questions had to be addressed. We needed to determine if o-Ps formed inside the silicate crystals and if the o-Ps had a different probability of forming in the polymer situated in the interlayer spacings (RAF) versus the polymer between the clay stacks (MAF). Finally, we needed to determine if the o-Ps exhibit the same annihilation behavior in the MAF and RAF regimes.

To verify that the contribution of the o-Ps from the clay layers was indeed minimal, a PALS analysis of pure Na^{+}MMT was performed. The clay was dried for two days under vacuum at 120 °C and then pressed in a mold to form 10 mm by 1 mm discs subjected to PALS analysis. o-Ps lifetimes in the range of 1-10 *ns* were not observed from PALS temperature scans of the clay.

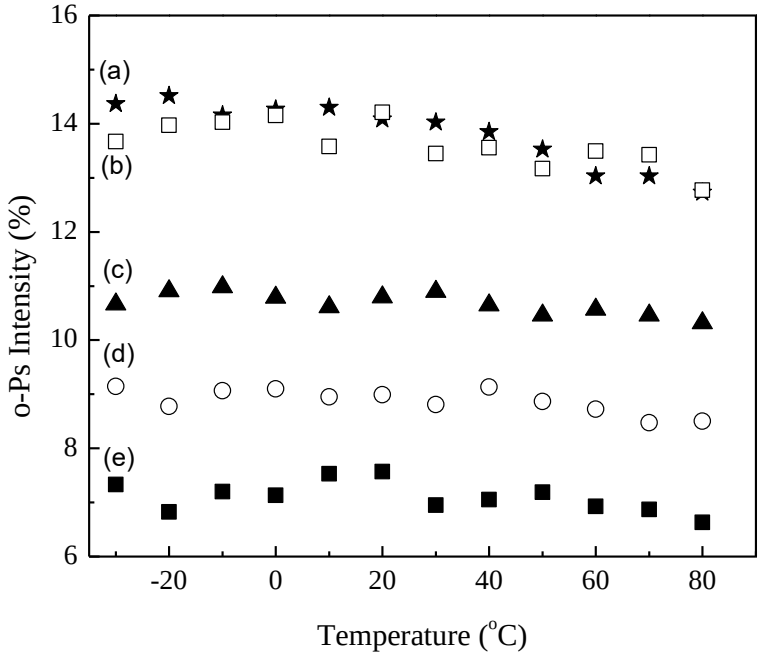

Figure 5.6 Orthopositronium intensities, I_3, for HBP4 and Na^+MMT/HBP4 nanocomposites as a function of temperature at the following MMT fractions: (a) 0%, (b) 25%, (c) 40%, (d) 60% and (e) 70% wt/wt.

In Figure 5.6, we show the temperature dependence of the o-Ps intensities, I_3, for pure HBP4 and Na^+MMT/HBP4 nanocomposites. The o-Ps intensity, I_3, exhibited a weak temperature dependence encompassing the glass and liquid states, typical of amorphous polymers, indicating a corresponding weak temperature dependence in hole density, above and below the T_g [77]. This also suggests that the MAF and RAF regions have consistent hole densities. If the hole densities differed, then one would expect a change in I_3 above the glass transition where only the RAF remains vitrified. Also, increased data scatter causing limited measurement reliability was experienced at high clay concentrations as the amount of polymer to analyze becomes very small, limiting the applicability of some of the data at high concentrations in further analysis.

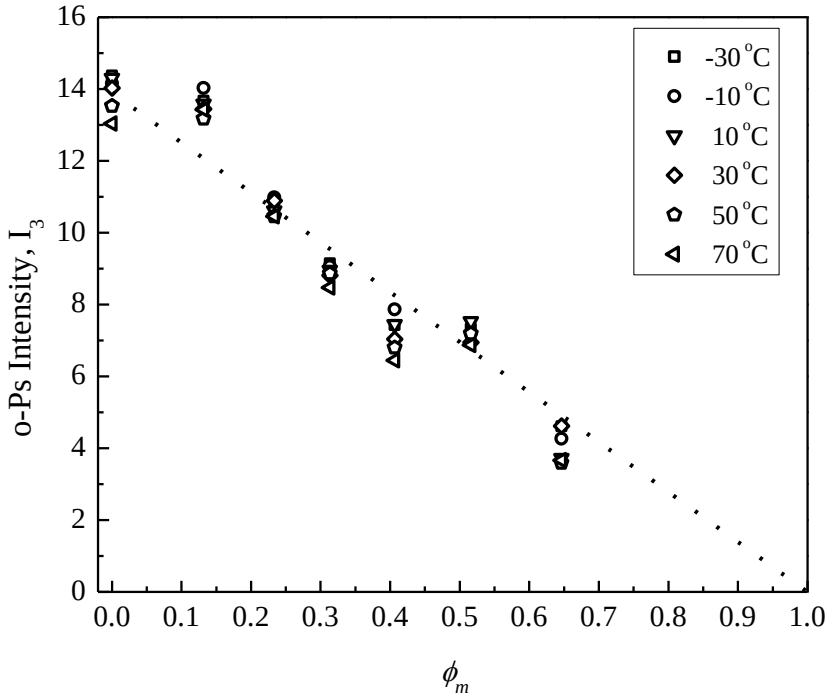

Figure 5.7 o-Ps Intensity, I_3, at -30 °C, -10 °C, 10 °C, 30 °C, 50 °C, and 70 °C versus volume fraction Na^+MMT. The dotted line represents a perfect linear correlation between I_3 and the volume fraction of clay.

The o-Ps intensity, I_3, is also plotted as a function of clay filler volume fraction in Figure 5.7. The overall o-Ps intensity of the nanocomposite samples decreased linearly with increasing clay content. Similar reductions in I_3 have been observed in other clay nanocomposite systems [78-80] and in certain semicrystalline systems, such as poly(ether ether ketone) where the o-Ps could not form within the polymer crystallites [81-82]. As mentioned previously, there is negligible positronium formation in the clay layers [83] limiting the regions capable of o-Ps formation to the amorphous polymer phases. Therefore, the linear trend of the o-Ps intensity with clay loading is suggestive of a two phase model dependent only on the polymer fraction and clay content. As there is no

noticeable deviation from this two phase model, it can be reasoned that there is a similar probability of o-PS formation in the RAF and MAF regions.

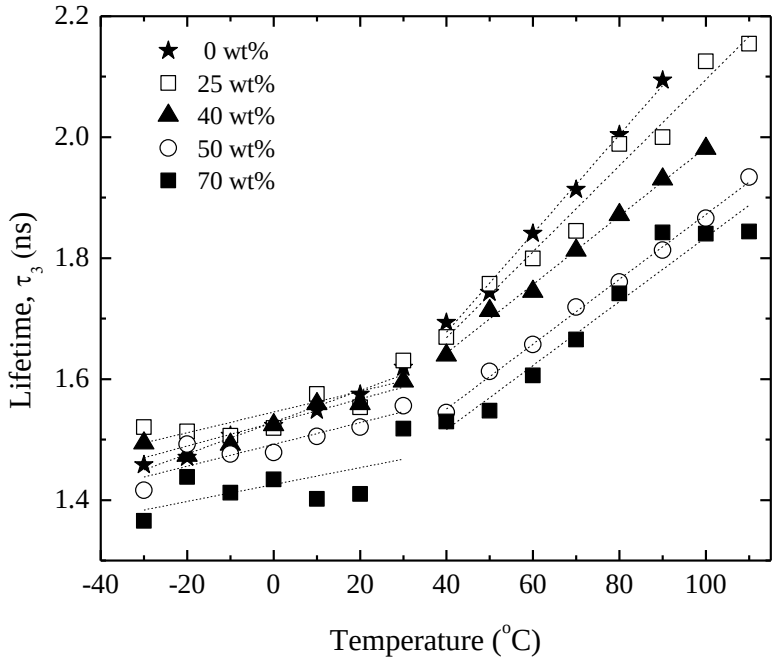

Figure 5.8 Orthopositronium lifetimes, τ_3, for HBP4 nanocomposites as a function of temperature at the following MMT fractions: 0%, 25%, 40%, 50% and 70% wt/wt. The dotted lines represent linear fits of the data above and below the T_g.

As noted in Eqn. 1, the o-Ps lifetime, τ_3, is directly related to the hole volume in the system. The temperature dependence of τ_3 is shown in Figure 5.8. The τ_3 values below T_g for the different clay concentrations remained very similar, as expected, except at very high loadings. While we could speculate on the cause of this decrease in τ_3, e.g. changes in hole shape from increased orientation of the clay, as previously mentioned, data reliability is questionable at high clay concentrations where the relative amount of polymer is small. Therefore, further analysis was confined to clay concentrations at and below 50% wt/wt. Unlike I_3, τ_3 values did increase with temperature, indicative of the

expansion of hole sizes on heating. The thermal expansivity of the hole volume was greater above the glass transition temperature, which is reflected in the different slopes of τ_3 with temperature above and below T_g. The slopes of τ_3 with temperature above T_g decreased with increasing clay content, but the slopes below T_g remained relatively constant, irrespective of clay content. This behavior is consistent with the results of Harms et al. in a system of poly(ethylene-alt-propylene) and hydrophobically modified silica nanoparticles [84].

Below T_g, both the amorphous HBP4 confined by the clay layers and the surrounding free HBP4 are in the glassy state. The constant slopes indicate that the thermal expansivity of the RAF phase is equal to that of the pure HBP4 in the glassy state. Above T_g, decreases in the τ_3 versus T slope of the nanocomposites, relative to the slope of the pure HBP4, indicate that a portion of the amorphous phase possesses a lower hole thermal expansivity than the pure HBP4 as the Na^+MMT does not contribute to the o-Ps lifetimes, as established previously. Therefore, above the T_g, the free volume changes detectable by PALS can only be due to contributions from the RAF and MAF phases. Since the RAF exhibited the same thermal expansion properties as the bulk HBP4 in the glassy state, we hypothesized that the decreases in the τ_3 slope of the nanocomposites above T_g, relative to the neat HBP4, are due to the additive contribution of the free volume hole sizes of the RAF and MAF fractions in the nanocomposites, since the RAF is expected to remain vitrified above the bulk T_g.

As the data shows that the MAF and RAF have similar o-Ps concentrations but exhibit different thermal expansivities in hole sizes above the T_g, the possibility to quantify the RAF and MAF phases became clear.

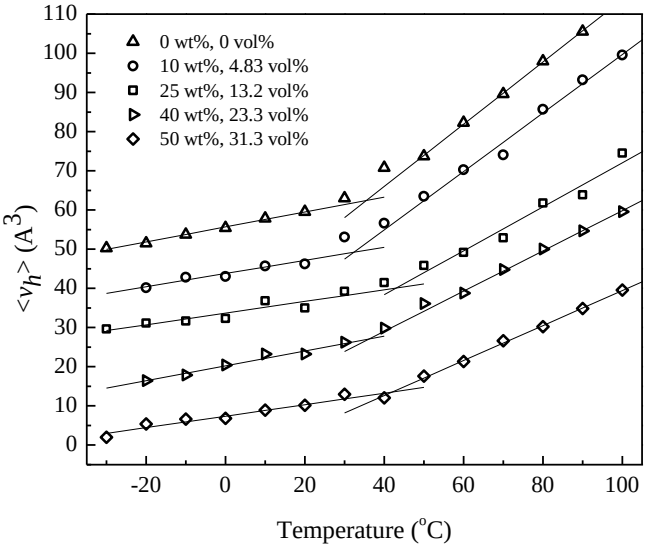

Figure 5.9 Hole free volume, v_h, as a function of temperature plots for the nanocomposites. Vertically offset for clarity from 0% vol/vol.

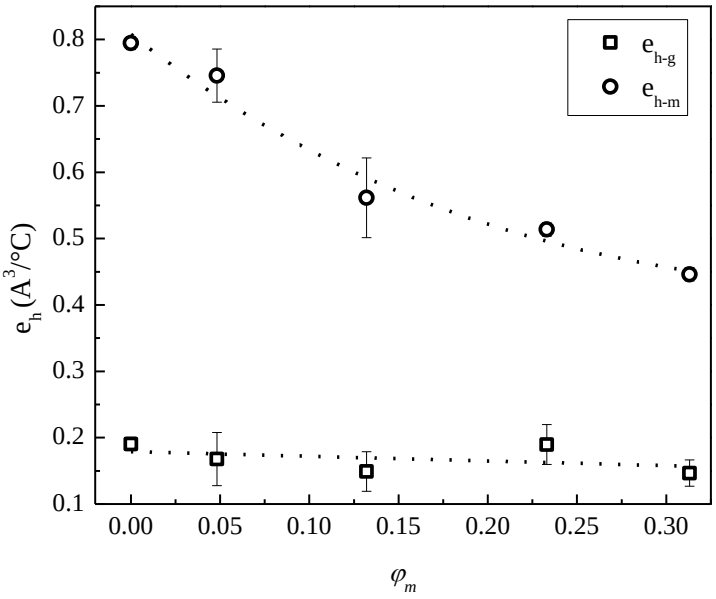

Figure 5.10 Thermal expansivity of the nanocomposites systems above (o) and below (□) the T_g. Error bars represent the standard errors of the linear fits from Figure 5.9.

The average hole size, v_h, was calculated by $v_h = (4/3)\pi R^3$, where R is calculated from Eqn. 1, and is plotted in Figure 5.9. v_h ranges from 50-120 Å^3 over the temperature range studied. The hole thermal expansivity, dv_h/dT, of the vitrified, neat, HBP4 below T_g was taken to be equal to that of the RAF, which remains vitrified by clay confinement above T_g. Since the contributions of RAF and MAF to v_h are considered additive we have the following relationship

$$v_h = \frac{N^{RAF} v_h^{RAF} + N^{MAF} v_h^{MAF}}{N^{RAF} + N^{MAF}} \qquad (4)$$

where v_h is the average hole volume as measured for the composite, v_h^{RAF} is the average hole volume as measured for RAF, and v_h^{MAF} is the average hole volume as measured for MAF. N^{RAF} is the number of free volume holes for the RAF, and N^{MAF} is the number of free volume holes for the MAF. Since this analysis is dependent upon the v_h slopes with temperature, a linear regression of v_h in the glassy state and in the equilibrium liquid state above T_g was required, examples of which are included in Figure 5.9. For this linear regression, the data points from 20-40 °C are excluded as they are very close to the glass transition. The linear slope of v_h versus T, e_h, for the nanocomposites were thusly defined as:

$$e_h = \frac{dv_h}{dT} \qquad (5)$$

and plotted in Figure 5.10 where $e_{h\text{-}g}$ and $e_{h\text{-}m}$ refer to the linear slopes below and above the T_g, respectively. Since the slope of the v_h versus T plot for all of the samples below T_g remained constant, the linear slope of the RAF below T_g, dv_h/dT, was defined as e_h^{RAF}. As there was no HBP4 crystallinity evidenced by DSC or XRD for the pure HBP4 above T_g, the amorphous phase was considered to be composed entirely of MAF and dv_h/dT above

T_g was defined as e_h^{MAF}. Based upon the negligible changes of I_3, above and below T_g, we assume that the number density of holes, $n = N_i/V_i$, is the same for RAF and MAF. Since n is constant, Eqn. 4 can be rearranged as follows where $\varphi_{RAF} + \varphi_{MAF} + \varphi_m = 1$.

$$v_h = \frac{\varphi_{RAF} v_h^{RAF} + \varphi_{MAF} v_h^{MAF}}{\varphi_{RAF} + \varphi_{MAF}} \qquad (6)$$

Taking the derivative of Eqn. 6 with respect to temperature yields the final equation for the slope of v_h with temperature, with no adjustable parameters.

$$e_{h-m} = \frac{\varphi_{RAF} e_h^{RAF} + \varphi_{MAF} e_h^{MAF}}{\varphi_{RAF} + \varphi_{MAF}} \qquad (7)$$

Employing Eqn. 7 allowed for φ_{RAF} and φ_{MAF} to be extracted from the slope, $e_{h\text{-}m}$, of the v_h plots with temperature. The slope below T_g, e_h^{RAF}, was 0.19 Å^3/°C and the slope above T_g, e_h^{MAF}, was 0.80 Å^3/°C for the pure HBP4. The correlation coefficients were at or above 0.99 for the linear regression analysis, and the results from the v_h slope analysis are summarized in Table 5.2. The resulting φ_{RAF} and φ_{MAF} determined from this analysis are shown in Table 5.2 and plotted in Figure 5.4 relative to the loading fraction of Na^+MMT. The volume fractions of the amorphous phases as determined by the previous DSC analysis are included for comparative purposes in Table 5.2.

Table 5.2 Amorphous volume fractions determined from the free volume temperature coefficients of HBP4 nanocomposites.

w_m	φ_m	$e_{h\text{-}g}$ (Å^3/°C)	$e_{h\text{-}m}$ (Å^3/°C)	φ_{MAF} (PALS)	φ_{MAF} (ΔC_p)	φ_{RAF} (PALS)	φ_{RAF} (ΔC_p)
0	0	0.19 ± 0.01	0.80 ± 0.01	1.00	1.00	0.00	0.00

0.10	0.048	0.17 ± 0.04	0.75 ± 0.04	0.88 ± 0.07	0.83 ± 0.10	0.08 ± 0.07	0.12 ± 0.10
0.25	0.132	0.15 ± 0.03	0.56 ± 0.06	0.53 ± 0.06	0.59 ± 0.07	0.34 ± 0.06	0.28 ± 0.07
0.40	0.233	0.19 ± 0.03	0.51 ± 0.01	0.41 ± 0.02	0.41 ± 0.09	0.36 ± 0.02	0.36 ± 0.09
0.50	0.313	0.15 ± 0.02	0.45 ± 0.01	0.29 ± 0.02	0.37 ± 0.11	0.37 ± 0.02	0.32 ± 0.11

As seen in Table 5.2, the volume fractions of amorphous HBP4 determined from the o-Ps lifetime analysis are similar to those determined from analyzing the ΔC_p at T_g. This provides additional evidence that the RAF phase remains vitrified well above T_g due to the constraints imposed by the surfaces of the montmorillonite clay layers. Therefore, it was clearly demonstrated by both the bulk thermal and nanoscopic free volume techniques that the adsorption, flattening, and confinement of the HBP lead to the vitrification of a portion of the HBP, which remains vitrified well above the bulk T_g.

Conclusion

A broad concentration range of nanocomposites, based on the fourth generation of a Boltorn™ dendritic polyol (HBP4) combined with unmodified sodium montmorillonite clay (Na^+MMT), was prepared using water as a solvent (0-100% wt/wt Na^+MMT). The HBP4 exhibits a DSC glass transition temperature ~24 °C, followed by exothermic and endothermic events, attributed to the formation and melting of an ordered mesophase, whose formation is suppressed on addition of clay to form a nanocomposite.

With the addition of clay, the bulk T_g exhibited a modest increase, while the ΔC_p at T_g showed a substantial decrease. The ΔC_p behavior for the nanocomposites deviated significantly from the linear trend expected for a two-phase composite in an unusual step-like fashion indicative of suppression of the segmental mobility of the amorphous HBP polymer. At and above 80% wt/wt of clay, the glass transition in the nanocomposites was fully suppressed. The step-like deviation from the two-phase prediction was demonstrated to correlate to step-like changes in intercalation interlayer spacing groupings observed in a previous study [28]. The weight fraction of the MAF (w_{MAF}), which contributed to the step in the heat capacity at T_g was calculated based on the corresponding $\Delta C_{p.}$ A simple series mathematical model in which multiple confined polymer layers alternate between mineral layers enabled calculation of interlayer spacings from the experimental ΔC_p data which were in excellent agreement with those determined by XRD.

From knowledge of w_{MAF} for each clay content we were able to calculate the amount of RAF (since $w_m + w_{RAF} + w_{MAF} = 1$). As much as ~32% wt/wt of the system was made up of RAF at its maximum. Incremental steps in interlayer spacings observed at 0.3-0.35, 0.45-0.5, and 0.65-0.7 wt/wt clay correlated to abrupt increases in w_{MAF} (decrease in w_{RAF}) at each step, followed by a linear decrease in w_{MAF} (increase in w_{RAF}) with increasing clay content until the next step is reached. Clearly, the changes in the RAF and MAF content depend not only on the fraction of clay within the system but also on the changes in clay morphology.

As the T_g is attributed solely to the MAF and not the immobilized RAF, we believe the observed increases in T_g with increasing weight fraction of clay loading are a

reflection of a MAF fraction whose mobility has become perturbed by the proximity to the clay particles. Thus, we attribute the T_g of these nanocomposites to be a result of the combination of two distinct MAF populations, perturbed and unperturbed MAF situated at large enough distances between the clay tactoids to exhibit the bulk polymer T_g. The magnitude of the change in T_g then depends on the relative amounts of each population.

Positron annihilation spectroscopy (PALS) was used to gain information on the temperature dependence of free volume hole density and average hole sizes from I_3 and τ_3, respectively encompassing the glassy and liquid states. The weak temperature dependence of I_3 indicated similar o-Ps formation probabilities in RAF and MAF. This enabled a novel nanocopic approach to estimate w_{RAF} and w_{MAF} via PALS from the thermal expansivities of hole sizes in the liquid and glassy states. The volume fractions of RAF and MAF of the HBP4 nanocomposites determined from o-Ps lifetime analysis proved to be consistent with those determined from analysis of ΔC_p at T_g. This serves to verify the glassy nature of the RAF constrained by the montmorillonite layers at elevated temperatures.

Acknowledgements

The authors are grateful to the National Science Foundation for support of this work through the Center for Layered Polymeric Systems (DMR 0423914) and MRSEC (DMR-0213883).

Supporting Information

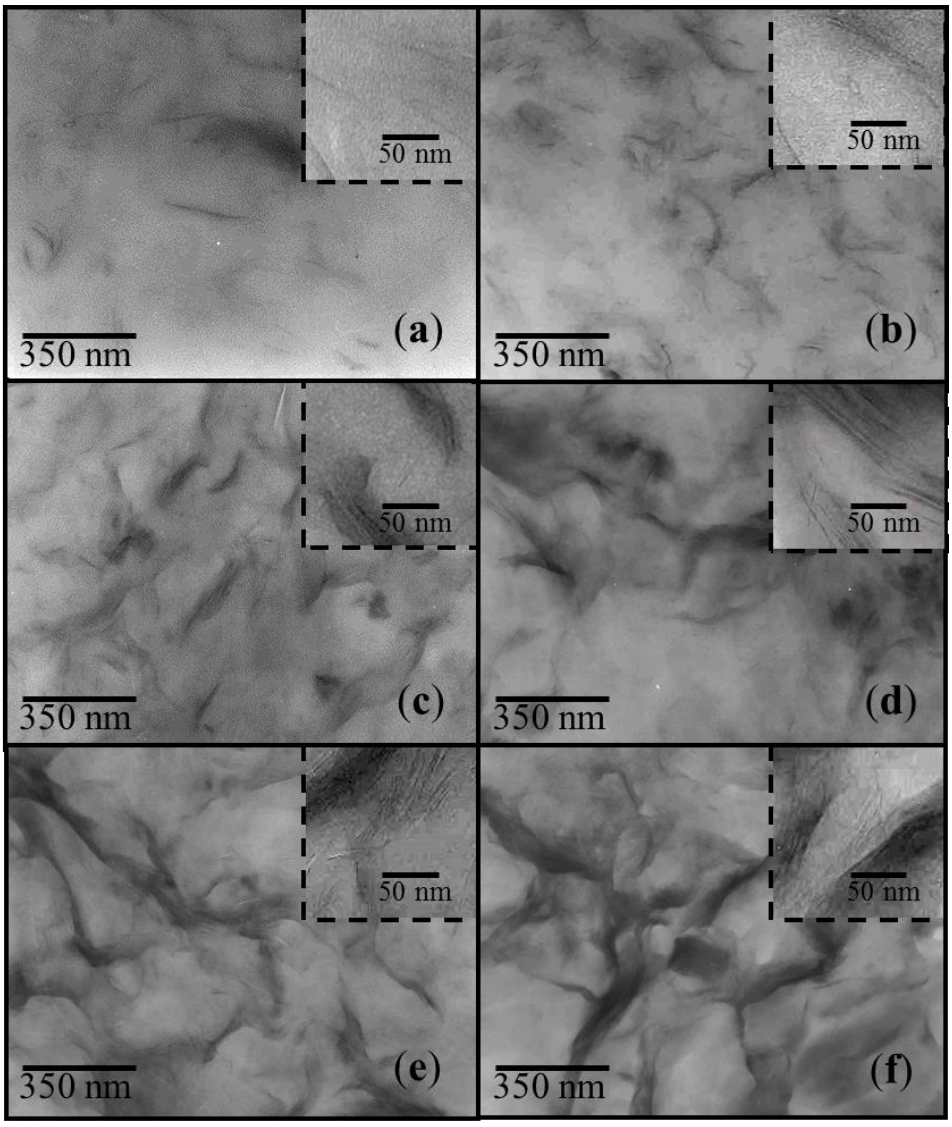

Figure 5.1 Representative high (inserts) and low magnification TEM micrographs of the HBP4/Na^{+}MMT nanocomposites with (a) 1, (b) 5, (c) 15, (d) 20, (e) 25, and (f) 40 % wt/wt clay content.

References

1] Alexandre M, Dubois P. Polymer-layered silicate nanocomposites: preparation, properties, and uses of a new class of materials. Mater. Sci. Eng. 2000; 28: 1.

2] Ray SS, Okamoto M. Polymer/layered silicate nanocomposites: a review from preparation to processing. Prog. Polym. Sci. 2003; 28: 1539.

3] Tjong SC. Structural and mechanical properties of polymer nanocomposites. Mater. Sci. Eng. 2006; 53: 73.

4] Strawhecker KE, Manias E. Structure and Properties of Poly(vinyl alcohol)/Na Montmorillonite Nanocomposites. Chem. Mater. 2000; 12: 2943.

5] Jikei M, Kamimoto M. Hyperbranched polymers: a promising new class of materials. Prog. Polym. Sci. 2001; 26: 1233.

6] Zhu PW, Zheng S, Simon G. Dielectric Relaxations in a Hyperbranched Polyester with Terminal Hydroxyl Groups: Effects of Generation Number. Macromol. Chem. Phys. 2001; 202: 3008.

7] Luciani A, Plummer CJG, Nguyen, T, Garamszegi L, Manson JE. Rheological and Physical Properties of Aliphatic Hyperbranched Polyesters. J. Polym. Sci. Part B: Polym. Phys. 2004; 42: 1218.

8] Žagar E, Žigon M. Characterization of a Commercial Hyperbranched Aliphatic Polyester Based on 2,2-Bis(methylol)propionic Acid. Macromolecules 2002; 35: 9913.

9] Žagar E, Huskić M, Žigon M. Macrom. Structure-to-Properties Relationship of Aliphatic Hyperbranched Polyesters. Chem. Phys. 2007; 208: 1379.

10] Žagar E, Huskić M, Grdadolnik J, Žigon M, Zupančić-Valant A. Effect of Annealing on the Rheological and Thermal Properties of Aliphatic Hyperbranched Polyester Based on 2,2-Bis(methylol)propionic Acid. Macromolecules 2005; 38: 3933.

11] Žagar E, Žigon M, Podzimek S. Characterization of Commercial Aliphatic Hyperbranched Polyesters. Polymer 2006; 47: 166.

12] Tanis I, Karatasos K. Local Dynamics and Hydrogen Bonding in Hyperbranched Aliphatic Polyesters. Macromolecules 2009; 42: 9581.

13] Malmström E, Johansson M, Hult A. Hyperbranched Aliphatic Polyesters. Macromolecules 1995; 28: 1698.

14] Burgath A, Sunder A, Frey H. Role of Cyclization in the Synthesis of Hyperbranched Aliphatic Polyesters. Macromol. Chem. Phys. 2000; 201: 782.

15] Malmström E, Hult A. Kinetics of Formation of Hyperbranched Polyesters Based on 2,2-bis(methylol)propionic Acid. Macromolecules 1996; 29: 1222.

16] Magnusson H, Malmström E, Hult A. Structure Buildup in Hyperbranched Polymers from 2,2-Bis(hydroxymethyl)propionic Acid. Macromolecules 2000; 33: 3099.

17] Zeiner T, Shrader P, Enders S, Browarzik DJ. Phase- and Interfacial Behavior of Hyperbranched Polymer Solutions. Fluid Phase Equilib. 2011; 302: 321.

18] Tsukruk VV. Dendritic Macromolecules at Interfaces. Adv. Mater. 1998; 10(3): 253.

19] Peleshanko S, Tsukruk VV. The architectures and surface behavior of highly branched molecules. Prog. Polym. Sci. 2008; 33: 523.

20] Tsukruk VV, Rinderspacher F, Bliznyuk VN. Self-Assembled Multilayer Films from Dendrimers. Langmuir 1997; 13: 2171.

21] Bakshi MS, Sood R, Kaur G, Sakai K, Yoshimura T, Esumi K. Characterization of aliphatic and aromatic polyester hyperbranched dendrimers by AFM imaging. Colloid Polym. Sci. 2005; 284: 74.

22] Sheiko SS, Musafarov AM, Winkler RG, Getmanova EV, Eckert G, Reineker P. Contact Angle Microscopy on a Carbosilane Dendrimer with Hydroxyl End Groups: Method for Mesoscopic Characterization of the Surface Structure. Langmuir 1997; 13: 4172.

23] Mansfield ML. Surface adsorption of model dendrimers. Polymer 1996; 37(17): 3835.

24] Plummer CJG, Gramszegi L, Leterrier Y, Rodlert M, Månson JE. Hyperbranched Polymer Layered Silicate Nanocomposites. Chem. Mater. 2002; 14: 486.

25] Rodlert M, Plummer CJG, Grünbauer HJM, Månson JE. Hyperbranched Polymer/Clay Nanocomposites. Adv. Eng. Mater. 2004; 6(9): 715.

26] Rodlert M, Plummer CJG, Gramszegi L, Leterrier Y, Grunbauer HJM, Månson JE. Hyperbranched Polymer/Montmorillonite Clay Nanocomposites. Polymer 2004; 45: 949.

27] Rodlert M, Plummer CJG, Leterrier Y, Månson JE. Rheological Behavior of Hyperbranched Polymer/Montmorillonite Clay Nanocomposites J. Rheol. 2004; 48(5): 1049.

28] Decker JJ, Chvalun SN, Nazarenko S. Intercalation behavior of hydroxylated dendritic polyesters in polymer clay nanocomposites prepared from aqueous solution. Polymer 2011; 52: 3943.

29] Androulaki K, Chrissopoulou K, Prevosto D, Labardi M, and Anastasiadis SH. Dynamics of Hyperbranched Polymers Under Confinement: A Dielectric Relaxation Study. ACS Appl. Mater. Interfaces 2015; 7: 12387

30] Fotiadou S, Karageorgaki C, Chrissopoulou K, Karatasos K, Tanis I, Tragoudaras D, Frick B, Anastasiadis SH. Structure and Dynamics of Hyperbranched Polymer/Layered Silicate Nanocomposites. Macromolecules 2013; 46: 2842.

31] Liyanage AU, Ikhuoria EU, Adenuga AA, Remcho VT, Lerner MM. Synthesis and Characterization of Low-Generation Polyamidoamine (PAMAM) Dendrimer-Sodium Montmorillonite (Na-MMT) Clay Nanocomposites. Inorg. Chem. 2013; 52: 4603.

32] Wunderlich B. Reversible crystallization and the rigid–amorphous phase in semicrystalline macromolecules. Prog. Polym. Sci. 2003; 28: 383.

33] Wunderlich B. Calorimetry of Nanophases of Macromolecules. Int. J. Thermophys. 2007; 28: 958.

34] Lin J, Shenogin S, Nazarenko S. Oxygen Solubility and Specific Volume of Rigid Amorphous Fraction in Semicrystalline Poly(ethylene terephthalate). Polymer 2002; 43: 4733.

35] Olson BG, Lin J, Nazarenko S, Jamieson AM. Positron Annihilation Lifetime Spectroscopy of Poly(ethylene terephthalate): Contributions from Rigid and Mobile Amorphous Fractions. Macromolecules 2003; 36: 7618.

36] Righetti MC, Tombari E, Di Lorenzo ML. The Role of the Crystallization Temperature on the Nanophase Structure Evolution of Poly[(R)-3-hydroxybutyrate]. J. Phys. Chem. B 2013; 117: 12303.

37] Di Lorenzo ML, Androsch R, and Stolte I. Tailoring the rigid amorphous fraction of isotactic polybutene-1 by ethylene chain defects. Polymer 2014; 55: 6132.

38] Hamonic F, Miri V, Saiter A, and Dargent E. Rigid amorphous fraction versus oriented amorphous fraction in uniaxially drawn polyesters. Eur. Polym. J. 2014; 58: 233.

39] Beckingham BS, Ho V, and Segalman RA. Formation of a Rigid Amorphous Fraction in Poly(3-(2'-ethyl) hexylthiophene). ACS Macro Lett. 2014; 3: 684.

40] Righetti MC, Laus M, and Di Lorenzo ML. Temperature dependence of the rigid amorphous fraction in poly(ethylene terephthalate). Eur. Polym. J. 2014; 58: 60.

41] Righetti MC, Laus M, Di Lorenzo ML. Rigid amorphous fraction and melting behavior of poly(ethylene terephthalate). Colloid Polym. Sci. 2014; 292: 1365.

42] Tognana S and Salgueiro W. Influence of the rigid amorphous fraction and segregation during crystallization in PHB/DGEBA blends. Polym. J. 2015: 1.

43] Massa CA, Pizzanelli S, Bercu V, Pardi L, and Leporini D. Constrained and Heterogeneous Dynamics in the Mobile and the Rigid Ammorphous Fractions of Poly(dimethylsiloxane): A Multifrequency High-Field Electron Paramagnetic Resonance Study. Macromolecules 2014; 47, 6748.

44] Remy R, Wei S, Campos LM, and Mackay ME. Three-Phase Morphology of Semicrystalline Polymer Semiconductors: A Quantitative Analysis. ACS Macro Lett. 2015; 4: 1051.

45] Sargsyan A, Tonoyan A, Davtyan S, Schick C. The amount of immobilized polymer in PMMA SiO_2 nanocomposites determined from calorimetric data. Eur. Polym. J. 2007; 43: 3113.

46] Corcione EC, Maffezzoli A. Glass transition in thermosetting clay-nanocomposite polyurethanes. Thermochim Acta 2009; 485: 43.

47] Wurm A, Ismail M, Kretzschmar B, Pospiech D, Schick C. Retarded Crystallization in Polyamide/Layered Silicates Nanocomposites Caused by an Immobilized Interphase. Macromolecules 2010; 43: 1480.

48] Fotiadou S, Chrissopoulou K, Frick B, Anastasiadis SH. Structure and Dynamics of Polymer Chains in Hydrophilic Nanocomposites. J. Polym. Sci., Part B: Polym. Phys. 2010; 48: 1658.

49] Sari MG, Shahbazi M, Pakdel AS. Developing a Novel Hyperbranched Polymer-Modified PP/Clay Nanocomposite: Characteristics Investigation. Polymer-Plastics Technology and Engineering 2014; 53: 1561

50] Sargsyan A, Tonoyan A, Davtyan S, Schick C. The amount of immobilized polymer in PMMA SiO_2 nanocomposites determined from calorimetric data. Eur. Polym. J. 2007; 43: 3113.

51] Sargsyan A, Tonoyan A, Davtyan S, and Schick C. Rigid Amorphous Fraction in Polymer Nano-Composites. NATAS Notes 2007; 39: 6.

52] Pissis P, Klonos P, and Kyritsis A. Interfacial Effects in Polymer Nanocomposites Studied by Dielectric and Thermal Techniques. IEEE 2011; 67.

53] Davtyan SP, Tonoyan AO, Varderesyan AZ, Muller SC. Frontal compolymerization in the presence of nano-particles. Eur. Polym. J. 2014; 57: 182.

54] Kim S, Nguyen NA, Wie JJ, and Park HS. Manipulating the glass transition behavior of sulfonated polystyrene by functionalized nanoparticle inclusion. Nanoscale 2015; 7: 8864.

55] Chrissopoulou K, Fotiadou S, Frick B, and Anastasiadis SH. Structure and Dyanamics in Hydrophillic Polymer/ Layered Silicate Nanocomposites. Macromol. Symp. 2013; 331-332: 50.

56] Signori F, Pelagaggi M, Bronco S, and Righetti MC. Amorphous/crystal and polymer/filler interphases in biocomposites from poly(butylene succinate). Thermochim Acta 2012; 543: 74.

57] Karami S and Lafleur PG. Role of Chain Dynamics and Topological Confinements in Cold Crystallization of PLA-Clay Nanocomposites. Polym. Eng. Sci. 2015; 55: 1310

58] Klonos P, Kripotou S, Kyritsis A, Papageorgiou GZ, Bikiaris D, Gournis D, and Pissis P. Glass transistion and segmental dyanmics in poly(L-lactic acid)/ graphene oxide nanocomposites. Thermochim Acta 2015; 617: 44.

59] Charlon S, Marais S, Dargent E, Soulestin J, Sclavons M, and Follain N. Structure-barrier property relationship of biodegradable poly(butylene succinate) and poly[(butylene succinate)-co-(butylene adipate)] nanocomposites: influence of the rigid amorphous fraction. Phys. Chem. Chem. Phys. 2015; 17: 29918.

60] Rath SK, Sudarshan K, Bhavsar RS, Kharul UK, Pujari PK, Patri M, and Khakhar DV. Characterizing the nanoclay induced constrained amorphous region in model segmented polyurethane-urea/clay nanocomposites and its implications on gas barrier properties. Phys. Chem. Chem. Phys. 2016; 18: 1487.

61] Purohit PJ, Wang D, Wurm A, Schick C, and Schonhals A. Eur. Polym. J. 2014; 55: 48.

62] Fotiadou S, Karageorgaki C, Chrissopoulou K, Karatasos K, Tanis I, Tragoudaras D, Frick B, Anastasiadis SH. Structure and Dynamics of Hyperbranched Polymer/Layered Silicate Nanocomposites. Macromolecules 2013; 46: 2842.

63] Pethrick RA. Positron annihilation—A probe for nanoscale voids and free volume? Prog. Polym. Sci. 1997; 22: 1.

64] Jean YC, Mallon PE, Schrader DM (Eds). Principles and Applications of Positron and Positronium Chemistry. River Edge, NJ: World Scientific; 2003.

65] Higuchi H, Yu Z, Jamieson AM, Simha R, McGervey JD. Thermal history and temperature dependence of viscoelastic properties of polymer glasses: relation to free volume quantities. J. Polym. Sci. Polym. Phys. 1995; 33(17): 2295.

66] Simha R, Somcynsky T. On the Statistical Thermodynamics of Spherical and Chain Molecule Fluids. Macromolecules 1969; 2: 342.

67] Eldrup M, Lightbody D, Sherwood NJ. The temperature dependence of positron lifetimes in solid pivalic acid. Chem. Phys. 1981; 63: 51.

68] Tao SJ. Positronium annihilation in molecular substances. J. Chem. Phys. 1972; 56: 5499.

69] Lagaly G, Ziesmer S. Colloid chemistry of clay minerals: the coagulation of montmorillonite dispersions. Adv. Colloid Interface Sci. 2002; 100: 105.

70] Carmezini G, Mackay ME, Sauer BB, Kampert W. Manipulation of Hyperbranched Polymers' Conformation. Chem. Mater. 2002; 14: 819.

71] Cheng SZD, Cao M-Y, Wunderlich B. Glass transition and melting behavior of poly(oxy-1,4-phenyleneoxy-1,4-phenylenecarbonyl-1,4-phenylene) (PEEK). Macromolecules 1986; 19: 1868.

72] Richardson MJ. In: Mathot VBF (Eds.) Calorimetry and thermal analysis of polymers. Munich: Hanser; 1993. 170.

73] Kirkegard P, Eldrup M, Morgesen OE, Pedersen, NJ. Program system for analysing positron lifetime spectra and angular correlation curves. Comput. Phys. Commun. 1981; 23: 307.

74] Grebowicz J, Lau SF, Wunderlich BJ. The thermal properties of polypropylene. J. Polym. Sci. Polym. Symp. 1984; 71: 19.

75] Suzuki H, Grebowicz J, Wunderlich BJ. Heat capacity of semicrystalline, linear poly(oxymethylene) and poly(oxyethylene). Macromol. Chem. 1985; 186: 1109.

76] Jamieson AM, Olson BG, Nazarenko S. Positron Annihilation Lifetime Studies of Free Volume in Heterogeneous Polymer Systems In L. Utrackie and A. Jamieson (Eds.), Polymer Physics: From Suspensions to Nanocomposites and Beyond. Hoboken, NJ: John Wiley & Sons, Inc.; 2010. 473.

77] Yu Z, Yahsi U, McGervey JD, Jamieson AM, Simha R. Molecular Weight-Dependance of Free Volume in Polystyrene Studied by Positron Annihilation Measurements. J. Polym. Sci. Pol. Phys. 1994; 32: 2637.

78] Choudalakis G, Gotsis AD. Free volume and mass transport in polymer nanocomposites. Curr. Opin. Colloid Interface Sci. 2012; 17: 132.

79] Wang Y-Q, Wu, Y-P, Zhange H-F, Zhang L-Q, Wang B, Wang Z-F. Free Volume of Montmorillonite/Styrene-Butadiene Rubber Nanocomposites Estimated by Positron Annihilation Lifetime Spectroscopy. Macromol. Rapid Commun. 2004; 25: 1973.

80] Wang ZF, Wang B, Qi N, Zhang HF, Zhang LQ. Influence of Fillers on Free Volume and Gas Barrier Properties in Styrene-butadiene Rubber Studied by Positrons. Polymer 2005; 46: 719.

81] Nakanishi H, Jean YC. Dynamics of Excess Free Volume in Semicrystalline PEEK Studied by Positron Annihilation. Macromolecules 1991; 24: 6618.

82] Nakanishi H, Jean YC. Positronium Formation at Free-volume Sites in the Amorphous Regions of Semicrystalline PEEK. J. Polym. Sci. B 1989; 27: 1419.

83] Sano M, Murakami H, Ichimura K. Positronium in a layered-structure material: Montmorillonite. J. Radioanal. Nucl. Chem. 1999; 239 (2): 325.

84] Harms S, Rätzke K, Faupel F, Schneider GJ, Willner L, and Richter D. Free Volume of Interphases in Model Nanocomposites Studied by Positron Annihilation Lifetime Spectroscopy. Macromolecules 2010; 43: 10505.

APPENDIX A – MULTILAYERED COMPOSITES CONTAINING LOW T_g PHOSPHATE GLASS: CONTROLLED INTERDIFFUSION FOR IMPROVED GAS BARRIER PROPERTIES

This chapter was co-authored with Matthew Herbert, David A Schiraldi, and Sergei Nazarenko

Abstract

Multilayer coextrusion of alternating linear low density polyethylene (LLDPE)/low T_g phosphate glass (pglass) composite and low density polyethylene (LDPE) layers was utilized in an attempt to produce an easily processable high gas barrier system. This study attempted to utilize asymmetric layer interdiffusion to promote particle coalescence of pglass into high aspect ratio impermeable sheets. Particle concentration from layer shrinkage has been previously demonstrated to occur in systems of alternating layers of polymers with highly different mobilities when annealed in the melt. A convective flow of the more slowly diffusing molecules (LDPE) can be observed opposite to the faster diffusing molecules (LLDPE) containing particles. The goal being, that as the pglass beads are concentrated, the close proximity of the pglass particles would favor coalescence. Composites of pglass (75 ± 3°C and 135 ± 3°C) with a wide range of loadings (up to 30 vol%) were morphologically analyzed and selected systems multilayered. Particle concentration was observed through SEM microscopy; however, particle coalescence into high aspect ratio sheets was not apparent. While some coalescence most likely occurred, as evident from increases in particle diameters, the forces on the particles did not prove substantial enough to force the particles into platelet form and only resulted in the 2D alignment of the glass spheres.

Introduction

Polymer films have been of critical importance in the coating and food packaging industries for many years due to their inexpensive cost, ease of processing and manufacturing, and mechanical strength; however, many polymers are less effective than desired in regards to gas barrier properties which limits their application in many applications including electronic encapsulation. In this project we investigated the utilization of coextruded multilayer films with layers of glass particulate (low T_g phosphate glass) filled nanocomposites in an attempt to increase a polymer's gas barrier properties.

Phosphate glasses (pglass) are "polymeric" in nature as they are comprised of chained or crosslinked network structures [1-4]. These phosphorous, especially tin flouro phosphate glasses, based glasses can be produced to exhibit a wide range of T_gs [5-7] and exhibit a variety of intriguing properties [8]. As the pglasses' T_gs can be tailored, particles can be produced that are fluidic under the processing temperatures of a variety of polymers. Pglass polymer composites, especially in polyolefin [9-16] and polyamide [17-23] based polymers, have been extensively studied previously. The fluidic nature of the pglass under processing conditions enables very high pglass loadings to be attained (up to ~90 vol%) [22, 24-26]. The phosphate fillers have shown to impart oxygen [16], water [27}, and fire [23] barrier along with mechanical reinforcement [11,17,27-28] to a polymer matrix. Urman and Otaigbe previously provided a comprehensive review of the current (as of 2007) status of phosphate glass polymer composites [26].

As mentioned, pglass based composites have been shown to impart oxygen barrier properties to a polymer matrix under the right processing conditions. Gupta et al [16]

demonstrated that through biaxial stretching coextruded films comprised of alternating layers of coextruded maleic anhydride grafted polypropylene incorporated with phosphate glass particles, a 2-3 orders of magnitude improvement in oxygen barrier could be achieved as compared to the bulk unoriented polymer. They attributed this enhanced barrier to the formation of high aspect ratio pglass platelets upon stretching, resembling a brick wall structure. These platelets increased the tortuosity pathway for diffusing molecules and thus lowered the overall permeability of the films.

This work led to our idea of the possibility of creating high aspect ratio pglass sheets from a different technique. This method involves the harnessing of unequal interdiffusion in the melt across multilayer boundaries to shrink intended layers and concentrate particles imbedded in those layers.

Previously it has been demonstrated that melt induced interdiffusion of polymers in microlayers can be utilized to increase the concentration of inorganic particles in one of the component layers [29-31]. Studies have shown that when microlayers of linear low density polyethylene (LLDPE) and low density polyethylene (LDPE) were annealed into the melt, a moving boundary is observed as the more mobile linear LLDPE chains diffuse more quickly into the slowly diffusing branched LDPE chain layer. The result is shrinkage of the LLDPE phase [29,31-33]. If particles are dispersed in the LLDPE layers, a particle concentration phenomenon is observed as the composite layers become depleted of polymer [29-31]. This study aims to address the question that if pglass particles are dispersed in these shrunken LLDPE layers, will the boundary movement forces promote/force coalescence of the particles, that are fluidic at the annealing temperature, into high aspect ratio platelets or sheets that are desired for barrier property

enhancement (Scheme A.1). These platelets would create a more tortuous path for any diffusing penetrant and thus lower the diffusivity coefficient of the polymer.

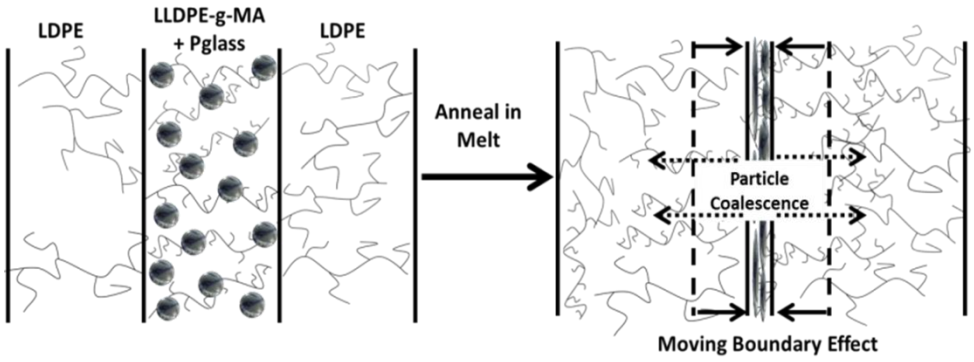

Scheme A.1 Scheme for creating high aspect ratio pglass platelets from multilayer polymer interdiffusion in the melt.

Therefore, the structures of the pglass/LLDPE composites and multilayered systems with particulates were morphologically analyzed. The particle concentration effect from interdiffusion in multilayers was investigated and low T_g phosphate glass particle coalescence monitored for multiple systems varying in multilayer structure, pglass material, and pglass loading.

Experimental

Materials

Tin fluoro-phosphate glasses (pglass) were prepared from reagent grade tin fluoride (SnF_2), tin oxide (SnO), tungsten trioxide (WO_3) and ammonium dihydrogen phosphate ($NH_4H_3PO_4$), all purchased from Sigma-Aldrich and used as received. Dowlex® 2035 grade LLDPE of the Dow Chemical Company with a bulk density of 0.919 g/cm^3 and a melt index of 6 g/10 min, was used for the pglass nanocomposites and Huntsman PE2030 LDPE from the Huntsman Corporation with a bulk density of 0.919

g/cm^3 and a melt index of 5 g/10 min was used for the unfilled layers during multilayer coextrusion.

Characterization

Composite blends were melt blended in a Prism TSE 16TC twin screw extruder at 200˚C and 80 rpm. A Carver Melt Press was utilized to prepare ~1 mm thickness composite films for gas barrier property analysis and morphological studies. A Dynisco Model D4001 melt flow indexer was used for viscosity calculations where viscosity was calculated as the shear stress at the wall divided by the shear rate at the wall.

Composite films were scaled up (2-3 kg) and multilayer films were coextruded in an extruder that consists of two ¾ inch single screw extruders with melt pumps, a coextrusion block, a series of layer multiplier elements, and a film die [34]. Films of ~300 μm thickness, with alternating layers of LDPE and composites (LLDPE/pglass) of approximately 30 μm (9 total layers) or 15 μm (17 total layers) average layer thicknesses were prepared. Separately 3 layer films were produced by stacking compression films in a ~700 μm mold.

Thermal analysis, T_g determination, of the pglass was performed using a TA Instruments Q2000 Differential Scanning Calorimeter (DSC). Heating and cooling scans were carried out at a 10 °C/min rate over a range of -50 to 200 °C under a dry nitrogen atmosphere. Second heating scans were utilized for the analysis. Thermal property analysis, verification of pglass loading, of each of the LLDPE/pglass composite films was tested using Thermogravimetric Analysis (TGA) (model TA Instruments TGA Q500). The TGA ramp rate was 10 °C/ minute up to 600 °C. Nitrogen with a flow rate of 10 mL/min was used as the sample gas.

Oxygen permeability measurements were made using a commercially available diffusion apparatus, MOCON OX-TRAN 2/21, at room temperature, 1 atmosphere partial oxygen pressure difference, and 0% RH.

A FEI Quanta 200 Scanning Electron Microscope (SEM) was used to analyze pglass size and dispersion along with multilayer morphology before and after interdiffusion in the melt state. Samples to be analyzed with SEM were cryogenically fractured and sputter coated with gold. Optical microscopy was also used to analyze some of the multilayer films. Semi-thin (~5μm) cryo-microtomed sections were used for the imaging.

Preparation of Tin Fluoro-Phosphate Glass

The phosphate glasses (pglass) were prepared on a 250 g scale, according to the procedure outlined by M. Gupta, et al [16]. The ingredients were carefully weighed and added into a closed jar to form pglass with a batch molar composition of 50% SnF_2 + 20% SnO + 30% P_2O_5 for the pglass with a T_g of 134-137°C. A batch molar composition of 65% SnF_2 + 17.5% SnO + 15% P_2O_5 + 2.5% WO_3 was utilized for the tungsten doped pglass with a T_g of 72-77°C. The ingredients were tumble mixed for 25-30 min to produce a uniform mixture and then transferred to a 300 ml capacity vitreous carbon crucible. The crucible was placed, uncovered, into a muffle furnace at 450 °C for 70 min. Fluid melts obtained using this procedure were quenched onto a stainless steel plate and annealed by placing in the oven at approximately 20 °C above T_g for about 90 min [35-36]. This results in a pglass with a density of ~3.65 ± 0.01 g cm^{-3}.

Results and Discussion

Dispersion of the pglass in the composite blends was analyzed using Scanning Electron Microscopy (SEM) and image analysis. Figure A.1 depicts the dispersion of the particles at different filler loadings. The particles are predominately spherical and the particle diameters steadily increase with increasing loadings. At small loadings, i.e., 1 wt% or 0.25 vol%, the particles exhibit a small average diameter size of around 1 μm. At 10 vol% the particles exhibit an average diameter of close to 5 μm. This technique is limited to the particles that could be observed in the SEM micrographs and thus some small particles might not be apparent, especially any under 1 μm in diameter.

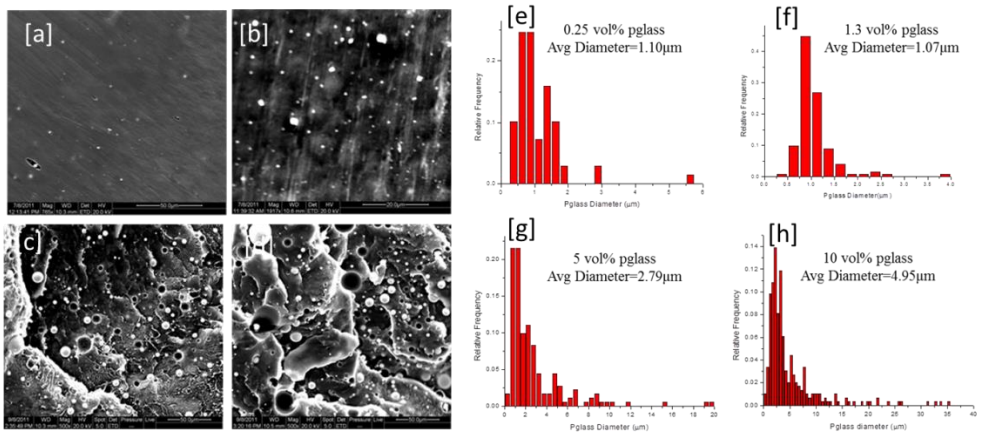

Figure A.1 Scanning Electron Microscopy images of (a,e) 0.25 vol%, (b,f) 1.3 vol%, (c,g) 5 vol%, and (d,h) 10 vol% and their corresponding histograms for pglass sphere diameters.

The permeability of the pglass/LLDPE nanocomposites were analyzed and compiled in Figure A.2. As expected, the spherical nature of the particles made any barrier improvement minimal. Significant barrier improvements are only observed at very high loadings and even then are less than impressive.

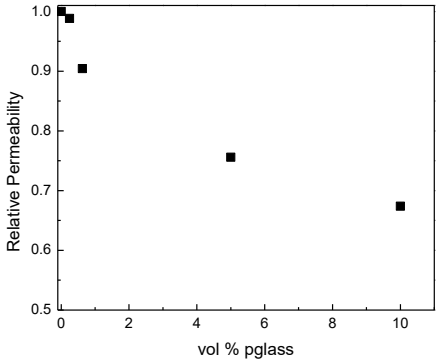

Figure A.2 Relative permeability of the pglass/LLDPE composites.

It has been shown that maleic anhydride can act as a compatibilizer for many types of fillers and enhance particle dispersions [16]. Therefore, we first added 10 wt% of maleic anhydride grafted LLDPE to the 10 vol% pglass blends to promote dispersion. The effect was quite pronounced, as the small amount of maleic anhydride grafted to the LLDPE helped reduce the particle diameter size nearly in half, from ~5 μm to 2.75 μm. When the glass particles were dispersed in pure maleic anhydride grafted LLDPE, the particle diameter size reduced even more to ~2 μm.

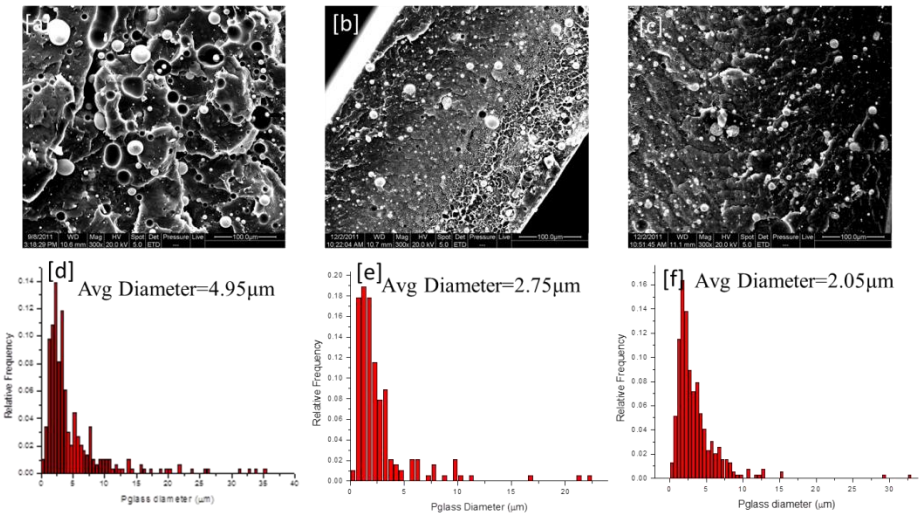

Figure A.3 Scanning Electron Microscopy images of (a,d) 10 vol% pglass + LLDPE, (b,e) 10 vol% pglass + 10 wt% LLDPE-g-MA + 59 wt% LLDPE, and (c,f) 10 vol% pglass + LLDPE-g-MA and their corresponding histograms for pglass sphere diameters.

There is a wide range of batch compositions reported that lead to phosphate glasses with a wide range of T_g's. Therefore, we decided to formulate a pglass that had an even lower T_g than the previous system. A tungsten doped pglass filler dispersed in LLDPE resulted in the interesting morphologies depicted in Figure A.4. The tungsten doped pglass exhibited less of a spherical morphology. The shape of the particles made measuring the particle sizes very difficult, especially at high loadings.

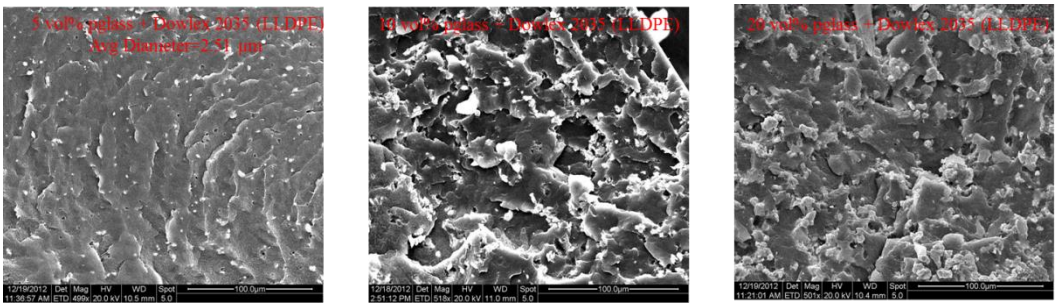

Figure A.4 Scanning Electron Microscopy images of tungsten doped pglass in LLDPE at (left) 5 vol%, (center) 10 vol%, and (right) 20 vol% pglass loadings.

Composites with 5 vol% pglass in LLDPE were chosen to be multilayered with alternating layers of LDPE. This composite and the LDPE had MFI values that could be easily matched during coextrusion at ~200°C. SEM images of cryo-fractured multilayers can be viewed in Figure A.5 for a control (unfilled LLDPE/ unfilled LDPE) and composite multilayer (5 vol% pglass + LLDPE/ unfilled LDPE). 17 layer films were utilized to make sure the layers were larger than all the particles.

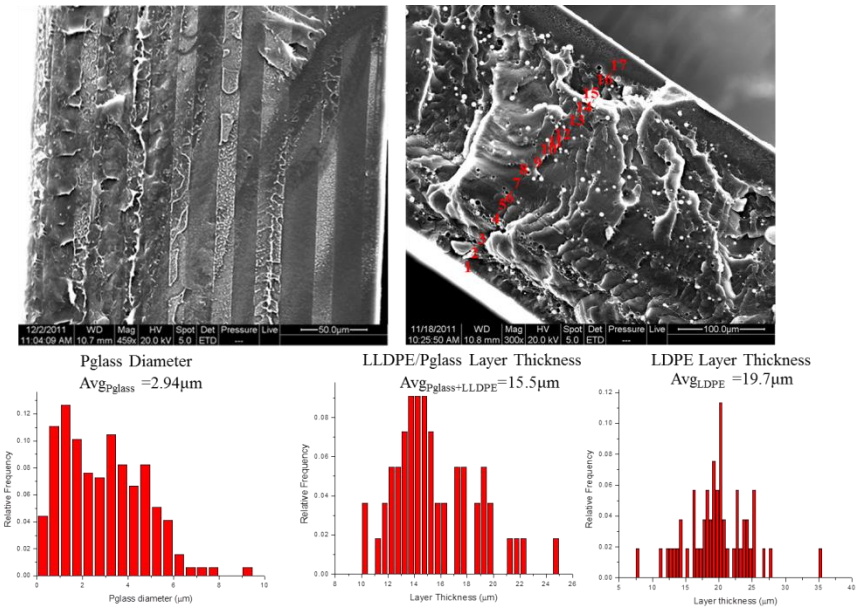

Figure A.5 SEM images of 17 layer coextruded film consisting of alternating layers of LDPE and (top left) unfilled LLDPE and (top right) LLDPE + 5 vol% pglass along with histograms for the composite multilayer film's pglass diameter, composite layer thickness, and LDPE layer thickness.

A morphological examination of the composite multilayer films yielded the histograms found in Figure A.5. While intended for the multilayers to be a 50/50 mixture of composite layers and LDPE layers, the layer thickness analysis shows that the unfilled LDPE layers were initially thicker. This could be a result of improper control of the melt feed flowrates during coextrusion or the result of layer boundary movement from interdiffusion that occurred during the coextrusion process.

As mentioned, the goal of the project was to promote particle coalescence into high aspect ratio sheets through using of the "moving boundary"/"particle concentration" effect brought on through interdiffusion in the melt. The film samples were thus annealed for up to 10 hours to promote the composite layer shrinkage. SEM images were taken at various levels of interdiffusion and some are shown in Figure A.6. As the

composite layers are shrunken with annealing time, one can observe the pglass spheres align in two dimensional rows, opposite the initial random three dimensional ordering in the original (unannealed) film layers. However, particle coalescence was not readily apparent.

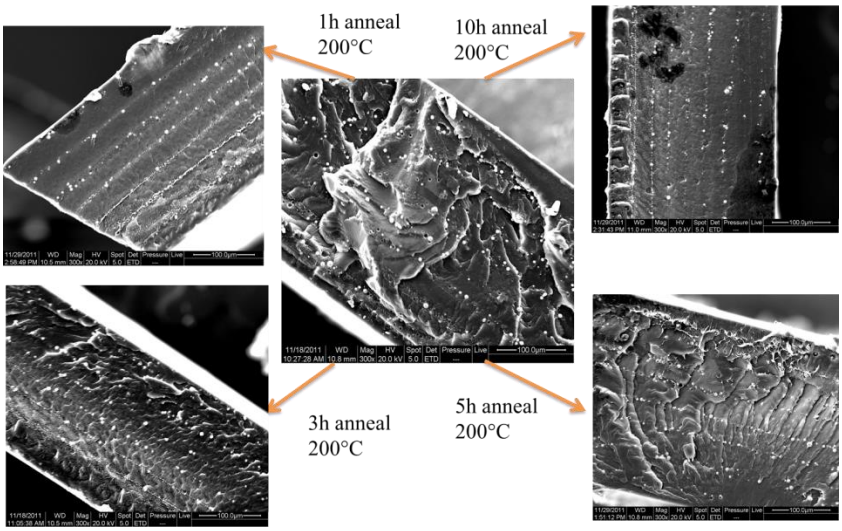

Figure A.6 Scanning Electron Microscopy images of 17 layer coextruded film consisting of alternating layers of LDPE and LLDPE + 5 vol% pglass composite. Images show layer morphology changes with annealing time at 200°C.

The LDPE and composite layer thickness changes are plotted in Figure A.7. The thickness of the composite layers reduced to about a third of their original thickness with interdiffusion in the melt. This is consistent with some of our previous work. While particle coalescence into platelets or sheets was not observed, there appears to be a slight increase in thickness of the pglass droplets with layer shrinkage. This could be the result of some particles coalescing into larger spheres; however, the effect is so minimal and falls within the error of the measurements.

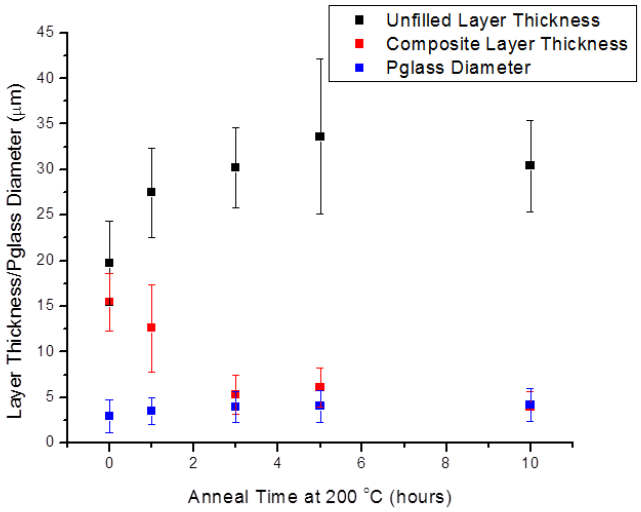

Figure A.7 Layer thickness and particle diameter changes for the 17 layer coextruded film consisting of alternating layers of LDPE and LLDPE + 5 vol% pglass composite with annealing time at 200°C.

Multilayer films were also made utilizing the lower T_g tungsten doped pglass as shown in optical microscopy images in Figure A.8. The idea to use this lower T_g glass was twofold. First, the tungsten doped pglass resulted in smaller less spherical particles than the original pglass. We hoped this hinted that these glass particles had a higher inclination to form oblong or higher aspect ratio shapes. Also, it was hypothesized that during film cooling after annealing, the polymer would crystallize ($T_{m\text{-}LLDPE}$~124°C) first while the pglass was still liquid. The resulting material contraction during the melt to solid state transition might further promote particle coalescence into platelets. The pglass loading was increased to 10 vol% and the amount of layers was also reduced to 9 in these multilayered systems to increase the volume/proximity of pglass particles to each other when the particles concentrate into 2D rows again.

From the optical microscopy images in Figure A.8, the particle concentration after 5 hours is clearly visible; however the particles still do not appear to be coalesced into single sheets.

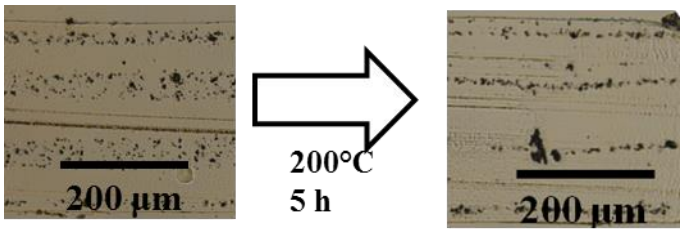

Figure A.8 Optical Microscopy images of 9 layer coextruded films consisting of alternating layers of LDPE and LLDPE + 10 vol% tungsten doped pglass composite. Images show the layer morphology changes after annealing for 5 hours at 200°C.

Lastly, three layer films were constructed using compression molding to create a system with a layer that was highly concentrated with pglass particles and quite thick. The films consisted of outer layers that measured around 300 µm (diffusion sink for LLDPE) and composite layers that measured around 100 µm with tungsten doped pglass concentrations of 5, 10, 20, and 30 vol%. SEM images of these trilayer systems are shown in Figure A.9.

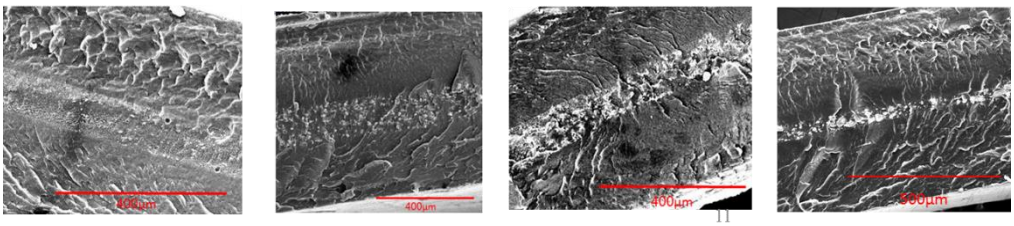

Figure A.9 SEM images of 3 layer compression molded films consisting of alternating layers of LDPE and LLDPE + 5, 10, 20, or 30 vol% (left to right) pglass.

The films were annealed for 24 hours and the resultant samples' layer thicknesses analyzed. The 5 and 10 vol% trilayers showed substantial internal layer thickness

reduction post annealing. The samples with more than 20 vol% pglass in the internal layers did not show any appreciable thickness changes with annealing. The polymer is most likely blocked or constrained from diffusing by the large amount/structure of the particles. An SEM micrograph before and after annealing for the 10 vol% pglass trilayer system is shown in Figure A.10. The zoomed in segment appears to show some coalescence of the particles. However, it is very apparent that regions of pure LLDPE still transverse the composite layer and any permeation improvement would be minimal.

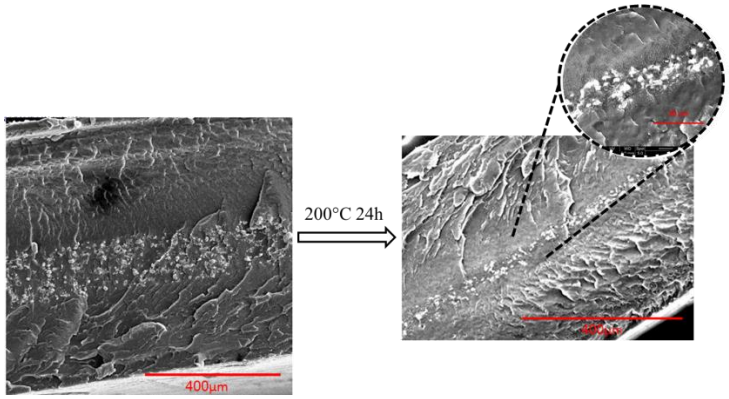

Figure A.10 SEM images of 3 layer coextruded films consisting of alternating layers of LDPE and LLDPE + 10 vol% tungsten doped pglass composite. Images show the layer morphology changes after annealing for 24 hours at 200°C.

Conclusions and Future Efforts

Phosphate glass (pglass) blends were successfully dispersed in a polymeric system with viscosities well within the limits of multilayer co-extrusion. Composites of pglass (T_g~ 75 ± 3°C and 135 ± 3°C) with a wide range of loadings (up to 30 vol%) were morphologically analyzed and selected systems multilayered. A morphological analysis of pglass droplet diameter size what conducted on the pglass composites, including those with an added LLDPE-g-MA compatibilizer. Pglass particle size increased with loading and the compatibilizer was successful in reducing the particle sizes. Gas barrier

properties were not greatly reduced at low loadings, typical of dispersions of spherical particulates.

Selected systems were successfully multilayer coextruded as a system with alternating linear low density polyethylene (LLDPE)/pglass composite and low density polyethylene (LDPE) layers. This study attempted to utilize asymmetric layer interdiffusion to promote particle coalescence of pglass into high aspect ratio impermeable sheets. Particle concentration from layer shrinkage was demonstrated in the composite multilayers as a convective flow of the more slowly diffusing molecules (LDPE) was observed opposite to the faster diffusing molecules (LLDPE) containing pglass. The pglass beads were concentrated into aligned 2D spheres, as observed through SEM/OM microscopy; however, the close proximity of the pglass particles did not appear to favor coalescence. Particle coalescence into high aspect ratio sheets was not apparent. While some coalescence most likely occurred, as evident from increases in particle diameters, the forces on the particles did not prove substantial enough to force the particles into platelet form and only resulted in the 2D alignment of the glass spheres. Other post processing techniques are most likely needed to force the aligned pglass spheres into the advantageous high aspect ratio morphology.

Acknowledgements

The authors are grateful to the National Science Foundation for support of this work through the Center for Layered Polymeric Systems (DMR 0423914) and the GK-12 fellowship program (DGE-1007911, Award #0947944). Special thanks are to be given to

the Matthew Herbert and Dr. David Schiraldi at Case Western Reserve University for their careful manufacturing of the pglass and the multilayered films.

References

1. Brow RK. Review: The structure of simple phosphate glasses. J. Non-Cryst Solids 2000; 263–264:1–28.
2. Ray NH. Inorganic polymers. New York: Academic Press; 1978.
3. Ray NH. The structure and properties of inorganic polymeric phosphates. Br Polym J 1979; 11: 163–77.
4. Otaigbe JU, Beall GH. Inorganic phosphate glasses as polymers. Trends Polym Sci 1997; 5: 369–79.
5. Sanford LM, Tick PA. Tin-phosphorous oxyfluoride glasses. 1982, US Patent: 4,314,031.
6. Smith GP. Some Recent Advances in Glasses and Glass-Ceramics. Mater and Design 1989; 10(2): 54.
7. Popova E, Dimitriev Y. Tin-based amorphous and composite materials. J Mater Sci 2007; 42: 3358-3366.
8. Loong C-K, Suzuya K, Price DL, Sales BC, Boatner LA. Structure and dynamics of phosphate glasses: from ultra- to orthophosphate composition. Physica B 1998; 241–243: 890–6.
9. Adalja SB, Otaigbe JU, Thalacker J. Glass-Polymer Melt Hybrinds. I: Viscoelastic Properties of Novel Affordable Organic-Inorganic Polymer Hybrids. Polym Eng Sci 2001; 41(6): 1055.

10. Tischendorf BC, Harris DJ, Otaigbe JU, Alam TM. Investigation of Structure and Morphology Dynamics in Tin Fluorophosphate Glass- Polyethylene Hybrids Using Solid-State ^{1}H, ^{13}C, and ^{31}P MAS NMR. Chem Mater 2002; 14: 341-347.
11. Adalja SB, Otaigbe JU. Creep and Recovery Behavior of Novel Organic-Inorganic Polymer Hybrids. Polym Composite 2002; 23(2): 171.
12. Guschl PC, Otaigbe JU. An Experimental Study of Morphology and Rheology of Ternary Pglass-PS-LDPE Hybrids. Polym Eng Science 2003; 43(6): 1180-
13. Guschl PC, Otaigbe JU. Experimental observation and prediction of interfacial tension and viscoelastic emulsion model behavior in novel phosphate glass-polymer hybrids. J of Colloid Interf Sci 2003; 266: 82-92.
14. Guschil PC, Otaigbe JU. Crystallization Kinetics of Low-Density Polyethylene and Polypropylene Melt-Blended with Low-Tg Tin-Based Phosphate Glass. J Appl Polym Sci 2003; 90: 3445-3456.
15. Urman K, Schweizer T, Otaigbe JU. Uniaxial elongational flow and morphology development in LDPE/phosphate glass hybrids. Rheol Acta 2007; 46: 989-1001.
16. Gupta M, Lin Y, Deans T, Baer E, Hiltner A, Schiraldi DA. Structure and Gas Barrier Properties of Poly(propylene-graft-maleic anhydride)/ Phosphate Glass Composites Prepared by Microlayer Coextrusion. Macromolecules 2010; 43: 4230-4239.
17. Urman K, Otaigbe J. Novel Phosphate Glass/ Polyamide 6 Hybrids: Miscibility, Crystallization Kinetics, and Mechanical Properties. J Poly Sci Poly Phys 2006; 44: 441-450.

18. Urman K, Madbouly S, Otaigbe JU. Unusual accelerated relaxations of tin fluorophosphates glass/ polyamide 6 hybrid studied by broadband dielectric spectroscopy. Polymer 2007; 48: 1659-1666.
19. Urman K, Schweizer T, Otaigbe JU. Rheology of tin fluorophosphates glass/polyamide 12 hybrids in the low concentration regime. J Rheol 2007; 51(6): 1171-1187.
20. Urman K, Iverson D, Otaigbe JU. Study the Effects of Melt Blended Speed on the Structure and Properties of Phosphate Glass/ Polyamide 12 Hybrid Materials. J Appl Polym Sci 2007; 105: 1297-1308.
21. Rawal A, Fang XW, Urman K, Iverson D, Otaigbe JU, Schmidt-Rohr K. Promotion of the γ-Phase of Polyamide 6 in Its Nanocompoiste with Phosphate Glass. J Polym Sci Poly Phys 2008; 46: 857-860.
22. Rawal A, Kong X, Meng Y, Otaigbe JU, Schmidt-Rohr K. Reduced Crystallinity and Mobility of Nylon-6 Confined near the Organic-Inorganic Interface in a Phosphate Glass-Rich Nanocomposite Detected by ^{1}H- ^{13}C NMR. Macromolecules 2011; 44: 8100-8105.
23. Belyamani I, Otaigbe JU, Fielding W. Development of New Sustainable Inorganic Flame Retardant Additive System for Polyamide 6,6 with Improved Performance. Polym Eng Sci 2014; 55(8): 1741-1748.
24. Otaigbe JU, Quinn CJ, Beall GH. Processability and Properties of Novel Glass-Polymer Melt Blends. Polym Composite 1998; 19(1): 18.
25. Frayer, P. D., 2000, US Patent, 6,103,810.

26. Urman, K.; Otaigbe, J. U. New phosphate glass/polymer hybrids- Current status and future prospects. Prog Polym Sci 2007; 32: 1462–1498.
27. Otaigbe JU, Adams DO. Bioabsorbable Soy Protein Plastic Composites: Effect of Polyphosphate Fillers on Water Absorption and Mechanical Properties. J Envir Polym Degra 1997; 5(4): 199.
28. Georgiou G, Mathieu L, Pioletti DP, Bourban PE, Manson JAE, Knowles JC, Nazhat SN. Polylactic Acid-Phosphate Glass Composite Foams as Scaffolds for Bone Tissue Engineering. J Biomed Mater Res B 2007; 80B: 322-331.
29. Nazarenko S, Dennison M, Schuman T, Stepanov EV, Hiltner A, Baer E. Creating layers of concentrated inorganic particles by interdiffusion of polyethylenes in microlayers. J Appl Polym Sci 1999; 73(14): 2877-2885.
30. Pollock G, Nazarenko S, Hiltner A, Baer E. Interdiffusion in Microlayered Polymer Composites of Polycarbonate and a Copolyester. J App Polym Sci 1994; 52(2): 163-176.
31. Decker J, Meyers KP, Paul DR, Schiraldi DA, Hiltner A. Polyethylene-based nanocomposites containing organoclay: A new approach to enhance gas barrier via multilayer coextrusion and interdiffusion. Polymer 2015; 61(20): 42-54.
32. Schuman T, Stepanov EV, Nazarenko S, Capaccio G, Hiltner A, Baer E. Interdiffusion of Linear and Branched Polyethylene in Microlayers Studied via Melting Behavior. Macromolecules 1998; 31(14): 4551-4561.
33. Schuman T, Nazarenko S, Stepanov EV, Magonov SN, Hiltner A, Baer E. Solid State Structure and Melting Behavior of Interdiffused Polyethylenes in Microlayers. Polymer 1999; 40(26): 7373-7385.

34. Mueller C, Kerns J, Ebeling T, Nazarenko S, Hiltner A, Baer E. Microlayer coextrusion processing and applications. Polym Process Eng 1997; 97: 137-157.

35. Tick PA. Phys. Chem. Glasses 1988; 29: 49.

36. Xu XJ, Day DE. Properties and structure of Sn-P-O-F glasses. Phys Chem Glasses 1990; 31: 183-187.